

**Department of Physics and Astronomy
Heidelberg University**

Bachelor Thesis in Physics by

Leon Niklas Lindenberger

submitted in August 2021

Towards Ultra-Fast X-Ray Transient Absorption Spectroscopy in High Density Neon Gas:

Gas Flow Model for Experimental Setup and Numerical Predictions

This Bachelor thesis has been carried out by
Leon Niklas Lindenberger at the
Max-Planck-Institute for nuclear physics in Heidelberg
under the supervision of
Prof. Dr. Thomas Pfeifer and
Priv.-Doz. Dr. Alexander Dorn

Beitrag zur Realisierung ultraschneller transienter Röntgen-Absorptionsspektroskopie in Neongas hoher Dichte: Gasdurchflussmodell für Versuchsaufbau und numerische Vorhersagen

In dieser Arbeit wird ein Beitrag zur Realisierung eines bevorstehenden Experiments zur Untersuchung nicht linearer Effekte der Interaktion zwischen ultrakurzen, hochintensiven X-Ray Laserpulsen (European XFEL) und Neongas hoher Dichte mit Hilfe von transienter Absorptionsspektroskopie geleistet. Im Fokus steht die Anregung von K-Schalen-Elektronen mit 867.5 eV Photonenenergie. Der hierfür errichtete Target-Vakuumaufbau wird im Detail beschrieben und für diesen ein Modell der, im Betrieb vorherrschenden Druckbedingungen entwickelt. Dieses fußt auf der Theorie des Gasdurchflusses und somit auf der Auswahl einer zur Berechnung der, zentrale Komponenten charakterisierenden, physikalischen Größe des Leitwerts. Im Anschluss werden entsprechende Druck-Messergebnisse mit dem Ziel, die verlässlichste Methode der Vorhersage herauszustellen, diskutiert. Im zweiten Teil wird ein, für das Neon-Experiment angepasstes, numerisches Simulationsmodell auf Basis der Schrödinger Gleichung vorgestellt und die hiermit erhaltenen Ergebnisse diskutiert. Hierbei liegt der Fokus auf der potentiellen Manipulation der Absorptionslinien-Form und der Verstärkung resonanten Röntgenlaserlichts bei besonders hohen Spitzenintensitätswerten.

Towards Ultra-Fast X-Ray Transient Absorption Spectroscopy in High Density Neon Gas: Gas Flow Model for Experimental Setup and Numerical Predictions

In this thesis, a contribution is made towards the realisation of an upcoming experiment for the investigation of non-linear effects occurring in the interaction of ultra-short, high-intensity X-ray laser pulses (provided by the European XFEL) and high-density neon gas, based on transient absorption spectroscopy. The aim is to excite K-shell electrons with a photon energy of 867.5 eV. The target vacuum setup, constructed for this purpose, is described in detail and a model to characterise the pressure conditions prevailing during the experiment's operation, depending on the input pressure, is developed. This is based on the theory of gas flow and thus on the selection of an appropriate theory for calculating the conductance-values that classify central components of the experiment. Subsequently, corresponding pressure measurement data is discussed, aiming to identify the most reliable method of predicting the chamber pressures. In the second part, a numerical simulation model, adapted for the neon experiment and based on the Schrödinger equation, is presented along with a discussion of the results obtained. Here, emphasis is put on a potential manipulation of the absorption line shapes by means of transient energy shifts and on the amplification of resonant X-ray laser light at particularly high peak intensity values.

Contents

1	Introduction	5
2	Theory	8
2.1	X-ray free-electron laser	8
2.2	Neon atom	14
2.3	Interaction of laser-pulse and matter	16
2.4	Absorption spectroscopy	22
2.5	Physics of vacuum and gas flow	26
3	Experimental setup	31
3.1	Structural overview of the vacuum system	32
3.2	(Neon-) gas supply and target cell	36
3.3	Characterisation of <i>Festo</i> pressure control valve	38
3.4	Differential pressure and gas flow measurements	41
3.5	Pressure dependency on target cell hole diameter	54
3.6	Pressure dependency on gas type	57
3.7	Concluding remarks for upcoming beamtime	60
4	Numerical simulation	63
4.1	Mathematical basis of simulation method	63
4.2	Simulations for state-of-the-art XFEL peak intensities	66
4.3	Outlook for high intensities	68
5	Conclusion	76
	References	79
	Appendix	81
	Glossary	87
	Acknowledgment	88

1 Introduction

The foundations of modern scientific disciplines, amongst them those of physics, were laid down by Aristotle in the 4th century BC. In his teachings, the ancient polymath distinguished between two great philosophies. First comes metaphysics, the (ontological) theory of the **'being'** of all that exists. This is followed logically by physics, the theory of the **'becoming'** of all that exists. These two fundamental disciplines share the investigation and description of the spatio-temporal world [1]. Understanding this world is the natural endeavour of each and every human being, rooted in their disposition of wonder and amazement. This urge for knowledge, in turn, gives rise to the method of basic research, as conducted (amongst many other international research institutes) at the *Max Planck Institute for Nuclear Physics* in Heidelberg. Thereby, modern physics is constantly sounding out the realm of knowledge, often regarding or based on key concepts like energy and matter. To a great extent this is done on the (sub-)atomic level. Whenever enhanced technical possibilities offer an opportunity to successfully carry out new **experiments**, a refinement of the existing **theory** models can be expected at the very least. Perhaps, however, a radically new theory will have to be developed. One such recent technical development is provided by the *EuXFEL* - short for *European X-Ray Free-Electron Laser* - a state of the art free-electron laser system in Hamburg that went into operation in 2017 [2].

Such a next-generation laser, used in experiments to test a physical theory, blends seamlessly into the context of what was outlined above. To describe the 'being' of all that exists is devoid of meaning and cannot succeed without the 'becoming'. In this sense, information about the structures and laws of **matter** can only be obtained in a process of 'becoming', namely the interaction with **light**. While humans constantly do this (in their day-to-day life and during optical sensory perception) on a macroscopic level and in the visible range of the electromagnetic spectrum, shorter wavelength light is required for (sub-)atomic investigations. The correspondingly higher photon energies are attainable owing to laser technology, as, for instance, the recent development of free electron lasers. Thus, employing the *EuXFEL*'s pulses with potential wavelengths down to 0.05 nm and photon energies up to 24 keV opens up numerous possibilities for practical applications in areas such as molecular biology, medicinal chemistry and computer technology, which can be explored on the *EuXFEL* website (see [2]).

An overview of previous experiments of basic research with extreme ultraviolet and X-ray FELs is given in [3] and [4]. This bachelor thesis is based on such a light-matter-interaction experiment as well, investigating the laser intensity and target gas pressure dependency of the measured absorption signal. For this experiment

and the underlying interaction with matter, the source of light has now already been introduced in the form of the *EuXFEL*. The X-ray laser pulses exhibit a peak intensity of around 10^{18} W/cm² and are referred to as ultra-short due to their duration of just a few femtoseconds [5]. The matter irradiated by these is gaseous neon, contained within a target cell in the pressure range of several bars. The induced interaction aims at the ($1s$ to $3p$) excitation of an electron in the core K-shell of the neon atom, facilitated by *EuXFEL* laser pulses with a resonant photon energy of 867.5 eV (which lies within the X-ray range). The interaction with neon gas, i.e. the resonant linear and nonlinear effects that occur in the process, leads to a temporal and spectral reshaping of the laser pulse. Subsequently, this is analysed by means of transient absorption spectroscopy and allows conclusions to be drawn about the electronic properties of the neon atom.

At the time of this bachelor thesis, the experiment described has not been carried out yet. During the beamtime at the *EuXFEL* in Hamburg, scheduled for this purpose, the spectrometer for the analysis of the reshaped laser light will be provided by *Uppsala University*. The primary task for the collaborators at the *Max Planck Institute* in Heidelberg is the construction of the vacuum setup complete with the gas inlet system which is to be linked to the two external components, *EuXFEL* and spectrometer, in the upcoming experiment. In addition to the central target cell, this setup comprises a main chamber, two pre-chambers on each side, a series of vacuum pumps and various other components. The laser beam, which propagates through the vacuum chambers and is meant to interact with the target gas only inside the cell, should not be attenuated (or absorbed elsewhere, of which the latter would happen in air at atmospheric pressure). Consequently, the key challenge is to establish and maintain high vacuum conditions, enabled by a thorough understanding of the pressures within the entire system. For this purpose, it was necessary to develop an applicable theory of the gas flow, apply it to the setup's components and to subsequently test the results experimentally.

As a second part of the groundwork prior to the upcoming experiment, a *Lab-VWIE* code, based on solving the Schrödinger equation was adapted to simulate the described laser pulses, the relevant energy level scheme of neon and their interaction. Thus, predictions can be made for the occurrence of certain effects, first and foremost the so-called Rabi coupling of ground and excited states at high intensities as well as the associated change of the resonant absorption line shapes.

This thesis aims to give the reader a broad overview of all mentioned aspects of the experiment at hand and, at the same time, to provide a detailed insight into the physical model of gas flow developed for the setup as well as into the expected ef-

fects for the interaction of ultrashort, high-intensity X-ray laser pulses with gaseous neon (inferred from the simulation results). To this end, the theoretical foundations of laser pulses, quantum mechanics, the neon atom to be investigated, various interaction effects (mainly Rabi oscillation and stimulated Raman scattering), absorption spectroscopy, and gas flow mechanics are laid in chapter 2. In chapter 3, the experimental setup with all relevant components and the therefor developed model of gas flow and pressure conditions is presented in detail. This is essentially based on identifying the value of the so-called conductance for elements through which gas flows. The measurements carried out are subsequently used to characterise central components (namely the pressure control valve and the target cells) as well as to test said theory model's validity. While in this chapter the pressure serves as the central control parameter to manipulate the absorption signals, the peak intensity of the laser pulse takes over this function in the subsequent chapter 4 where the numerical simulation is used to describe possible findings. Here, the occurrence of coupling effects during the interaction of X-ray light with neon gas is investigated for the proposed experimentally given intensities on the one hand, which is extended to even higher intensity regimes for the development of new theoretical insights and ideas on the other hand. The findings of the main chapters 3 and 4 finally lead to a conclusion and outlook in chapter 5. Hopefully, along the way, it will become clear, how the introduced dual interplay of matter and energy, theory and experiment, as well as 'being' and 'becoming' may constitute the proposed project.

2 Theory

The following chapter serves the same purpose in two different ways. Firstly, it is of great benefit to potential readers and those who wish to familiarise themselves with the basics of the underlying experiment to find here a collection of the physical foundations and effects. Secondly and most importantly, grasping the concepts presented is essential for a better understanding of the results presented later in this thesis. The common purpose, thus, is an introduction to the physics behind the experiment at hand.

For this purpose, first, the free-electron laser is introduced in chapter 2.1, as this type of laser (the *EuXFEL*) provides the radiation source for the experiment. Another central aspect of this is the target gas neon, which is subsequently presented in chapter 2.2. The interaction of high intensity, ultra-short XFEL pulses with irradiated neon atoms is at the heart of the physics to be studied. It therefore requires theoretical explanation, as is provided in chapter 2.3. The method of investigation in the experimental scope is transient absorption spectroscopy, the fundamentals of which are described in chapter 2.4. Finally, in chapter 2.5, theoretical principles of gas flow and pressure physics are outlined, as they apply to the feed of neon gas in the experiment.

2.1 X-ray free-electron laser

In the past decades, the research for and development of high intensity, ultra-short lasers (short for 'light amplification by stimulated emission of radiation') has made significant progress, reaching new regimes of photon energy. In 2016, the world's largest X-ray laser, measuring 3.4 kilometres in length, was taken into operation at the international *European X-Ray Free-Electron Laser* research facility (*EuXFEL*) in Hamburg [2, 3]. This laser, which produces up to 27 thousand flashes of light per second with an ultra-short temporal bandwidth of few femtoseconds, will be used for the irradiation and investigation of neon in the experiment. Therefore, the following section introduces the principles of such laser pulses and the free-electron lasers used to create them.

2.1.1 Mathematical description of ultra-short laser pulses

The pulse duration, which is aimed at within the framework of the experiment, falls within the range of several femtoseconds (10^{-15} s). A pulse is called 'ultra-short' when its duration lies in the region from pico- to attoseconds (10^{-12} s to 10^{-18} s) [5]. On account of the wave character of light, laser pulses can be described

as a complex space- and time-dependent, linearly polarized electric field, which can be given in either the temporal or the spectral domain. In the following expression for a single-frequency continuous wave, \vec{k} denotes the wave vector and ω refers to the angular frequency [6]:

$$\vec{E}(\vec{x}, t) = \vec{E}_0 \cdot e^{i\omega \cdot t - \vec{x} \cdot \vec{k}}. \quad (2.1)$$

In the non-relativistic dipole approximation $\vec{x} \cdot \vec{k} \ll 1$, this can be reduced to the temporal domain, leading to $E(t)$. For the representation of a pulsed light field, a continuum of frequencies and therefore an electromagnetic wave packet is used. In a first, simplified consideration, the experimental temporal envelope function is approximated by a Gaussian, as illustrated in figure 2.1. $\tilde{E}(\omega)$ is a complex-valued function (indicated by the tilde) that describes the spectral field strength of a pulse. This can be transformed into $E(t)$ by employing Fourier transformation from the spectral to the temporal domain, introduced here with the operator \mathcal{F} . When starting with the real-valued $E(t)$, the inverse \mathcal{F}^{-1} leads to the complex description of the spectral electric field $\tilde{E}(\omega)$, as shown in 2.2 below. As the Fourier transform of a Gaussian again leads to a Gaussian, $\tilde{E}(\omega)$ is also of Gaussian shape. It follows:

$$\tilde{E}(\omega) = \mathcal{F} \{E(t)\} \equiv \int_{-\infty}^{\infty} E(t) \cdot e^{-i\omega \cdot t} dt, \quad (2.2)$$

$$E(t) = \mathcal{F}^{-1} \{\tilde{E}(\omega)\} \equiv \frac{1}{2\pi} \int_{-\infty}^{\infty} \tilde{E}(\omega) \cdot e^{i\omega \cdot t} d\omega. \quad (2.3)$$

Although without physical meaning, the complex representation of the spectrum accounts for negative frequencies as well. Therefore it is to be redefined as $\tilde{E}(\omega)^+$, neglecting all $\omega < 0$. A complex-valued $\tilde{E}^+(t)$ is correspondingly defined in analogy to equation 2.3 by replacing $\tilde{E}(\omega)$ with $\tilde{E}^+(\omega)$. A detailed description of this is given in [7]. Additionally, the complex quantities can be separated in an amplitude and a phase term, where equation 2.4 gives the expression for the spectrum with the spectral amplitude $|\tilde{E}(\omega)|$ and the respective complex-valued phase $\tilde{\Phi}(\omega)$. The field envelope as seen in figure 2.1 is described by $|E(t)|$ which is part of equation 2.5 along with the temporal phase $\Phi(t)$. This reads:

$$\tilde{E}(\omega) = |\tilde{E}(\omega)| \cdot e^{i\tilde{\Phi}(\omega)}, \quad (2.4)$$

$$E(t) = |E(t)| \cdot e^{i\Phi(t)}. \quad (2.5)$$

When used in the experiment and analysed via a spectrometer, the key parameter of a laser pulse is its intensity whereas the phases are not directly measurable. The spectral and temporal intensities are linearly proportional to $|\tilde{E}(\omega)|^2$ and $|E(t)|^2$,

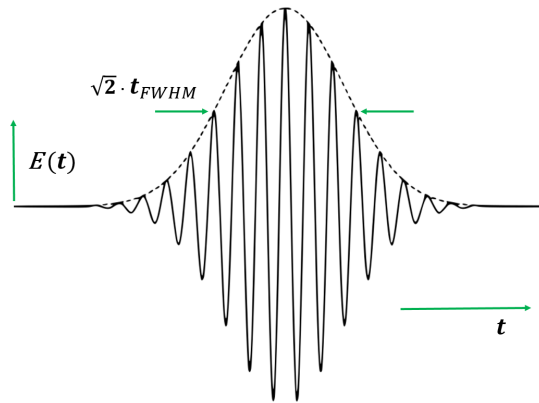


Figure 2.1: Illustration of a Gaussian pulse in temporal domain with dashed line for envelope and temporal pulse duration t_{FWHM} (defined for pulse intensity, hence multiplication by $\sqrt{2}$); taken and adapted from [8]

respectively. $I(t)$ is measured in units of W/cm^2 .

The pulse duration t_{FWHM} at the full width at half maximum (FWHM) of the temporal intensity profile is connected to the Gaussian standard deviation. For laser pulses with the spectral bandwidth ω_{FWHM} , due to the Fourier uncertainty, the limit $t_{\Delta FWHM} \cdot \omega_{FWHM} \geq constant$ holds. The two parameters are inversely dependent on each other; the minimal pulse duration is therefore limited by the maximal spectral bandwidth and vice versa. The case of $t_{\Delta FWHM} \cdot \omega_{FWHM} = constant$ is commonly referred to as the minimum duration–bandwidth product. With this, all the pertinent aspects of laser pulses used in the numeric simulations (see chapter 4), first and foremost the Fourier formalism, are introduced. The reader is advised to consult the referenced book "Ultrashort Laser Pulse Phenomena" for further details (see [7]).

2.1.2 Free-electron lasers

The electromagnetic spectrum comprises the various types of radiation, classified by means of their (central) frequency f , photon energy E_{ph} and wavelength λ . These quantities are connected via the formulae

$$E_{ph} = h \cdot f \quad \text{and} \quad c = f \cdot \lambda, \quad (2.6)$$

incorporating the speed of light ($c = 2.998 \cdot 10^8 \text{ m/s}$) and Planck's constant ($h = 6.626 \cdot 10^{-34} \text{ J/Hz} = 4.136 \cdot 10^{-15} \text{ eV/Hz}$) [9]. If one examines this spectrum on the short-wave side of the visible range, one first finds the ultraviolet region. Dif-

ferent authors define the spectral transitions in various respects, here reference is made to [10]. At a wavelength of around 5 nm which roughly corresponds to $E_{ph} = 250$ eV, the extreme ultraviolet (XUV) spectrum ends. That is where the X-ray range begins, which, in turn, is subdivided into soft and hard X-ray. The boundary between these two domains can be set at 1 Å, i.e. at about 12.4 keV. The soft X-ray range thus includes the K-edge of carbon at 284 eV in the long wavelength regime, followed by that of nitrogen (410 eV), oxygen (543 eV) and eventually neon (870.2 eV). Further examples of elements with K-edges in the soft X-ray spectrum (past neon in terms of energy and the corresponding order) are: Al, Si, Ca, Fe, Ni, Cu; see [10]. Beyond hard X-ray, the spectrum ultimately transitions into gamma radiation at even higher energies.

For an increasing atomic number Z , the photon energy required to release a K-shell electron increases. The core excited state targeted in this experiment lies just below the continuum. For such states, said relation with Z is valid as well. Accordingly, novel laser systems with higher photon energy provide new possibilities for core excitation and ionisation in more complex atoms. This also explains the importance of X-ray lasers in the scope of this experiment: while comparable excitations were only possible for less complex atoms with XUV pulses, the same can now be performed on neon.

For a long time, it was only possible to generate laser pulses in the XUV range. From 2009 onwards, laser facilities such as the *LCLS* in the USA or *SACLA* in Japan were put into operation. These reached energies corresponding to the soft X-ray range for the first time. However, the wavelengths of laser pulses generated by the *EuXFEL* are considerably smaller and thus allow spectral observations in entirely new ranges. The pulses have a duration of a few femtoseconds and can be referred to as 'ultra-short' according to the definition given above. The resulting temporal resolution, along with the high peak intensity of the beam, is a key advantage of the *EuXFEL* for this experiment. Using the concept of undulators as illustrated in figure 2.2, the creation of such a pulse is described in the following. The description of this process is not strictly essential for the numerical simulations in chapter 4, but it is particularly important for the upcoming experiment and thus explained in the following for the *EuXFEL*. [2, 10]

First, a particle source for the entire system provides bunches of electrons at a constant rate. Superconducting accelerators operating at -271°C are used to drive these bunches to relativistic velocities. Next up, the accelerated pulses enter the so-called undulator. A periodically arranged set of magnets forces the electrons on a sinusoidal trajectory; they undulate in transversal oscillation as a result of

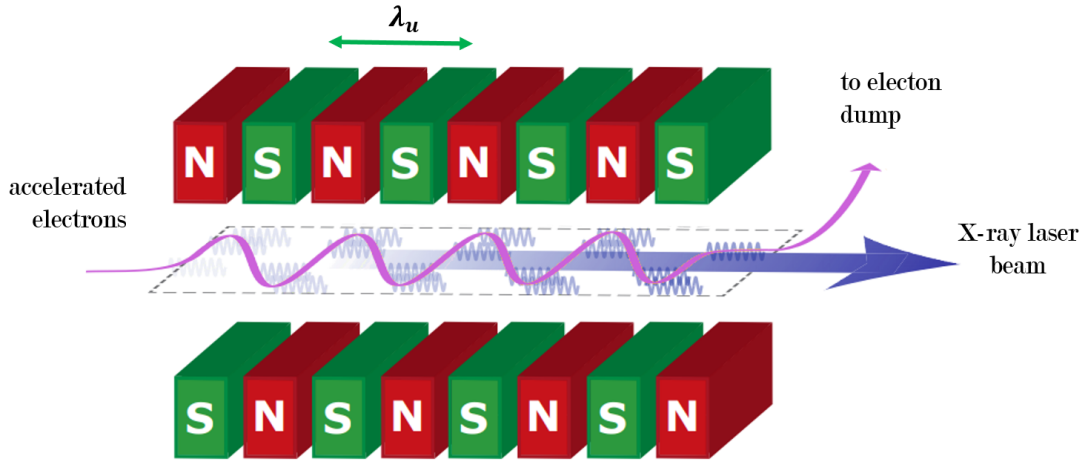


Figure 2.2: Illustration of an undulator with periodically arranged magnets of alternating polarity with period λ_u , sinusoidal electron trajectory in pink (electrons inserted by the accelerator and guided into a dump) and built up X-ray laser beam in blue; taken and adapted from [6]

the Lorentz force. Using the period length λ_u of these magnets, as shown in figure 2.2, the electrons' oscillation wavelength can be calculated via

$$\lambda = \frac{\lambda_u}{2 \cdot \gamma^2} \cdot \left(1 + \frac{K^2}{2} \right). \quad (2.7)$$

In this equation, γ refers to the Lorentz factor $\gamma = (1 - v_e^2/c^2)^{-0.5}$ with the electrons' relativistic velocity v_e . K , the undulator parameter, is expressed via the wave vector of the undulator $k_u = 2\pi/\lambda_u$, the absolute maximum of the magnetic flux density B_0 , as well as charge e and mass m_e of an electron as follows:

$$K = \frac{e \cdot B_0}{m_e \cdot c \cdot k_u}. \quad (2.8)$$

For further explanations and details, the reader is advised to consult [11].

While undulating within the alternating magnetic field, the electrons emit synchrotron radiation in the XUV or X-ray range, clearly peaked into the forward direction. These photons consequently follow a straight trajectory and interact with the slightly slower electrons, thereby the radiation is amplified. This interaction leads to the effect of microbunching, which ultimately results in quasi-coherent laser pulses leaving the undulator at a high repetition rate. Meanwhile, the electrons are forced onto a different trajectory and into a dump. In terms of maximum

photon energy and therefore minimal wavelength, the laser is primarily limited by the gaps between undulator parts and by the kinetic energy of the electron beam. The system must at least be of a certain minimum length; in case of the *EuXFEL*, the entire process described requires over 100 m of undulation. [2, 6]

2.1.3 SASE pulses

In this context and as a final remark, the term self-amplified spontaneous emission (SASE) shall be mentioned briefly. SASE denotes the procedure of utilizing the self-amplification effect of relativistic electrons on a sinusoidal trajectory. This is a consequence of the aforementioned microbunching and utilised to produce ultra-short X-ray laser pulses. Although the range of possible phases for the photons is limited by the effect of microbunching, it is not fixated entirely. As illustrated in figure 2.3, a single SASE pulse is of a randomly spread spiky shape, originating from the stochastic character of the electrons' generation. In the moment of spontaneous emission, the chaotically distributed wavelength of the synchrotron radiation leads to white noise. Only Fourier components which meet said phase condition are amplified. The black curve represents the average of the coloured individual pulses. A Gaussian-like shape can already be surmised here. And indeed, for large numbers of pulses, the distribution converges to such a shape. Taking into account the connection between spectral and temporal width outlined in chapter 2.1.1, it should be mentioned that a spiky structure is also present in the domain of time. As an example, an FEL pulse produced in this manner with a duration of several tens of femtoseconds is to be understood as a train of nearly coherent temporal spikes with widths in the low- or sub-femtosecond regime. [3, 11]

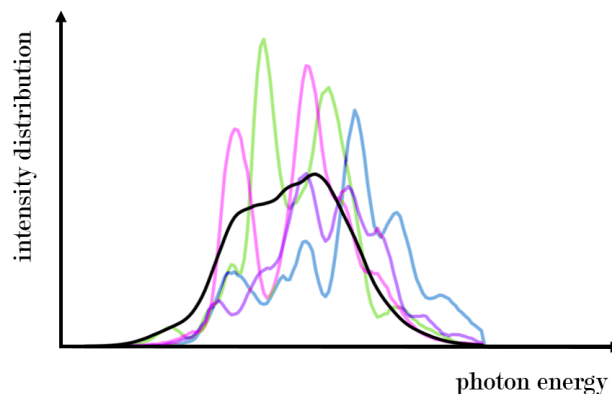


Figure 2.3: Illustration of SASE pulses, differently colored peaky structures result in the black, Gaussian-like spectrum by means of according distribution probabilities, taken and adapted from [11]

2.2 Neon atom

In the course of the experiment on which this thesis is based, neon is to be investigated as the target gas. For this purpose, it is irradiated with an XFEL-laser and the absorption spectrum (see chapter 2.4) is observed. Both for comprehending the configuration of the laser (the photon energy of which is to be in resonance with the core-level $1s \rightarrow 3p$ transition), and to understand the assumptions for the numerical simulation (see chapter 4), a quantum mechanical description of the neon atom is required.

2.2.1 Relevant energy scheme

Neon is an element of group 8 in the periodic table and thus belongs to the noble gases. As an inert gas, it is monatomic, colour- and odourless under normal conditions. While neon is one of the most common elements in the universe, it is rare on earth. Its atomic number Z is equal to 10; the electron configuration in the ground state is therefore given by $1s^2 2s^2 2p^6$. The first ionisation energy of neon, i.e. the energy necessary to strip away a valence ($2p$) electron, amounts to 21.6 eV [12]. The closer an electron is to the nucleus in the shell model, the stronger it is bound. For the ionisation of a K-shell electron, an energy is required, which at least corresponds to that of the K-edge. As mentioned before, this energy level lies at 870.2 eV for the neon atom. The corresponding continuum is indicated by the blue coloured area in figure 2.4. Since the objective of the experiment at hand is to core excite electrons and the targeted state is located just below the K-edge, a schematic illustration of a corresponding three-level neon system is presented in the following. Regarding targeted excitation, the complex 10-electron system is reduced to the consideration of just one electron of the K-shell. The numerical simulation uses only the ground and the core excited state (see chapter 4). As part of the theoretical description of effects that are to be expected in the actual experiment, a third, valence-excited state is appended to the scheme of the here relevant levels.

The energy zero point is defined at the level of the ground state energy of $|0\rangle$. The core excited state $|2\rangle$ is therefore positioned at $\epsilon_2 = 867.5$ eV while the valence excited state $|1\rangle$ lies at $\epsilon_1 = 18.2$ eV. For these three levels, the two coherent couplings are depicted in green. The magnitudes of these dipole couplings $d_{g,e}$ and $d_{v,e}$ are given in atomic units (a.u.), which are discussed in [5]. Additionally and indicated by the blue arrow, photoionisation out of the core orbital can occur, leading to Ne^+ and thus a loss of natural neon atoms in the experiment. [4]

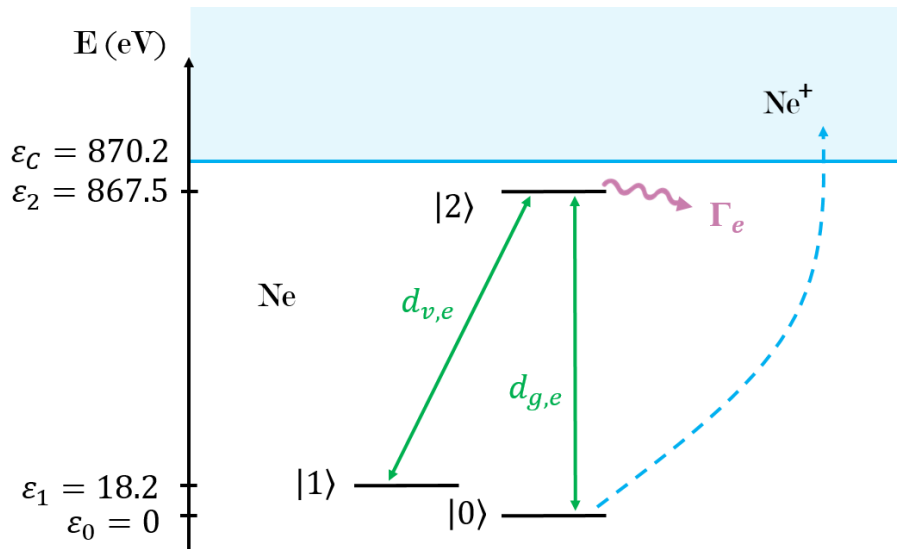


Figure 2.4: Reduced neon model of a neon atom; illustration of energy states $|0\rangle$, $|1\rangle \equiv |2p^{-1}3p\rangle$ and $|2\rangle \equiv |1s^{-1}3p\rangle$, (Auger) decay rate (pink, $\Gamma_e = 0.0099$ a.u.) and dipole coupling (green, $d_{g,e} = 0.0077$ a.u. and $d_{v,e} = 0.048$ a.u.); ionisation by excitation above K-edge (blue); energy and coupling values taken from [13]; scheme taken and adapted from [4]

2.2.2 Auger decay

Generally speaking, the core excited state $|2\rangle$ is short-lived, lasts on femtosecond timescales and can come to its end either by radiative decay or via the Auger process. For more complex atoms with larger numbers of electrons, such as the neon atom, the latter is faster and thus dominant. Also given in atomic units, the Auger decay rate Γ_e therefore denotes the coherent loss of $|2\rangle$. As a result of the excitation by the laser, the K-shell of the atom has an unoccupied $1s$ state, a $1s$ hole. In the process of Auger decay, this vacancy is thereafter filled by an electron of a higher orbital, however not by a $3p$ electron. The energy released during this decay is, in turn, transferred to another particle, the so-called Auger electron. Consequently, the Auger electron leaves the atom; the residual atom is thus ionised [14, 15]. In the simulation of the described neon system (see chapter 4), this dominant decay process constitutes the lifetime of the core excited state. In addition to this, only the states $|0\rangle$ and $|2\rangle$ form the basis of the corresponding model. For these, laser-induced coupling effects (see chapter 2.3.2) are investigated.

2.3 Interaction of laser-pulse and matter

Up to this point, the fundamentals of an ultra-short X-ray laser pulse, as well as that of a natural two-level neon model, have been covered in detail. The gain in knowledge provided by the experiment stems primarily from the observed effects of interaction between such an atom and the electric field of a laser. In order to understand the expected findings on a single atom level, an introduction into the principles of quantum mechanics as well as dressed states and Rabi oscillation is to be given in the following chapters 2.3.1 and 2.3.2. These effects are directly related to the modification of absorption line shapes in the Fano formalism, as will be outlined in chapter 2.4.2.

Additionally, chapters 2.3.3 and 2.3.4 explain the processes of stimulated resonant Raman scattering, self-induced transparency and self-focusing. Although these are not part of the simulations in chapter 4, they are nonetheless important aspects of the upcoming experiment which are thus to be outlined in this section. Up until this point, the theoretical approach is based on the model of a single neon atom. Macroscopically, however, propagation effects such as the ones presented in chapter 2.3.4 take place if laser pulses travel through a dense target gas. Their description is based on the theory work, which was recently published by proposers of this experiment (see [3, 4]).

2.3.1 Principles of quantum mechanics

Quantum mechanics (QM) is to be understood in distinction to classical physics and makes it possible to characterise and predict processes on a (sub-)atomic level. In this context, the Schrödinger equation (SEQ) is a central tool. Erwin Schrödinger deduced a partial differential equation that describes the probabilistic dynamics of a QM state for non-relativistic systems. Such states are a means of modelling the dynamics of wave packets or particles and are usually expressed as $|\Psi(x, t)\rangle$. The SEQ reads:

$$i \hbar \cdot \frac{\partial}{\partial t} |\Psi(x, t)\rangle = \mathcal{H} \cdot |\Psi(x, t)\rangle. \quad (2.9)$$

In the reduction to the solely position dependent case, the SEQ is an eigenvalue equation with N normalised eigenstates $|\Psi_n(x)\rangle$. The Hamilton operator \mathcal{H} is used to characterise the energy of the system and can be described as a quadratic matrix of dimension N . The energies of said eigenstates, E_n , are thus equal to the

eigenvalues of the Hamiltonian:

$$\mathcal{H} \cdot |\Psi_n(x)\rangle = E_n \cdot |\Psi_n(x)\rangle. \quad (2.10)$$

Moreover, the respective stationary eigenstates form an orthogonal system. The aforementioned matrix formalism is used in chapter 4, where the numerical simulation based on solving the SEQ for the two-level neon system is presented. An analytical solution is only possible for the hydrogen atom (and similar one electron atoms). Helium with atomic number $Z = 2$ is already too complex and neon therefore even more so. Thus, approximations, a numerical approach or a combination of both are necessary.

The main challenge now is to define the Hamilton operator appropriately such that the SEQ yields the solution to the QM problem at hand. When describing one electron in an atom, the Hamiltonian is given by the sum of the kinetic energy and the bound electrostatic potential. The resulting eigenstates are propagated in time via equation 2.11 which incorporates their respective discrete energy values E_n (with the ground state for $n = 0$, and growing values for increasing n):

$$|\Psi_n(x, t)\rangle = e^{-iE_n \cdot \frac{t}{\hbar}} \cdot |\Psi_n(x)\rangle. \quad (2.11)$$

Furthermore, each state can be expressed as a superposition of the resulting eigenstates:

$$|\Psi(x, t)\rangle = \sum_n [c_n \cdot |\Psi_n(x, t)\rangle]. \quad (2.12)$$

Here, the coefficients can be determined via $c_n = \langle \Psi(x, t) | \Psi_n(x, t = 0) \rangle$ and lead to the state's population probability $P_n = |c_n|^2$. Finally, the normalization condition $\sum_n P_n = 1$ must be met. All of the above is also applicable for electronic states in a neon atom, which will be investigated in chapter 4. For a more detailed description and the inclusion electron-electron interaction into Hamiltonian for multi-electron systems, the reader is referred to [5, 9, 15].

2.3.2 Dressed states and Rabi oscillations in strong-field regime

In order to describe the near resonant coupling of the main excitation transition ($1s \rightarrow 3p$) in the neon atom, the scheme in figure 2.4 is now reduced to the states $|0\rangle$ and $|2\rangle$. The same applies to the numerical simulation in chapter 4. The valence excited state and the neon ion are, however, included in the later sections 2.3.3 and 2.3.4. The Hamiltonian used to describe the interaction of light and matter is

based on the involved electronic eigenstates, $1s$ and $3p$, as diagonal entries and the laser-induced dipole coupling of these two states for the off-diagonal elements. In the case of weak fields, i.e. a low-intensity laser pulse, a perturbation description is not required; the atomic contribution to the Hamiltonian is therefore sufficient. In contrast, strong fields are used in this experiment. Accordingly, a strong interaction is to be expected, leading to an oscillation of the state populations with the so-called Rabi frequency Ω'_R . As seen in equation 2.13, the Rabi frequency is expressed via the product of the electric field $E(t)$ and the aforementioned dipole coupling factor $d_{g,e}$. It should be noted, that the analytical description is only valid for monochromatic lasers. Although the numerical simulation is based on ultra-short and thus broadband laser pulses, the following theory findings are still applicable in chapter 4. The Rabi frequency is expressed as follows:

$$\Omega'_R = \frac{E(t) \cdot d_{g,e}}{\hbar}. \quad (2.13)$$

'Dressed states' refers to energy levels of the laser coupled system that are shifted with respect to the bare atomic states. As long as the laser field is present, these also represent the eigenstates of the total Hamiltonian. The coupling is caused by a laser with photon energy E_{ph} . This is where the concept of detuning should be introduced briefly, which is denoted by Δ and refers to the offset of E_{ph} from the excitation energy E_e . For the previously described neon system, the following is valid: $E_e = \epsilon_2 = 867.5 \text{ eV}$. Consequently, $\Delta = E_e - E_{ph}$ applies, whereby in the case of resonance, Δ is equal to 0. The chase of the laser's photon energy lying below that of the resonance ($\Delta < 0 \text{ eV}$) is referred to as red detuning (longer wavelength). The opposite case ($\Delta > 0 \text{ eV}$) is in turn called blue detuning (shorter wavelength).

The configuration of the dressed states E^\pm , generated by an intense laser, is illustrated in figure 2.5. Which of the two bare states becomes which of these dressed states depends on the detuning. When irradiated by a blue-detuned pulse, the ground state translates into E^+ and is therefore virtually shifted above the atomic excited state. The latter, in turn, translates into E^- (see figure 2.5 b)). Conversely, bare ground and excited state for red detuning transition into E^- and E^+ respectively (see figure 2.5 a)). For the established case of $\epsilon_0 = 0$ for $|0\rangle$ and incorporating the generalized Rabi frequency $\Omega_R = \sqrt{\Delta^2 + \Omega'^2_R}$, the new energy values can be expressed as follows:

$$E^\pm = \frac{E_{ph} + E_e}{2} \pm \hbar \cdot \Omega_R. \quad (2.14)$$

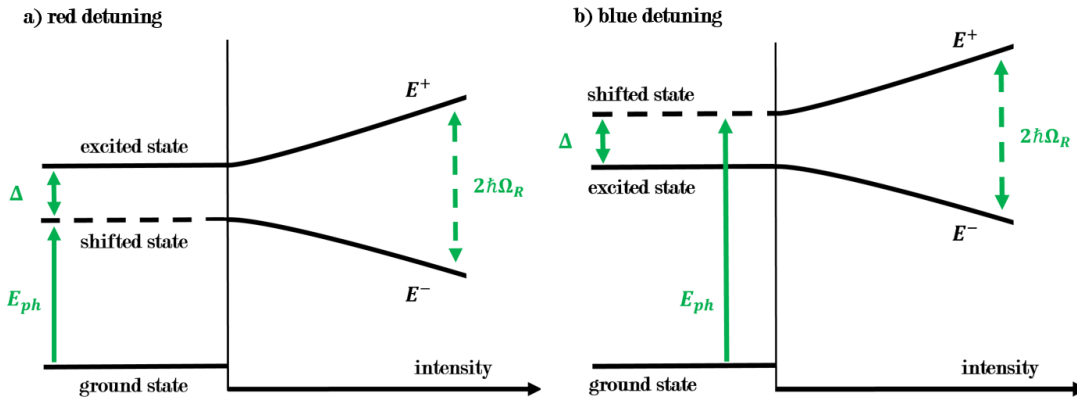


Figure 2.5: Illustration of formation and location of dressed states for **a)** red and **b)** blue detuning Δ ; interaction of laser field and two-level system with unperturbed ground and excited state on each left side with vertical energy axis; splitting of states in E^\pm in proportion to Rabi frequency Ω_R according to equation 2.13 for increasing intensity of dressing laser pulse with photon energy E_{ph} ; adapted from [17]

This energetic repositioning occurs only during the interaction with the ultra-short laser pulse. Due to the dependency of the Rabi frequency on $E(t)$, Ω_R is consequently dependent on the intensity of the laser. As the values of E^\pm are, in turn, connected to Ω_R , the repositioning depends on the laser's intensity, i.e. on its envelope. Hence, for a Gaussian pulse, the shift in the energy spectrum is of Gaussian shape as well. After the interaction process, both bare states end up having collected a phase shift. This, in turn, results from their shifted energy compared to the bare atomic energies and phases. Thus, the phase of the atomic dipole response is changed as well, which is referred to in chapter 2.4.2 for the modification of absorption line shapes. [5, 16]

Up to this point, only the spectral properties of the laser dressed and coupled two-level system were discussed. In the temporal domain, Rabi oscillation arises in the population probabilities of the ground and excited states (P_g and P_e , respectively). $P(t)$ for the two states follows a (co)sinusoidal curve between 0 and 1, whereby the two curves' oscillation is offset by half a phase. This is of key importance for the analysis of population inversion, as introduced and conducted in chapter 4.3 to explain the occurrence of resonant amplification of light. [17]

2.3.3 Stimulated resonant Raman scattering

In the following, the valence excited state $|1\rangle$ from figure 2.4 is included in the theoretical description, i.e. a three-level system is considered. At high intensities, so-called Raman scattering (RS) occurs between the states $|1\rangle$ and $|2\rangle$ (coupled with the dipole moment $d_{v,e}$). This scattering process of the X-ray laser's photons and the atoms results in energy transfer and is therefore inelastic. In contrast to elastic Rayleigh scattering, the frequency and thus photon energy (see equation 2.6) of the scattered photons changes.

A further distinction must be made between Stokes-RS and anti-Stokes-RS. In the former, energy is being transferred from the photon to a scattering molecule. After this process, the molecule is at a higher energy level than it previously was. In the latter case, rotational and vibrational energy of the molecule is passed on to the photon, which thereupon moves at a higher speed. In the experiment with monatomic neon, there are of course no molecular vibrations. Instead, the energy transfer is carried out via (Raman-like) electronic excitation in the valence shell.

For the introduced neon system, the photon energy of the laser is close to that of the electrical transition between $|1\rangle$ and $|2\rangle$. With a sufficient spectral bandwidth (FWHM above ~ 10 eV), photons with $\epsilon_2 - \epsilon_1 = 849.3$ eV are present in the pulses of the XFEL. These photons can drive the RS process, which is therefore

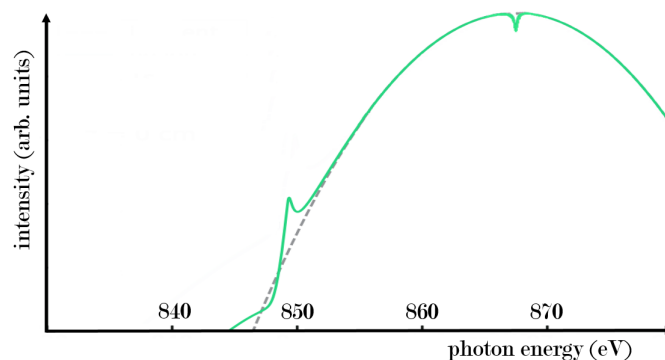


Figure 2.6: Spectral results of X-ray pulse centred around $1s \rightarrow 3p$ transition energy $\epsilon_2 = 867.5$ eV, propagating through neon gas at high intensity with incident spectrum illustrated via dotted grey line, transmitted spectrum in green; dip in transmitted spectrum resulting from resonant absorption at ϵ_2 ; peak at 849.3 eV due to stimulated resonance RS; excluding absorption by $1s$ -photoionisation above 870.2 eV; taken and adapted from [4]

called stimulated resonant RS in contrast to the otherwise spontaneous scattering. Within the context of the experiment, the described concepts lead to stimulated emission. Positioned at the energy level of the $2p \rightarrow 1s$ transition, formation and growth of a peak can be observed in the spectrum of transmitted light. This only occurs at higher intensities and can be seen in figure 2.6. [3, 15]

2.3.4 Self-induced transparency and self-focusing

From this point on, a gas of neon atoms is considered instead of a single atom. In the upcoming experiment, propagation effects are to be measured. For this purpose, it is necessary that the electric field of the laser interacts with a large number of atoms. Accordingly, the gas through which the pulses propagate must be at a sufficiently high pressure (more on this in chapter 3.7).

When a laser pulse passes through a resonant medium, Lambert-Beer's law states that part of the photon energy is absorbed as a result of state excitation (see equation 5.2). The energy would decay exponentially and ultimately reach zero. The phenomenon of self-induced transparency describes the propagation of a strong ultra-short light pulse through a resonant medium without significant energy loss in said manner. The transit time exceeds the expectation on account of the lower attenuation. This mechanism is caused by the constant absorption and re-emission of radiation by resonant atoms. After the pulse's propagation, their excited dipoles all remain in phase. Therefore, they coherently return power back into the electric field. Self-induced transparency is the reason why the laser pulse is still present after several millimetres of propagation through neon gas and can be observed for further analysis.

Resonant x-ray self-focusing occurs at high intensities. In the course of the laser's propagation through the cell, the beam size is strongly reduced. Consequently, the on-axis electric field grows. The reason for this effect is an induced change of the refractive index in the gas, triggered by the electromagnetic field. This in turn, influences the propagation of the field. On-axis and off-axis fields interact in different ways.

Further information on this as well as other linear and non-linear effects is provided by Kai Li and Linda Young in [4]. A detailed analysis of the processes involving ionisation and the Ne^+ system is also presented in their text. The additional energy levels and transitions of the ion also influence the phenomena described in this section of the theory chapter. They are, however, beyond the scope of this thesis and the numerical simulations in chapter 4.

2.4 Absorption spectroscopy

In this chapter of the theoretical introduction, the method of absorption spectroscopy (AS) is presented. As stated in the preface, X-ray transient absorption is to be investigated within the framework of the experiment. The interaction effects of high-intensity laser propagation through neon gas, which are described in the previous chapter, can be detected and studied employing X-ray transient AS. During the experiment's realization in Hamburg, this will be achieved with the help of a dispersive grating spectrometer provided by Jan-Erik Rubensson's group from *Uppsala University* [3].

2.4.1 Spectral absorbance and optical density

At the SQS end-station of the XFEL, the incident spectrum of the XFEL-laser pulse with intensity profile $I_0(\omega)$ is acquired and thereafter compared to the transmitted spectrum $I(\omega)$. The latter is detected by the dispersive grating spectrometer (combined with an X-ray streak camera). $I(\omega)/I_0(\omega)$ leads to the linear absorption spectrum; this fraction is referred to as the transmission $T(\omega)$, while $A(\omega) = 1 - T(\omega)$ denotes the spectral absorption. [5]

Between the two measurements, the pulse passes through the target gas with the atomic number density ρ_N and interaction length l . The following expression describes the optical density (OD), a quantity which is used for the measurement of characteristic spectral properties of atoms or molecules, concerning their interaction with light. As a central part of the analysis of the numerical simulation results in chapter 4, the resonance lines are studied using this concept:

$$OD(\omega) := \log_{10} \left[\frac{I(\omega)}{I_0(\omega)} \right] = \frac{\sigma_a(\omega) \cdot \rho_N \cdot l}{\ln(10)}. \quad (2.15)$$

Here, σ_a refers to the absorption cross section which is a measure for the probability of an absorption process and thus serves the purpose of quantifying the likelihood for light-matter interaction during the propagation of the XFEL-pulse through neon. The derivation of its expression in equation 2.17 can be found in appendix A.1 and in [5]. However, to comprehend the initial step of the appended remarks, the concept of polarisation must be outlined first:

Light, which propagates through matter, excites the atoms and leads to a change of the dipole moment, the property that characterises the separation of electrical charges in space. The single atom dipole response $d(\omega)$ relates to the macroscopic

polarisation P via the atomic number density ρ_N . For a dilute medium, $P(\omega)$ can also be stated as a function of the driving electric field $E(\omega)$ and the dielectric susceptibility $\chi(\omega)$. Furthermore, ε_0 refers to the electric permittivity in a vacuum. It follows:

$$P(\omega) = \rho_N \cdot d(\omega) = \varepsilon_0 \cdot \chi(\omega) \cdot E(\omega). \quad (2.16)$$

Finally, the derivation in A1 leads to:

$$\sigma_a(\omega) = \frac{\omega}{c \cdot \varepsilon_0} \operatorname{Im} \left[\frac{d(\omega)}{E(\omega)} \right]. \quad (2.17)$$

Just as is the case for equation 2.15, the division within the brackets in 2.17 can be regarded as a mathematical description of the interference between the incoming and the outgoing signal. The dipole response and the electric field are characteristic for the atom and the laser pulse respectively. Their interaction leads to a relative shift in phase, thus resulting in said interference. Understanding this and as a basis for the numerical simulation described in chapter 4, the following equation for the OD is given as well (a detailed derivation can be found in [5]):

$$OD(\omega) = -\log_{10} \left[\frac{|E(\omega) + i\eta \cdot d(\omega)|^2}{|E(\omega)|^2} \right]. \quad (2.18)$$

Here, η refers to the number of atomic emitters, whereby $\eta \ll 1$ can be expected for dilute media. In considering this rewritten expression for the OD, the aforementioned interference connection can now be recognised clearly. The numerator contains the electric field as well as the atoms' dipole response, the denominator only the former. For a given electric field, knowledge of $d(\omega)$ is thereby sufficient to calculate the OD. This is done as a central part of the simulation method. Additionally, one can use the spectral OD to extract information about the temporal dipole response, which will be introduced in the following chapter. [5]

2.4.2 Absorption line shapes and interferometric dipole phase shifts

The interference formalised in equation 2.18 is associated with a time-dependent phase shift $\Delta\phi$ of the dipole response. The phase shift can, for example, be the result of the energy level displacement for the dressed states explained in chapter 2.3.2 in connection with Rabi oscillation. It can be related to the so-called Fano parameter q , as is described and experimentally proven in [18]. The parameter characterises the asymmetry of a resonant absorption line and leads to a varied

absorption cross section according to:

$$\sigma_{Fano}(E) = \sigma_0 \cdot \frac{(q + \epsilon)^2}{1 + \epsilon^2}. \quad (2.19)$$

Here σ_0 denotes the cross section far away from the resonance and E refers to the photo energy (see equation 2.6). The reduced energy ϵ includes position E_r and width Γ of the resonance as well as Planck's constant $\hbar = h/2\pi$ and can be expressed as:

$$\epsilon = \frac{2 \cdot (E - E_r)}{\hbar \cdot \Gamma}. \quad (2.20)$$

Generally, the dipole response to excitation results in characteristic line shapes observed by means of AS. For instance, the symmetric Lorentz line is the consequence of the exponential decay of discrete excited states with finite lifetimes. A peak in the spectrum of the cross section, i.e. an absorption line formalised by q , represents strong light-matter interaction and thus significant absorption. As derived in the aforementioned article, the correlation of the Fano parameter and $\Delta\phi$ is given by:

$$\Delta\phi(q) = 2 \cdot \arg(q - i), \quad q(\phi) = -\cot\left(\frac{\Delta\phi}{2}\right). \quad (2.21)$$

Figure 2.7 illustrates different line shapes in relation to q and $\Delta\phi$. For this thesis, it is crucial to understand that the 'typical' Lorentzian line shape known from a simple two-level electronic transition is part of this Fano formalism. It corresponds to $\Delta\phi$ in convergence to integer multiples of 2π (and $q \rightarrow \pm\infty$). For odd multiples of π ($q = 0$), so-called window resonance occurs, leading to negative values for the absorption cross section and thus to amplification of resonant light. The analysis of the simulation results in chapter 4 is focused on the investigation of this phenomenon. The term 'window resonance' is thereby used to refer to the general case of symmetrical resonant absorption lines with a negative amplitude.

Furthermore, the phase can be shifted deliberately by coupling two states with an intense laser pulse. For the experiment described in [18], a pulse in addition to that for the state's excitation was used to change in the Fano parameter. In the course of this thesis, however, the possibility to control the absorption process using only one high-intensity laser pulse is examined. By changing the line shape, absorption can be converted into gain in a targeted manner. Two examples for transitions between absorption line shapes are indicated by the green and pink arrows in figure 2.7. Finally, an induced change from symmetrical Lorentz to asymmetrical Fano line shape is presented in figure 2.8.

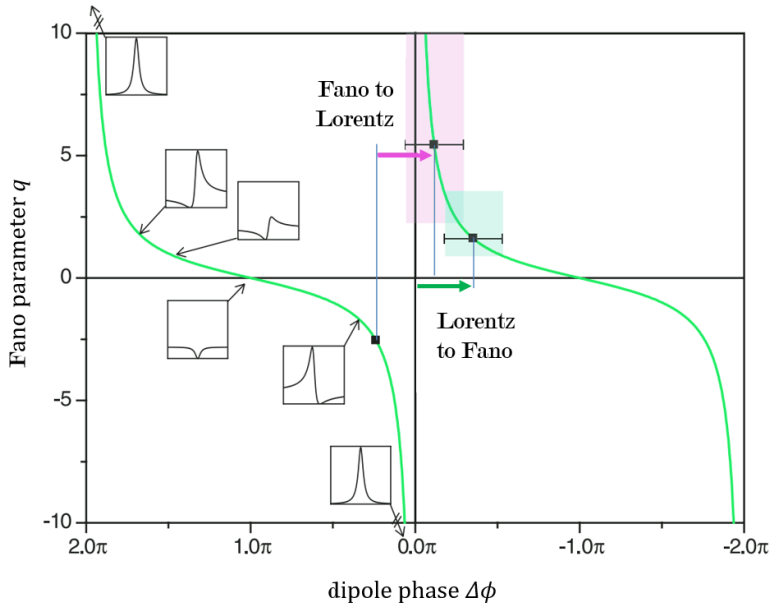


Figure 2.7: Relationship between Fano parameter and dipole phase, according to equation 2.21; with exemplary absorption line shapes in small boxes and two examples of phase shifting; taken and adapted from from [18]

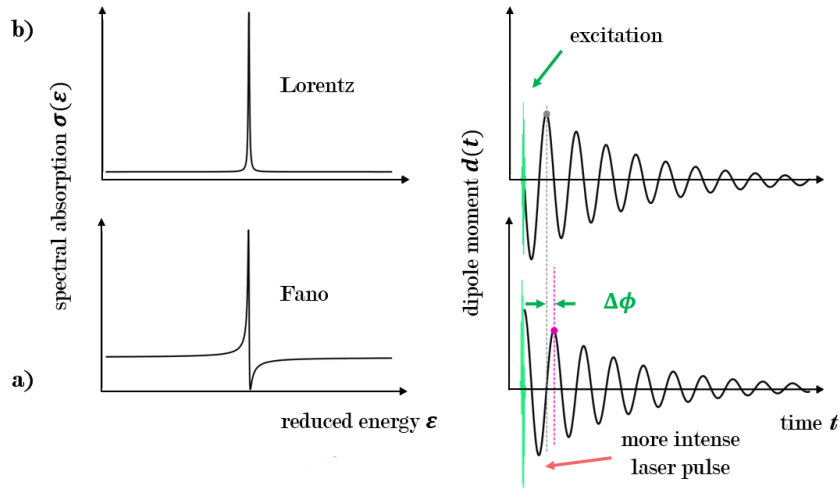


Figure 2.8: Illustration of laser excitation resulting in decaying dipole response and characteristic symmetric Lorentz absorption line in **a)**; shift of phase induced by more intense laser and transition to asymmetric Fano line shape in **b)**, corresponding to green arrow in figure 2.7; taken and adapted from [18]

2.5 Physics of vacuum and gas flow

This last subsection of the theoretical introduction covers the topic of gas flow (GF) and outlines the laws of vacuum physics. Furthermore, it serves as a basis for the theory comparison in chapter 3. The neon gas under examination is fed into the apparatus via a special control system. It then flows out through the two holes of the target cell into the evacuated space of the setup's main and pre-chambers. A turbo pump is mounted onto each of these compartments in order to assure high vacuum conditions. This is, in turn, necessary to guarantee that the laser propagates unhindered through the system prior to and after the neon interaction. Instead of adjusting the laser's peak intensity, the pressure within the target cell will serve as the key control parameter.

The information presented in this chapter is primarily based on the book "Building Scientific Apparatus - A Practical Guide to Design and Construction" ([19]). Chapter 3.2 of said book outlines the GF in vacuum chambers.

2.5.1 Average velocity and types of flow

Without an external gas supply, the targeted pressure in the experimental structure is in the order of 10^{-8} mbar (high vacuum). Since different gases behave differently when flowing, the description of the average velocity as stated by Maxwell-Boltzmann shall be given first. A transfer of energy and momentum occurs for gas molecules that are enclosed in a chamber. This leads to a distribution of velocity with a maximum at the most likely value. According to the kinetic theory of gases, the following applies for the average velocity of a particle that is part of an ideal gas at the temperature T :

$$\bar{v} = \sqrt{\frac{8 \cdot k_B \cdot T}{\pi \cdot M}}. \quad (2.22)$$

In this expression, $k_B = 1.381 \cdot 10^{-23}$ J/K denotes the Boltzmann constant and M refers to the molecular weight. It is to be mentioned that the assumption of an ideal gas does not reflect reality in a perfect manner. This would only apply in the case that the gas particles do not interact amongst each other. However, this description is sufficiently precise within the scope of the desired accuracy.

In areas of higher pressure (low vacuum: from over 100 mbar to about 1 mbar), collisions of the gas particles occur frequently, while hardly any take place with the wall of the chamber. This is the area of viscous flow, where a further distinction is made between laminar and turbulent flow. If medium vacuum is present (down

to about 19^{-3} mbar), the so-called Knudsen flow constitutes a transitional regime. Starting in the subsequent vicinity of high vacuum, molecular flow occurs; the particles scarcely interact with each other and travel almost unhindered within the confines of the chamber. The distinction between these types of GF is of great significance for the choice of the appropriate conductance and is visualised in figure 2.10 following the introduction of said parameter. Additionally, a table summarising the listed types of GF and vacuum as well as the pressure ranges can be found in [20].

2.5.2 Parameters and equations of gas flow

To understand the characteristics of GF, the following quantities are essential. The net (pumping) speed $S \equiv dV/dt$ is given in the units of a flow rate: L/s. It describes the rate of volume flow with respect to a cross section inside a chamber or a tube and is equal to the throughput Q divided by the inlet pressure. The capacity of a pump is defined accordingly: $S_p \equiv dV/dt$. The throughput $Q \equiv P \cdot S$, in turn, corresponds to the pumped flow rate and can be expressed in units of $\text{Pa} \cdot \text{m}^3/\text{s}$. For this, the values of the pressure P and the net speed S are to be measured in the same location. Lastly, the conductance C of a tube or an aperture is characterized as an inverse resistance value for GF. It describes the capacity of a line or an opening to allow the passage of gas and can therefore be regarded in analogy to Ohm's law, again in units of the net speed. This leads to the following description of the throughput Q with pressure decreasing from P_1 to P_2 along a tube with conductance C :

$$Q = (P_1 - P_2) \cdot C. \quad (2.23)$$

For a benchmark vacuum system as illustrated in figure 2.9, consisting of a chamber, a tube and a pump, the GF can be described mathematically via the so-called master equation (see equation 2.25 below). The following expressions for the system's net speed S as well as the capacity of the pump S_p are used for the derivation of said equation, which links these parameters to the conductance:

$$S = \frac{Q}{P_1}, \quad S_p = \frac{Q}{P_2}. \quad (2.24)$$

By substituting both pressure values in equation 2.23, these expressions lead to the master equation:

$$\frac{1}{S} = \frac{1}{S_p} + \frac{1}{C}. \quad (2.25)$$

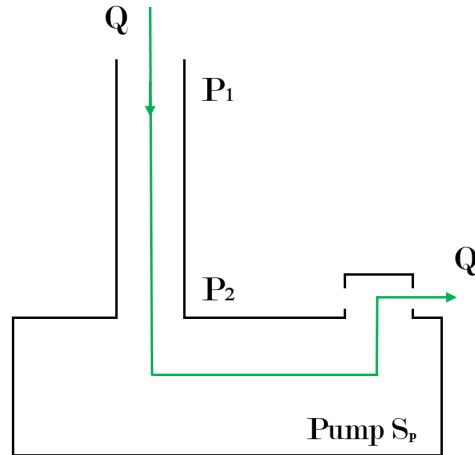


Figure 2.9: Simplified illustration of vacuum system with tube, throughput Q , decreasing pressure ($P_1 > P_2$) and pump with capacity S_p ; green arrow illustrates direction of GF; adapted from [19]

Assuming that there is only one source of gas in the system, the throughput Q is constant in all its parts which ultimately leads to:

$$S \cdot P_1 = S_p \cdot P_2 = Q. \quad (2.26)$$

2.5.3 Equations of conductance

Building on the specifications for a simple vacuum system above, a brief remark should be made about the network equations. These allow the description of a more complex system of n single conductances C_i employing one generalized value for the conductance from the source of a gas to the pump. Analogous to the laws of electrical resistance, the following applies to parallel and serial networks:

$$C_{parallel} = C_1 + C_2 + C_3 + \dots = \sum_{n=1}^N C_i, \quad (2.27)$$

$$C_{series} = \left[\frac{1}{C_1} + \frac{1}{C_2} + \frac{1}{C_3} + \dots \right]^{-1} = \left[\sum_{n=1}^N \frac{1}{C_i} \right]^{-1}. \quad (2.28)$$

For the description of the experiment in chapter 3, it is sufficient to consider the viscous and the molecular flow region. The key difference is that the conductance in the former region is dependent on pressure, whereas in the latter it is not. This can be seen in figure 2.10 below. For both cases, the formulas for a tube and

for an aperture are given in the following. For the tube, a circular cross section is assumed; the parameters D (diameter) and L (length) are given in units of cm, the area A , in the aperture case, in cm^2 . This so-called thin aperture occurs whenever a barrier with a hole of diameter greater than the thickness of the wall separates two regimes of different pressure.

Equations 2.29 and 2.30 describe the case of viscous flow for dry gases at room temperature (293 K). The former follows the Hagen–Poiseuille law and is applicable provided that no turbulence occurs. They read:

$$C_{tube} \left[\frac{\text{L}}{\text{s}} \right] = 24450 \cdot \frac{D^4}{\eta \cdot L} \cdot P_{av}, \quad (2.29)$$

$$C_{aperture} \left[\frac{\text{L}}{\text{s}} \right] = 20 \cdot A. \quad (2.30)$$

Here, η is equal to the dynamic viscosity of the gas (in units of micropoise μP) and P_{av} denotes the average pressure inside the tube (in mbar).

Additionally, equations 2.31 and 2.32 help to calculate the conductance in the range of molecular flow. As mentioned before, in this case, the conductance is not dependent on the pressure anymore. There is instead a dependency on the temperature T and the molecular weight M . The parameter \bar{v} again refers to the gas particles' average velocity (in cm/s). It follows:

$$C_{tube} \left[\frac{\text{L}}{\text{s}} \right] = 2.6 \cdot 10^{-4} \cdot \bar{v} \cdot \frac{D^3}{L}, \quad (2.31)$$

$$C_{aperture} \left[\frac{\text{L}}{\text{s}} \right] = 3.7 \cdot \sqrt{\frac{T}{M}} \cdot A. \quad (2.32)$$

Once the conductances have been determined via these formulae, the network equations can be used to calculate a single conductance for the system. This helps to estimate the pressure ratios which should be done prior to the installation of vacuum pumps and chambers in order to avoid inefficient application.

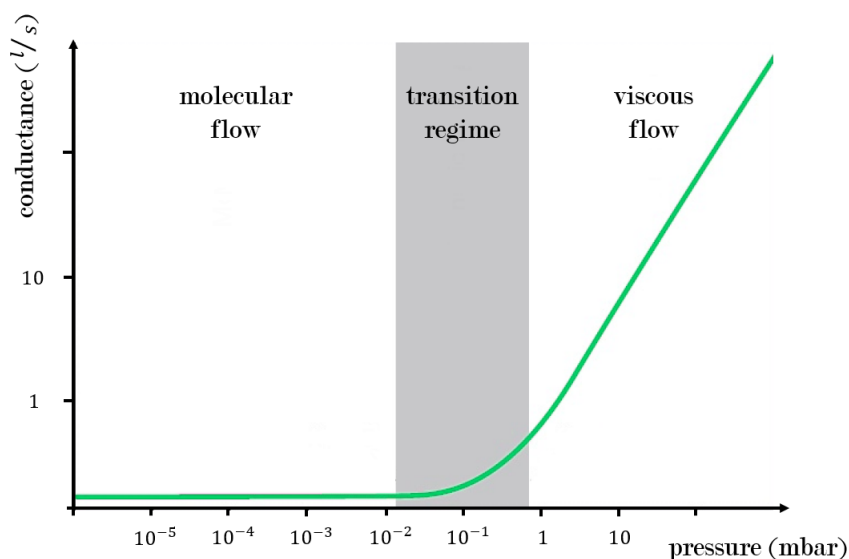


Figure 2.10: Illustration of conductance value in relation to pressure for distinction of different types of GF (see chapter 2.5.1); exemplary for smooth pipe; C constant for molecular flow, linearly dependent on pressure for viscous flow after transition regime; taken and adapted from [20]

2.5.4 Important gas-type dependent parameters

Finally, the dynamic viscosity η , molar mass M and average molecular velocity \bar{v} for the gases nitrogen (N_2), neon (Ne) and argon (Ar), are given here. These are relevant for the later calculation of the pressure ratios in chapter 3 and the comparison of different types of gases. For the pressure range in the context of which the dynamic viscosity is used, i.e. in the viscous flow range, its value can be approximated as pressure-independent. The temperature-dependency can be neglected as well since room temperature is assumed in all cases.

Gas type	η [μP]	M [10^{-26} kg]	\bar{v} [10^4 cm/s]
N_2	166	4.65	4.707
Ne	297	3.35	5.546
Ar	210	6.63	3.942

Table 2.1: Gas-type dependent parameters for later calculation of conductances for N_2 , Ne and Ar; taken from [12, 21]

3 Experimental setup

Starting from this chapter on, the main part of the thesis, including the project's results, commences. Here, the practical aspects of the experiment are covered, while chapter 4 presents the numerical simulation. Whereas in the latter, the intensity of the simulated laser serves as the main control parameter, the focus here lies on the GF, depending on the input pressure for the target cell. The precise control of this pressure is a key challenge and requires special attention.

First, in chapter 3.1 a rough overview of the setup structure is provided; this refers to the vacuum chamber system including the pumps and the corresponding pre-vacuum system. In chapter 3.2, the neon gas supply system is explained, followed by a characterisation of the corresponding pressure control valve in chapter 3.3. Furthermore, chapters 3.4 to 3.6 describe the pressure measurements that were carried out and refer back to the theory of GF from chapter 2.5. Here, a central comparison of the experimental data with the theoretical expectations is made, whereby the model with the best agreement with reality is to be found. The dependence of the pressure conditions on the target cell hole diameter and the type of gas is examined in this context. Concluding the description of the experimental setup, chapter 3.7 outlines options of optimisation and provides an outlook for the upcoming beamtime.

3.1 Structural overview of the vacuum system

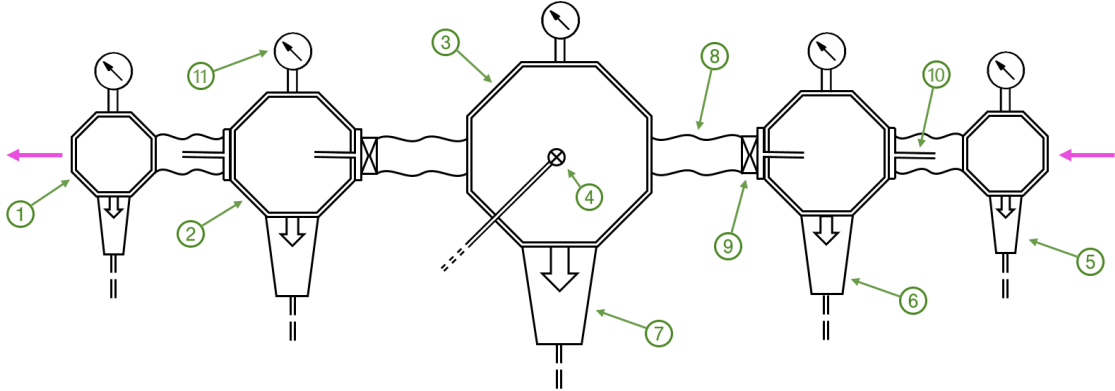


Figure 3.1: Scheme of experimental setup for vacuum chamber system; propagation direction of laser beam indicated by pink arrows, entering from right side (XFEL), heading into spectrometer on left side; components (individual labelling refers to any identical part):

- ① Outer and smallest differential-pumping pre-chambers
- ② Inner and medium-sized differential-pumping pre-chambers
- ③ Main chamber with target cell ④ for neon supply
- ⑤ *Pfeiffer Vacuum* HP-80 turbo pumps for outer pre-chambers
- ⑥ *Pfeiffer Vacuum* HP-300 turbo pumps for inner pre-chambers
- ⑦ *Pfeiffer Vacuum* HP-2300 turbo pump for main chamber
- ⑧ *Metallic Flex* welded bellows for chamber connection
- ⑨ *VAT* gate valves for pressure segregation
- ⑩ Pumping stages with reduced diameter for pressure reduction
- ⑪ *Pfeiffer Vacuum* full range gauges for pressure measurement

The general procedure of the experiment has already been outlined several times throughout this thesis. With the help of figures 3.1 and 3.2, it will now be explained in more detail. The *EuXFEL* first produces laser pulses as described in chapter 2.1. These are guided into the illustrated chamber system. In the main chamber, the pulses enter the target cell and interact with the gas under examination, in this case, neon gas. Its supply is described in chapter 3.2. The cell has small openings that allow the laser to pass through and be focused to the centre with the highest pressure. Pulses thus propagate through a few millimetres of gas and are not absorbed in their entirety. This is important in order to analyse the resulting light by means of absorption spectroscopy. To ensure this, the pulses must be enabled to exit on the other side of the system, where the spectrometer is connected. Overall,

3 EXPERIMENTAL SETUP

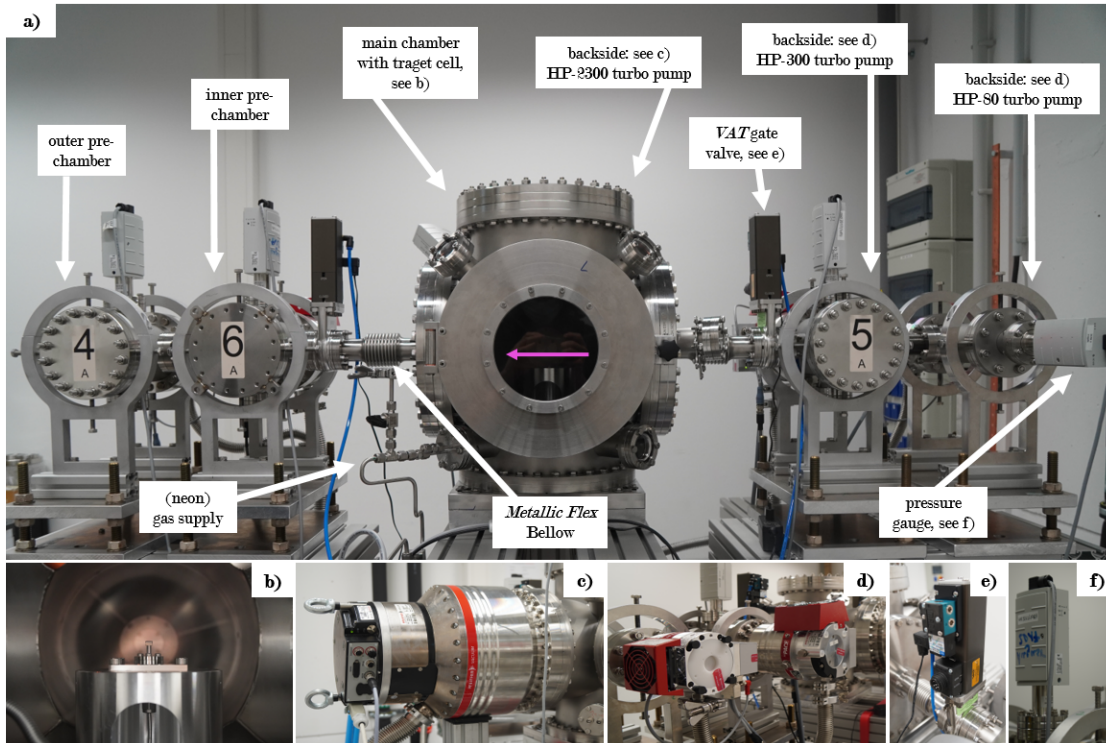


Figure 3.2: **a)** Photograph of experimental setup for chamber system with labelled components, laser beam direction indicated by pink arrow
b) Target cell in main chamber
c) *Pfeiffer Vacuum* HP-2300 turbo pump for main chamber
d) *Pfeiffer Vacuum* HP-80 turbo pump for outer pre-chambers (left) and HP-300 turbo pump for inner pre-chambers (right)
e) *VAT* gate valve
f) *Pfeiffer Vacuum* full range pressure gauge

it is of utmost importance that the pulse moves through a high vacuum with the exception of the target cell. Otherwise, scattering and absorption effects of the residual gas would prevent the beam from reaching both target and spectrometer. For this purpose, a differential pumping system consisting of several individual chambers, each with its own turbo molecular pump and pressure gauge, has been constructed. Before going into more detail on the characteristics of the utilised pumps in chapter 3.1.1, a few more general remarks are in order.

All connections of the system shown are sealed using copper flanges (CF). This well-proven method guarantees the build-up of high vacuum. In order to separate the main chamber vacuum from that of the pre-chamber system, pneumatic *VAT*

gate valves are installed on both sides. In inactive state, the valves are closed; they can be controlled electronically and are opened by means of compressed air. Since the barrier contains a window, an alignment laser can still be sent through the entire system.

Pumping stages are installed in between all chambers as additional resistances in order to guarantee the lowest possible pressure values apart from the target cell. The reduced diameter of 10 mm compared to the inner diameter of the utilised CF-40 flange of 37 mm leads to a decreased GF (according to the theory of conductance in chapter 2.5) whilst still allowing the laser to pass through. Thereby, the pressure is expected to be successively decreases from the main target chamber towards the outer pre-chambers. It is thus ensured that high vacuum conditions are given at the connection parts with the residual parts of the experiment, the XFEL and the spectrometer.

Pfeiffer Vacuum full range gauges (PBR-260) are connected to all five chambers of the structure. These measure the pressure in the respective vacuum chamber with a relative error of approximately 15 %. This leads to the errorbars in all following plots depicting pressure measurement results. In general, these gauges can quantify pressures between 1000 mbar and 10^{-9} mbar. Together, they are connected to a *Pfeiffer Vacuum* maxi-gauge (TPG-256-A), a control unit that displays the corresponding pressure values. In this way, the vacuum conditions at different points of the system can be measured at any time. Thus it can be ensured that the required values are achieved and maintained at the beamtime. Furthermore, the gauges enable GF measurements to be carried out, as was done in this thesis' project in order to compared the results to the theoretically estimated pressure and conductance values.

During the execution of the experiment in Hamburg, employing the *EuXFEL* and the dispersive grating spectrometer, the main chamber is planned to be placed on a high-precision elevating platform while the rest of the system is positioned in a stationary manner. The flexible bellows between the chambers enable the alignment of the laser. A pair of electrodes and a photosensitive screen are mounted inside the chamber. In combination, these make it possible to direct the laser beam through the holes of the target cell by a controlled repositioning of the platform. The installation of these elements has not yet taken place; a more detailed description is therefore not given this thesis.

3.1.1 Turbo pumps and pre-vacuum

The five components used to achieve the high vacuum are HiPace[®] turbo pumps; rotor blades (similar to a turbine) suck the residual gas out of the chambers. The four smaller pumps (HP-80 and HP-300) are kept at operating temperature through 24 V air-cooling units. The large HP-2300 pump, on the other hand, is water-cooled. All pumps are connected to *Pfeiffer Vacuum* DCU control displays, which are used for commissioning, regulation and control. The pumping capacity values S_p (see chapter 2.5), listed in the following table, are provided by the manufacturer as technical data for the pumps. For neon gas, no information can be obtained. Since numerous factors influence the gas-specific pumping speeds, an exact calculation is difficult. As confirmed during direct communication with *Pfeiffer Vacuum*, the pumping capacity value for neon can be considered equal to that of nitrogen in the subsequent calculations of pressure values. However, the manufacturer's test conditions cannot be expected for the recording of the pressure measurement series. [22]

	HP-80 [L/s]	HP-300 [L/s]	HP-2300[L/s]
Nitrogen	67	260	1900
Neon	67	260	1900
Argon	66	255	1800

Table 3.1: Pumping capacities S_p of HiPace[®] turbo pumps in [L/s] used in later calculation for different gases; S_p for neon (Ne) is assumed to be approximately equal to S_p for nitrogen (N₂); taken from [22]

Finally, the pre-vacuum system as illustrated in figures 3.3 and 5.1 is to be described (for the latter, a photograph of the setup, see appendix A.2). All connections of this system are sealed by means of 'Kleinflansch' (KF) rubber gasket rings. For the turbo pumps to operate as intended, it is necessary to evacuate their drains beforehand. A water-cooled A-100-L roots pump, also supplied by *Pfeiffer Vacuum*, serves this purpose. All gas in the system, including the extracted neon target gas, is discharged via an exhaust outlet. The pump is connected to the turbo pumps' outlets using a connecting piece "flute", each joint being equipped with a rotary valve for successive pumping. A TPR pressure gauge is attached to this which, compared to the gauges shown in figure 3.1, has a smaller measuring range with greater accuracy. This covers the expected magnitude for the pre-vacuum pressure of 10^{-2} mbar before and 10^{-1} mbar during operation. Additionally, a connector for helium leak tests is provided via another rotary valve.

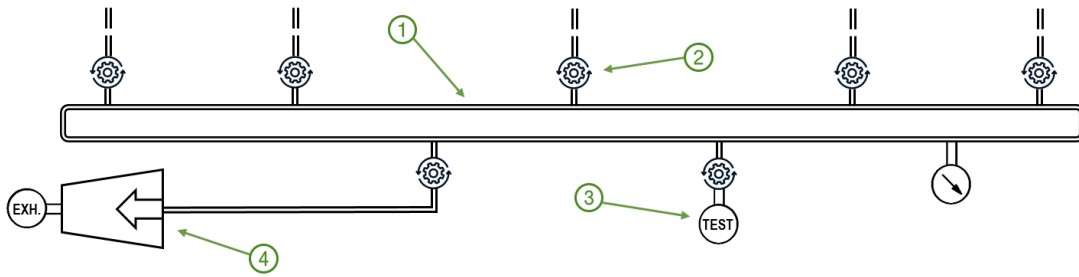


Figure 3.3: Structural overview of pre-vacuum system, connected to pumps of all five chambers shown in figure 3.1 above; components:

- ① Connecting piece "flute" for adaptation and joint gas extraction
- ② Variably adjustable rotary valve for step-by-step evacuation
- ③ Gas leak detection connection for inspection of entire system
- ④ *Pfeiffer Vacuum* A-100-L roots pump with exhaust outlet for pre-evacuation

3.2 (Neon-) gas supply and target cell

Figures 3.4 and 5.2 depict the structure of the gas supply system (for the latter, another photograph, see appendix A.2). First, a gas source is connected. In the context of later neon pressure measurements, this is a neon gas bottle. Alternatively, it can be linked to an external line. The goal is to apply pressures from 0 bar up to 10 bar in order to make propagation effects of the XFEL pulses noticeable in their absorption spectrum (see [3]). The connection lines of the illustrated system are produced by *Swagelok* and have an inner diameter of 4 mm. After the source, the gas flows into the *Festo* proportional pressure control valve, which is used for precise pressure control and is operated utilising a computer. This control valve is described and characterised in detail in chapter 3.3. The output of the *Festo* regulator is connected to the target cell in the main chamber via a *Swagelok* line, closable by means of the pneumatic valve V1. This is electronically controlled and works in the same way as the *VAT* devices shown in figure 3.1. It provides a means of shutting off the gas supply and can facilitate the evacuation of the chamber system. The second valve (V2) can be opened to free the supply line from residual gas after usage. Furthermore, it helps to pump down the target cell and main chamber, allowing for quick switches between measurements for different types of target gas. Finally, this connection, as well as the venting outlet of the *Festo* unit, is connected to a dry scroll pump (IDP-15) manufactured by *Agilent*.

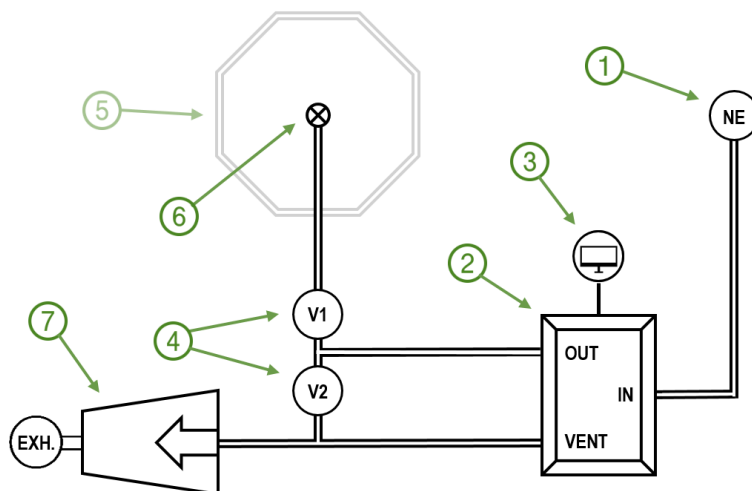


Figure 3.4: Structural overview of neon supply system for adjusting gas pressure inside target cell; components:

- ① Gas bottle as neon source, later: external supply line
- ② *Festo* proportional pressure control valve
- ③ Computer control with analogue-to-digital converter for regulation
- ④ *Swagelok* pneumatic valves for controlled operation
- ⑤ Main chamber with target cell (see figure 3.1)
- ⑥ Specially manufactured, interchangeable target cell for neon supply
- ⑦ *Agilent* IDP-15 dry scroll vacuum pump connected to exhaust outlet for evacuation and venting

Following the *Festo* control unit and valve V1, the gas enters the main chamber of the setup via a specially welded *Swagelok* line within a CF-40 flange. On the inside, a thin bellow further leads to a pedestal on top of which the target cell is mounted precisely in the centre of the chamber. The connection between the cell and the base is sealed by means of three screws and a rubber gasket ring. Figure 3.5 illustrates this gas supply.

To be able to have different interaction lengths and target pressures, the target cells are quickly replaceable with similar copies. Thereby, cells with hole diameters of 100 μm and 200 μm are available for three different cell lengths. The outer lengths measure 4 mm, 6 mm and 10 mm, excluding the thickness of the cell walls (1 mm each), inner cell lengths of 2 mm, 4 mm and 8 mm remain. The interior of the cells is hollow, which is where the gas accumulates at the desired high pressure. The holes allow the laser to propagate through the target gas within the cell. The inside is of oval shape and milled with high precision to ensure a reliably

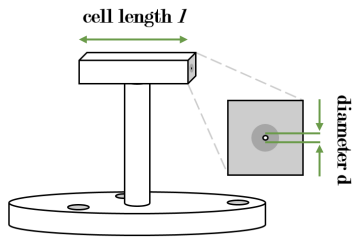


Figure 3.5: Structural illustration of target cell (height of 4 mm) with cell length l and hole diameter d , mounted on 13 mm high pedestal (without cell), including 3 mm thick base (diameter of 25 mm) with mounting holes

determinable propagation length for the laser. In order to drill the holes with extremely fine bits, a cut-out was made around the hole. A small portion of the accumulated target gas inevitably flows out of these openings and distributes itself in the chamber system. It is thus crucial to continuously pump out the residual gas to ensure low laser attenuation outside the cell. Finally, it should be noted that plans to construct a cell with smaller diameter holes are underway. More on this later.

3.3 Characterisation of Festo pressure control valve

The *Festo* proportional pressure control valve has a gas input and output connection as well as a venting outlet. An 8-pin electrical connecting plug is used for the control. A specifically constructed connector supplies the unit with the necessary operating voltage of 24 V DC via one pin and feeds a voltage signal between 0 V and 10 V DC (at a maximum of 20 mA) via another. In direct correspondence with this voltage value, the output pressure is set between 0 bar and 10 bar. The *Festo*'s display shows the set input value while the actual value is transmitted by another pin. Connected to this is an analogue-to-digital converter which translates a digital control signal sent from the computer into a discrete analogue voltage. With the help of the software *LabVIEW*, the pressure control valve is operated and the actual value of the output is read out. As specified by the manufacturer, the accuracy is 2%, i.e. a maximum of 0.2 bar for the highest possible pressure. Additionally, it should be noted here that the unit is not fully leak-proof. If an attempt is made to evacuate the chamber system with valve V1 open and the scroll pump switched off, it is found to work considerably worse. During the experiment, the pump should therefore be switched on, even at times when no pressure is applied.

For an initial characterisation measurement, nitrogen gas was applied to the control valve. Nitrogen was chosen because for this the exact values of the pumping capacity S_p are known, the gas is cheaper in use and operation via the in-house supply line is more practicable. The pressure of said supply line was set to 11 bar to ensure the maximum value of 10 bar to be potentially reached. Then a pressure

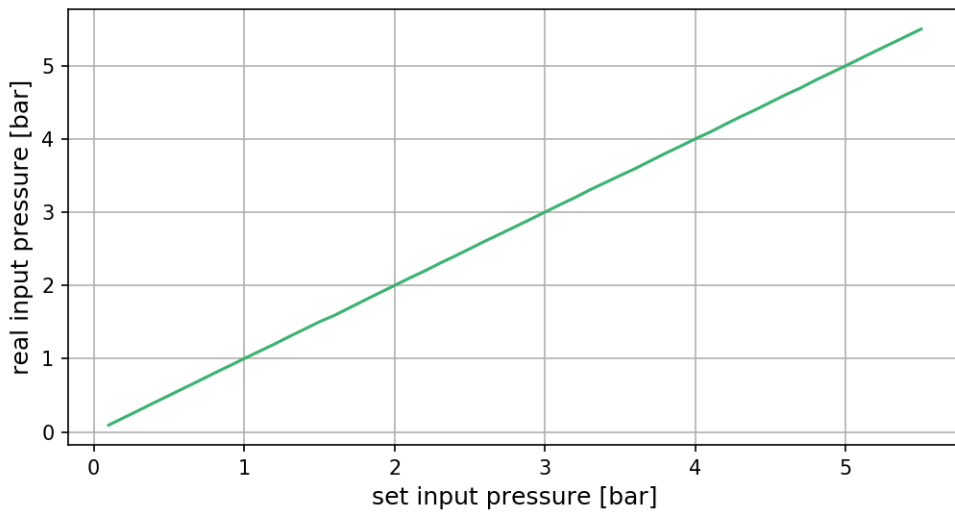


Figure 3.6: Characterisation of *Festo* pressure control valve with steps of 0.1 bar and constant error of 0.005 bar

range of 0.1 bar to 5.5 bar bar was driven in steps of 0.1 bar and the actual output pressure value was recorded in agreement with each set input value. Since a cell with $d = 100 \mu\text{m}$ was used for this measurement, higher pressures could not be achieved without causing dangerous overheating and automatic shutdown of the turbo pumps. The accuracy of the output voltage signal was determined by sampling with 1 kHz frequency over 5 seconds. These 5000 shots gave a constant error value of 0.005 bar, almost independent of the input pressure. On average, this was also obtained using just 500 shots at the same frequency when working with neon gas (although the error changed more frequently on the second significant digit). The pressure output can thus be considered independent of the gas type used and stable after a short period of regulation and adjustment. In relative terms, this error value is therefore below 1% beyond 0.5 bar. As a consequence, the error of the input pressure is neglected in the following calculations of the chapter as well as in all plots. Furthermore, it should be noted that the control unit requires a comparatively long stabilisation time of around 30 s for the minimal pressure value (0.1 bar), because the valve thereby is at its minimal opening position and is given less space for operation. Especially for higher pressure values, the inaccuracy is negligible; as a result, the linear relationship between the set and the real input pressure with the expected slope of 1 is observed, as can be seen in figure 3.6.

To further assess the functionality and suitability of the pressure control valve in

use, two long-term measurements were carried out. First, neon gas was supplied at a constant pressure of 2.5 bar for 75 min. No change of the recorded pressure values for the main and inner pre-chambers was detected, which remained at $2.1 \cdot 10^{-3}$ mbar and $1.1 \cdot 10^{-5}$ mbar, respectively. For the outer pre-chamber, an increase of 2.3 % from $4.4 \cdot 10^{-7}$ mbar to $4.5 \cdot 10^{-7}$ mbar was displayed. Since this change lies well within the measurement accuracy of the *Pfeiffer Vacuum* pressure gauges (15 %), the pressure values can be regarded as sufficiently constant. At the given input pressure, the capacity of the turbo pumps as well as the pressure control thus are at a steady level with neither a drop or shut down of the turbo pumping speed nor an increase of the chamber pressure.

Secondly, nitrogen gas was used and a pressure of 2 bar was applied. This setting was maintained for 48 h while the system operated in the intended manner. During and after this comparatively long period, the real input pressure, again, remained at the constant value to which the *Festo* unit was set. The same is true for the pressure conditions within all chambers, the main chamber pressure yielded $5.8 \cdot 10^{-3}$ mbar shortly after the beginning and at the end of the measurement. The *Festo* device can thus be employed for an extended duration in the upcoming experiment and provides reliable pressure values. This test also implies a continuous performance of the pumps when the input pressure is set to appropriate values.

A final characteristic to be investigated is the reproducibility of a measurement at a specific input pressure. The various measurements presented in the course of this chapter of the thesis were started under different pressure conditions within the chambers. The background pressure within the main chamber at 0 bar input pressure ranged between $1.7 \cdot 10^{-6}$ mbar and $2.6 \cdot 10^{-7}$ mbar, also depending on the time given for the turbos to pump down the chambers. In the pre-chambers, the pressure was always lower by about an order of magnitude and was at a minimum of $5.4 \cdot 10^{-9}$ mbar. With different starting values, however, approximately the same pressures were established in the chambers of the system using equal input pressures for given gases and cells. Even during operation with higher input values, the background pressure continuously decreases. In other words, the vacuum in the chambers, which is present without gas input, is increasingly improved over time. Eventually, a terminal state would be reached when the system is cleared of all residual contaminants and an equilibrium is established between the amount of air pumped out and the inflow through minor leaks. The respective starting pressure in a chamber is consequently to be understood only as an offset to the measured pressures during gas supply, which is increased by several orders of magnitude and can thus be neglected for the following calculations.

To validate the qualitative observation of reproducibility, the same pressure (3 bar) was sequentially applied ten times at short intervals with neon gas and using a cell with a $d = 100 \mu\text{m}$ hole. Without exception, all measurements yielded the same pressure values for main ($2.4 \cdot 10^{-3}$ mbar) and pre-chambers ($1.2 \cdot 10^{-5}$ mbar and $5.2 \cdot 10^{-7}$ mbar). Additionally, a test with different pressure values between 0.5 bar and 3 bar (steps of 0.5 bar) was carried out after a complete restart of the system. The pressure values in the main chamber deviated by 0% from the previous data collection for these six measurements. In the inner pre-chambers, the values were found to be 2.8% lower than the reference values when the measurements were repeated, and 5.9% lower in the outer pre-chambers. On the one hand, this may again be due to the measurement inaccuracy of 15%; on the other hand, it must be noted that the initial conditions (at 0 bar input pressure) differed. After restarting the system, the initial pressure values in the chambers were around half an order of magnitude below those of the first measurement due to a longer waiting time beforehand. This difference, the aforementioned offset, was slightly noticeable in the pre-chambers. The lower pressures during gas operation lead to a relatively higher, thus at some point non-neglectable offset pressure. It is therefore advisable to ensure at least 3 h of stabilisation time before measurement in the experiment. However, even without this, the differences in the pressure conditions are negligible; thus, a satisfactory reproducibility is given.

3.4 Differential pressure and gas flow measurements

3.4.1 Theory for experimental system

In this section, the previous remarks on the experimental setup and the theoretical principles of GF from chapter 2.5 are brought together. Here, the results of different calculations are presented, i.e. the theoretical expectations for the subsequent measurement of pressure conditions within the chambers of the experiment. The results of these measurements are thereafter compared to the theory to identify the most suitable model for the conductances between the cell and the main chamber as well as between the different chambers. For this purpose, Nitrogen (N_2) is referred to exclusively in this chapter as the gas is widely accessible. Additionally, all its necessary parameter values are well-known in contrast to the otherwise preferable neon gas (see chapter 3.6).

The supplied gas is at a controlled pressure P_0 in the range of a few bar. For now, it is assumed that this value is also given inside the target cell. This is corrected in detail in chapter 3.4.3. Subsequently, the gas flows out through the two laser propagation holes with a combined net speed S_1 and pressurises the previously

evacuated main chamber. From there, it is partly pumped out by the HP-2300 turbo pump or alternatively enters the pre-chambers of the system. In the following calculations for the conductance, the latter process is neglected. It shows that the value for the pumping stage connecting the chambers is more than three orders of magnitude below the that of the turbo pump's capacity. An equilibrium pressure P_1 can be determined for the interior of the main chamber, which is established after a few seconds of stabilisation following the inlet of the N_2 gas. Due to the suction of the HP-300 turbo pumps, the residual gas responsible for P_1 is in parts sucked into the two inner pre-chambers through the aforementioned pumping stages with a net speed S_2 on both sides. Here, too, a stabilised pressure P_2 is established at constant supply and pumping capacity. This process is repeated on both sides thanks to another set of pumping stages and the two HP-80 turbo pumps. Consequently, a further reduced pressure P_3 is to be expected as a result of the net speed S_3 in the outer pre-chambers.

Using the parameters for nitrogen given in table 2.1, four different values are initially calculated for the target cell conductance C_1 towards the main chamber, based on the different theories of GF. Due to the properties of the cell holes, none of the known conductance models can be assigned a priori. The thickness of the cell wall is only five times greater than the diameter of the opening and pressures of different orders of magnitude occur. Accordingly, it is necessary to determine the appropriate theory considering both tube and aperture as well as viscous and molecular flow. The value C of a single hole is multiplied by two, since the target cell and main chamber with the two holes as connections form a parallel system whose combined conductance can be calculated using equation 2.27. In figure 3.7 b) the purple curve represents the case of a tube opening in the viscous flow regime. This is based on equation 2.29, where D denotes the hole diameter ($D = 100 \mu\text{m}$) and L the 'length', i.e. the wall thickness ($L = 500 \mu\text{m}$). The mean pressure in this formula is approximated as half of the applied Festo input pressure P_0 , thus C is pressure-dependent in this model. This is not the case for the remaining models. The blue curve in a) is based on the assumption of the holes being tubes in the molecular flow regime (see equation 2.31). Here, accordingly, the average velocity of the nitrogen molecules is taken into account. The green and pink curves in a) assume the aperture case and are obtained from equations 2.30 and 2.32 for viscous and molecular flow, respectively. Furthermore, the master equation 2.25 leads to expression 3.1 that describes the net speed S_1 for the target cell holes used in the experiment. Moreover, equation 3.2 is derived for the main chamber pressure P_1 incorporating the turbo pump's capacity S_{P1} . It follows:

$$S_1 = \left[\frac{1}{S_{P1}} + \frac{1}{C_1} \right]^{-1}, \quad (3.1)$$

$$P_1 = \frac{S_1 \cdot P_0}{S_{P1}}. \quad (3.2)$$

For a better understanding of equation 3.1, it is important to mention that the values of the pumping capacities exceed those of the conductances by several orders of magnitude in most of the following cases. The net speed is therefore approximately equal to the conductance. To put it differently, the smaller the hole (or the longer the tube), the less influence the capacity of a pump behind this hole (or tube) has on the GF through it. The efficiency of pumping is reduced.

Again using equation 2.31, this time for the conductance C_2 of the distinctly tube-like pumping stages with $D = 1$ cm and $L = 10$ cm and under the assumption of molecular flow, the process is repeated for the two pre-chambers on both sides. In the following expressions, S_2 and S_3 are used for the inner and outer pre-chamber respectively, which are calculated in analogy to equation 3.1. The conductance C_3 is thereby equal to C_2 , as pumping stages are identical in construction. Additionally, the turbo pumps' capacities S_{P2} and S_{P3} from table 3.1 are included. With the conductances the pressures P_2 and P_3 can be calculated in the same way as in equation 3.2. Again applies:

$$P_2 = \frac{S_2 \cdot P_1}{S_{P2}}, \quad (3.3)$$

$$P_3 = \frac{S_3 \cdot P_2}{S_{P3}}. \quad (3.4)$$

Based on these equations, Figure 13 presents the theoretical pressure values and thus serves as a basis for the subsequent comparison with measurement results. At this point, it is important to emphasise that the differently coloured curves in the plots for P_2 and P_3 are the consequence of the four different theories for the target cell hole conductance. The pumping stages, i.e. the transitions between the chambers, are exclusively modeled as tubes in the molecular flow regime.

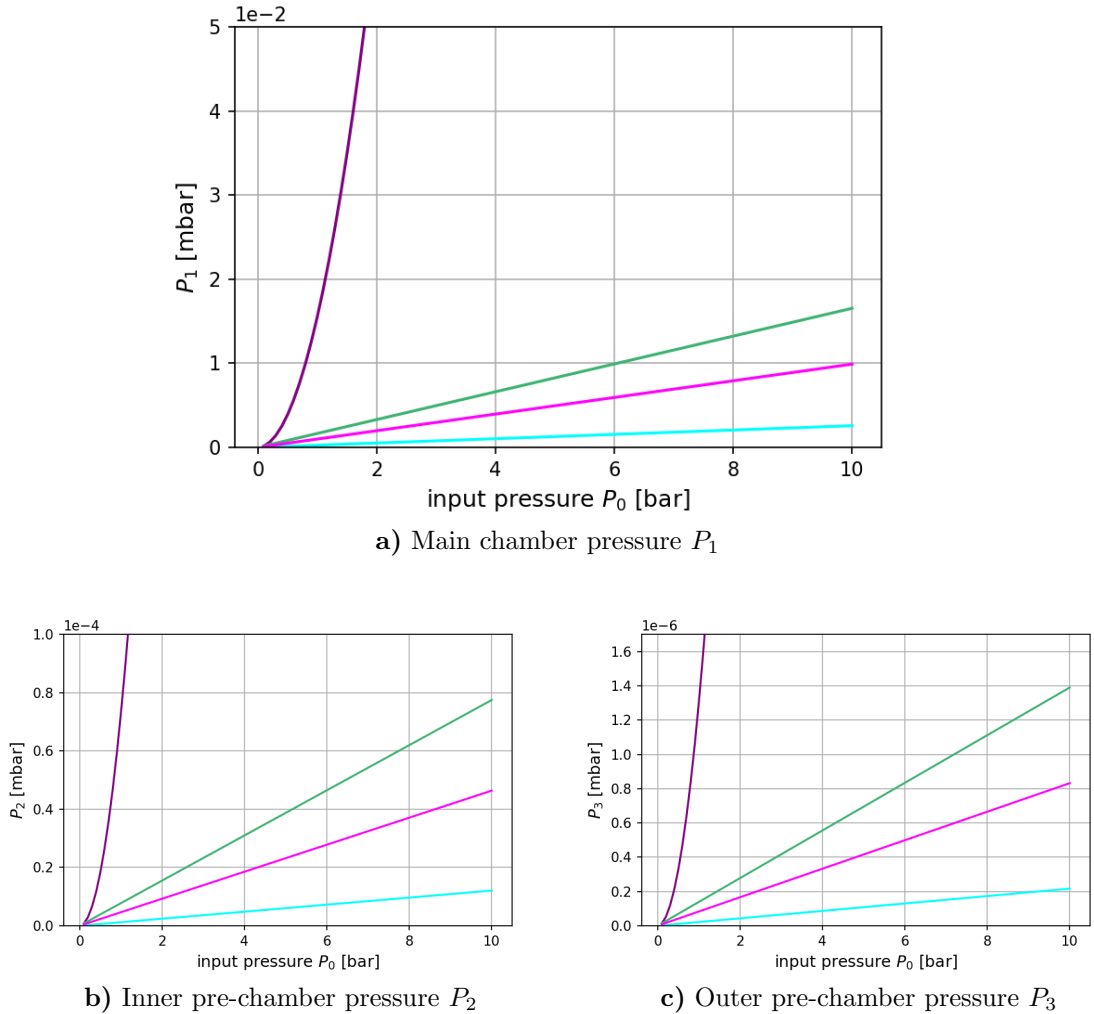


Figure 3.7: Theory for pressure values in **a)** main chamber, **b)** inner and **c)** outer pre-chambers for four different target cell hole conductance models (purple: tube and viscous flow, blue: tube and molecular flow, green: aperture and viscous flow, pink: aperture and molecular flow); for nitrogen gas and target cell with $d = 100 \mu\text{m}$

3.4.2 Pressure results for main chamber

The first series of measurements was carried out with a cell of 6 mm length with a hole diameter of $100 \mu\text{m}$. The initially chosen goal, an input pressure of 10 bar, is not achievable with this or any other currently available cell. However, chapters 3.5 and 3.7 suggest how this (rather arbitrarily chosen) goal can nevertheless be

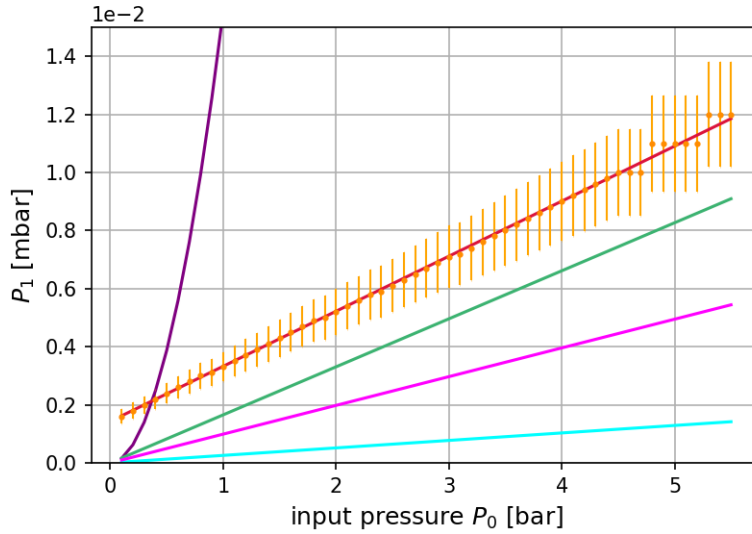


Figure 3.8: Measurement for pressure values P_1 in main chamber with linear fit (orange: measured values, red: linear fit) and theory for four different models of cell hole conductances (purple: tube and viscous flow, blue: tube and molecular flow, green: aperture and viscous flow, pink: aperture and molecular flow); for nitrogen gas and target cell with $d = 100 \mu\text{m}$

achieved in the upcoming experiment. Since the HP-2300 turbo pump of the main chamber starts reducing its rotational frequency at around 10^{-2} mbar to avoid damage because of too high gas load, the series of measurements end at the corresponding values, depending on the cell and gas type. In the following results, the shutdown started at 5.1 bar input pressure with the measurement being continued briefly up to 5.5 bar. A drop in the rotational frequency from 525 Hz to around 500 Hz was noticed. The data shows a clear linear relationship between the pressure in the main chamber and the *Festo* input pressure; it is compared to the theoretical plots in figure 3.8. The curve for the conductance model of a tube in viscous flow is the only one to show a quadratic shape and can therefore be ruled out as a suitable model most easily.

The measurement curve appears to be described best by the aperture model in the viscous flow regime, since the slopes of these two curves are the most similar. Compared to the modelling of the cell openings as tubes, the aperture description in the molecular flow regime does not deviate as strongly from the course of the measurement curve. Consequently, an aperture model is preferable. Since

the slope value allows direct conclusions to be drawn about the real conductance, a linear fit is applied to the measurement curve. This leads to a slope of $x_1 = (1.90 \pm 0.07) \cdot 10^{-3} \text{ mbar/bar}$. Combining equations 3.1 and 3.2 results in a corresponding linear expression $P_1(P_0) = x_1 \cdot P_0$ with the slope:

$$x_1 = \left[S_{P1} \cdot \left(\frac{1}{S_{P1}} + \frac{1}{C_1} \right) \right]^{-1}. \quad (3.5)$$

By rearranging equation 3.5, the value C_1 for the experimental combined conductance of the two cell holes is determined to be $C_{cell} = (3.6 \pm 0.1) \cdot 10^{-3} \text{ L/s}$. The error is calculated using that of the slope fit. In the following table, this experimental result is compared to the conductance values of the three linear models:

	Conductance value [L/s]	Deviation in %
Measurement	$(3.6 \pm 0.1) \cdot 10^{-3}$	
Tube and molecular flow	$4.90 \cdot 10^{-4}$	86.4
Aperture and viscous flow	$3,14 \cdot 10^{-3}$	12.7
Aperture and molecular flow	$1.88 \cdot 10^{-3}$	47.8

Table 3.2: Comparison of measured and theoretically calculated conductances of target cell holes with deviations of linear model values from experimental result

This confirms the assumption that the aperture model in the viscous flow regime describes the holes of the target cell most accurately. Although the quantitative deviation in the $5\text{-}\sigma$ range is of significant nature, it is important to emphasise the fact that both the order of magnitude and the linear shape of the theoretically calculated pressure curve for the main chamber are thereby confirmed qualitatively by the experiment. Since the described properties of the target cell holes cannot be unambiguously assigned to either an aperture or a hole, and since the pressure conditions in the cell and main chamber vary considerably, this qualitative correspondence can be considered a success. The quantitative deviation is also sufficiently small to make reliable predictions based on the theory presented.

3.4.3 Conductance of gas supply system

The previous remarks are based on the assumption that the pressure inside the target cell is the same as that which is applied via the *Festo* pressure control

valve (P_0). However, this is not entirely realistic, as only a certain proportion of the input pressure is present in the cell in accordance with the conductance of the gas supply system C_0 between the *Festo* control valve and the target cell. The aim of this chapter is to determine the value of said conductance. Since the model of the tube in the viscous flow regime is presumably appropriate for the long supply line (181 cm) and the high pressures (1 bar regime), a linear dependence of the conductance on the input pressure is to be expected following equation 2.29.

First, analogous to equations 3.1 and 3.2, an expression for the real pressure P_c within the cell is derived as a function of the input P_0 . Here, the target cell hole conductance C_{cell} takes the place of the 'pumping capacity', i.e. describes the GF out of the cell in approximation. In follows:

$$P_c(P_0) = \left(\frac{1}{C_{cell}} + \frac{1}{C_0} \right)^{-1} \cdot \frac{1}{C_{cell}} \cdot P_0. \quad (3.6)$$

The conductance C_0 of the gas supply line is subsequently computed using the following expression as well as the fitted measurement data for P_1 (see figure 3.8):

$$C_0 = -C_{cell} \cdot \left[\frac{P_0}{P_1} \cdot \frac{1}{1 + \frac{S_{P1}}{C_{cell}}} - 1 \right]^{-1}. \quad (3.7)$$

Figure 3.9 illustrates the course of the conductance C_0 , which is in fact linear. The value increases with rising input pressures and, according to equation 3.6, results in a cell pressure below the input value. The actual course of P_c is displayed in blue in figure 3.10, the grey dashed line represents the hereby rectified assumption of $P_c = P_0$ within the target cell. Since C_0 already exceeds C_{cell} at $P_0 = 0.1$ bar and increases continuously, its influence in the sum of the inverse values in equation 3.6 diminishes with growing input pressures. Consequently, the slope of the blue curve quickly converges to the value 1, i.e. to that of the grey line. The growing linearity is noticeable for input values above 2 bar in figure 3.10. This results in a negative pressure offset 'accumulated' in the non-linear section of low input values. In the same figure, the dotted red curve with an additional y-scale on the right side represents the ratio of the two pressure values P_c and P_0 , which seems to converge to 1. Thus, the higher the input pressure, the closer the real pressure within the cell matches its value. In fact, one can show that P_c/P_0 converges to 1 due to the linear dependency of C_0 on P_0 , seen in equation 3.6:

$$\lim_{P_0 \rightarrow \infty} \left[\frac{P_c}{P_0} \right] = \lim_{P_0 \rightarrow \infty} \left[\frac{1}{1 + \frac{C_{cell}}{C_0(P_0)}} \right] = 1. \quad (3.8)$$

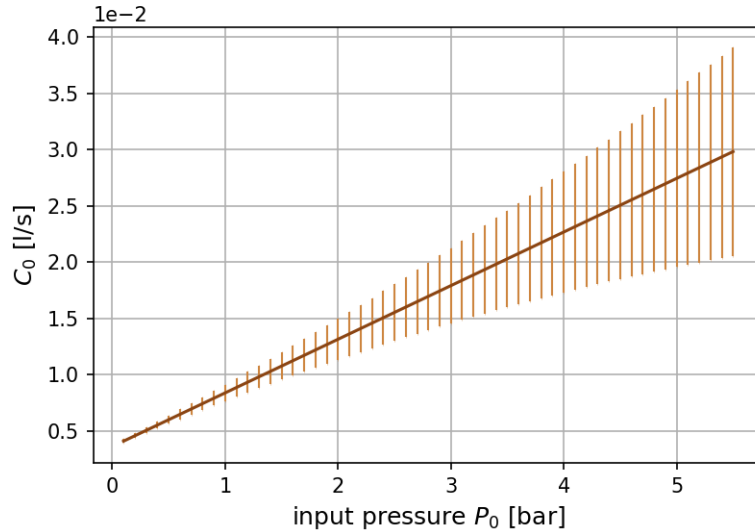


Figure 3.9: Conductance C_0 of gas supply system derived from pressure values P_1 in main chamber; for nitrogen gas and target cell with $d = 100 \mu\text{m}$

To compute the C_0 conductance graph in figure 3.9, the results of the fit for P_1 in figure 3.8 were used. The corresponding slope of $C_0(P_0)$ can now be determined as well and is found to be $m_{supply} = (4.8 \pm 0.2) \cdot 10^{-3} \text{ L/s} \cdot \text{bar}$, which can be compared to a rough estimation calculation based on equation 2.29. This formula suggests that the value of this slope corresponds to $24450 \cdot D^4/2 \cdot \eta \cdot L$. By using the additional factor 2, the mean pressure $P_0/2$ is taken into account. To compare this with the result of a coarse calculation for the supply line conductance's slope m_{supply}^{approx} , the line is subdivided into two sections. From the outlet of the *Festo* pressure control valve to just before the target cell inside the main chamber extends a 165 cm *Swagelok* line with an inner diameter of 0.4 cm. Its end is connected to the cell via several adapters with another 16 cm line of 0.2 cm inner diameter. Since this is merely an estimation for the magnitude of conductance, the influences of the incorporated adapter pieces as well as that of the bellow's corrugated structure are neglected. Moreover, for this simplified approach to describe the supply line, the relative errors of the measured lengths is roughly estimated at 10%. The value m_{supply}^{approx} is calculated using equations 2.28 and 2.29 for a series of two single conductances as follows:

$$m_{supply}^{approx} = \frac{24450}{2 \cdot 166 \mu\text{P}} \cdot \frac{(0.4 \text{ cm})^4 \cdot (0.2 \text{ cm})^4}{(0.4 \text{ cm})^4 \cdot 16 \text{ cm} + (0.2 \text{ cm})^4 \cdot 165 \text{ cm}}. \quad (3.9)$$

This results in $m_{supply}^{approx} = (4.5 \pm 0.6) \cdot 10^{-3} \text{ L/s} \cdot \text{bar}$. This value is very close to

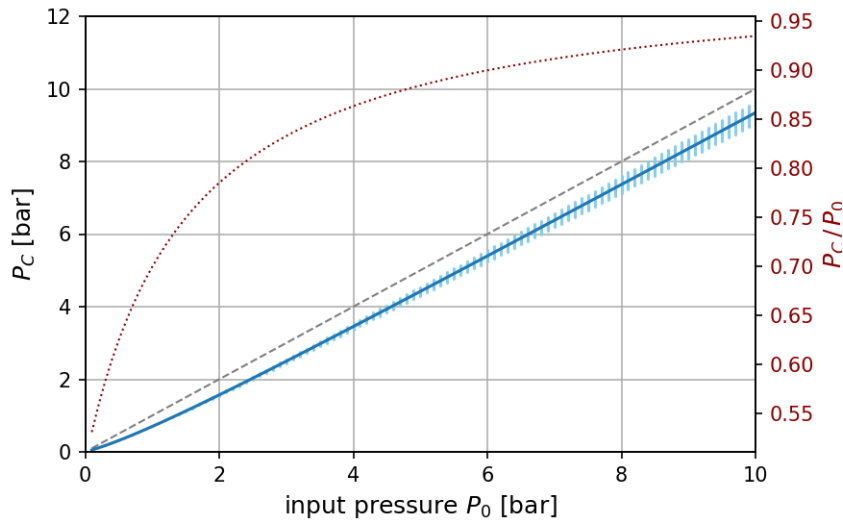


Figure 3.10: Resulting pressure values P_C in target cell (blue) compared to input pressure P_0 (grey); ratio of P_C and P_0 (red) with $P_C/P_0 \rightarrow 1$; for nitrogen gas and target cell with $d = 100 \mu\text{m}$

m_{supply} in figure 3.9 ($1-\sigma$ range) and thus confirms the procedure for computation of the conductance C_0 in a rough approximation. For further calculations and the upcoming experiment, this provides a method to determine the real pressure inside a target cell depending on the utilised gas and specific cell type as well as the input pressure value. More on this in chapter 3.7.

3.4.4 Pressure results for inner pre-chamber

As the maxi-gauge unit features only three display connection ports suitable for high vacuum, just one side of the pre-chamber setup was monitored during the pressure measurements. By temporally switching the connections during measurements, it was confirmed that the two sides of the vacuum apparatus exhibit the same pressure values for both inner and outer pre-chambers. This agrees well with the theory predictions. Thus, the measured values considered in the following are representative for both sides and it is reasonable to compare them to the theoretical calculations.

Figure 3.11 presents the measurement of the inner chamber pressures P_2 as function of the input pressure P_0 in comparison with the purely theory-based calculations, structured and coloured in the same manner as in figure 3.7. The applied model for the conductance C_2 of the preceding pumping stage is that of a tube in the

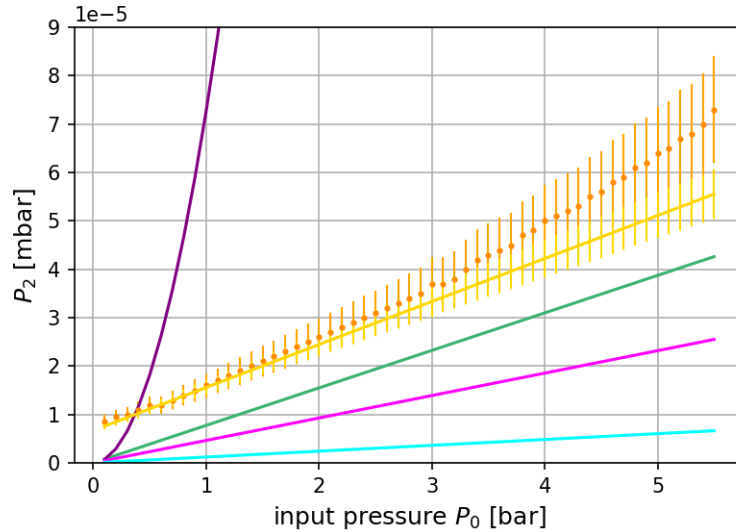


Figure 3.11: Measurement for pressure values P_2 in inner pre-chamber (orange: measured values) and theory for four different approaches to calculation of cell hole conductance (purple: tube and viscous flow, blue: tube and molecular flow, green: aperture and viscous flow, pink: aperture and molecular flow); semi-theoretical calculation of $P_2(P_1)$ using fitted measurement values for P_1 from figure 3.8 and theoretical pumping stage conductance C_2 (yellow); for nitrogen gas, target cell with $d = 100 \mu\text{m}$ and pumping stages with $D = 1 \text{ cm}$ and $L = 10 \text{ cm}$

molecular flow regime. It is essential to understand that, due to its calculation via P_1 , the pressure within the inner pre-chamber depends not only on C_2 but also on the aforementioned value C_{cell} for the target cell. Since the aperture model in viscous flow was found to be the most accurate description of the target cell's holes, the correspondence of the measurement results with the green curve is expected to be the strongest. For that reason, the other three graphs are omitted in the following plots. In addition, a semi-theoretical curve for P_2 is shown in yellow, which is derived from equation 3.3. It is based on the fitting results for the measurement of P_1 as illustrated in figure 3.8 as well as the above mentioned tube model in viscous flow for C_2 . Finally, the measurement data for P_2 is again plotted in orange.

Initially, a linear trend is apparent in the data. However, the curve drifts upwards for input pressure values of 3 bar and above. Here, a pressure of about 10^{-3} mbar is reached in the main chamber and, according to [20], the transition region from

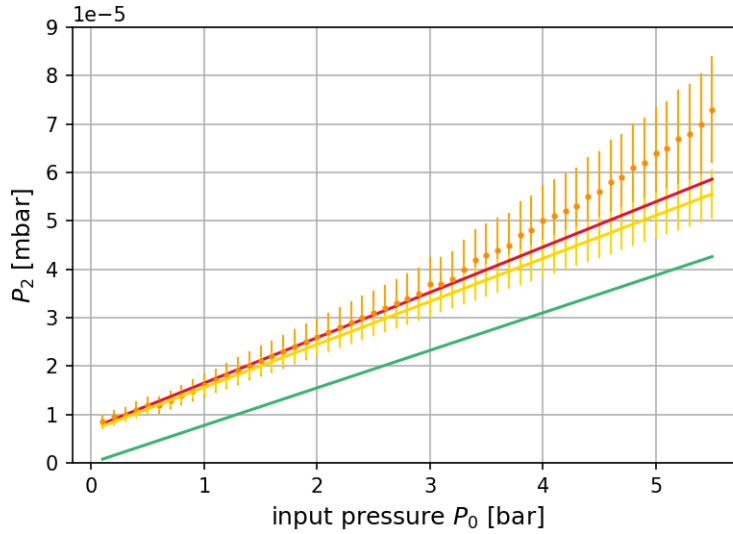


Figure 3.12: Measurement for pressure values P_2 in inner pre-chamber with linear fit (orange: measured values, red: linear fit) and theory based on (aperture, viscous flow) cell hole conductance as well as (tube, viscous flow) pumping stage conductance C_2 (green); semi-theoretical calculation of $P_2(P_1)$ using fitted measurement values for P_1 from figure 3.8 and theoretical pumping stage conductance C_2 (yellow)

molecular to viscous flow begins (Knudsen flow occurs). A precise description of this range is difficult and beyond the scope of this thesis; [20] provides a more detailed elaboration. Nevertheless, it is evident that this marks the transition from constant to pressure-dependent conductance values for the molecular and viscous flow regime, respectively. According to equation 2.29, the dependency of the pressure inside the pre-chamber on the input pressure thereby changes from linear to quadratic. This explains the increasing slope of the measured data curve starting at $P_0 = 3$ bar. A linear fit is again carried out to determine the slope and thus the conductance value of the pumping stage. This time, however, only the data up to 3 bar is taken into account. The fit result can be seen in figure 3.12.

As expected, the linear fit exhibits a similar slope to that of the (semi-theoretical) yellow curve and a slightly increased one compared to the green line (assuming a viscous flow aperture for the of cell holes, and a molecular flow tube for the pumping stage). The experimental conductance value C_{PS1} for the transition from the main chamber to the inner pre-chamber, i.e. for the pumping stage (corresponding theory value: $C_2 = 1.22 \text{ L/s}$), is calculated from the slope of the linear fit illustrated

in figure 3.12. This amounts to: $x_2 = (9.4 \pm 0.6) \cdot 10^{-6} \text{ mbar/bar}$.

Following the same principle as for the target cell conductance, the pressure in the inner pre-chamber can be expressed as $P_2(P_1) = P_2(P_1(P_0)) = x_2 \cdot P_0$. Here, too, the conductance can be determined from the slope x_2 in a similar way as in equation 3.5. The following expression applies:

$$C_{PS1} = \left[\frac{1}{x_2 \cdot S_{P1} \cdot S_{P2} \cdot \left(\frac{1}{S_{P1}} + \frac{1}{C_{cell}} \right)} - \frac{1}{S_{P2}} \right]^{-1}. \quad (3.10)$$

The calculation yields $C_{PS1} = (1.29 \pm 0.09) \text{ L/s}$. This can now be compared to the theoretical value C_2 , which lies well within the $1\text{-}\sigma$ range of C_{PS1} . Moreover, the theory deviates from the measured value by 5.2%. It can therefore be stated that with the mathematically predicted order of magnitude and the gradient of linear progression, the model approximation of the pumping stages as a tube in the molecular flow regime is proven to be applicable for $P_0 < 3 \text{ bar}$. In addition, the above mentioned non-linear component at higher input pressure values can be attributed to the incipient transition to the regime of viscous flow.

3.4.5 Pressure results for outer pre-chamber

In figure 3.13, the measurement results for the pressure P_3 in the outer pre-chamber are presented in orange along with the linear fit in red, again obtained by using input pressure values P_0 below 3 bar. The green curve depicts the results of calculating P_3 on an exclusively theoretical basis, following the assumption of the aperture model in the viscous flow regime for the target cell conductance. The yellow line indicates the semi-theoretically computed pressure values $P_3(P_2)$, given the linear fit results for the measurement data of P_2 (see figure 3.12). Again, the transitional pumping stage is modeled as a tube in the molecular flow regime for both (semi-)theoretical approaches with $C_3 = C_2$.

It is observed that the measurement results for the second pre-chamber deviate only marginally from their initial linear trend, even for high input pressure values. This remaining divergence can be understood from the measurement data curve in figure 3.12. Since the pressure values in the first pre-chamber do not show a strictly linear progression, this effect is also carried over in a weakened form into the values of the outer pre-chamber. A deviation from linearity due to the same phenomena as in the first pumping stage (transition to viscous flow regime) is unlikely for the second pumping stage with considerably lower pressure values. The non-linearity is thus expected to be a residual artifact of that observed for P_2 .

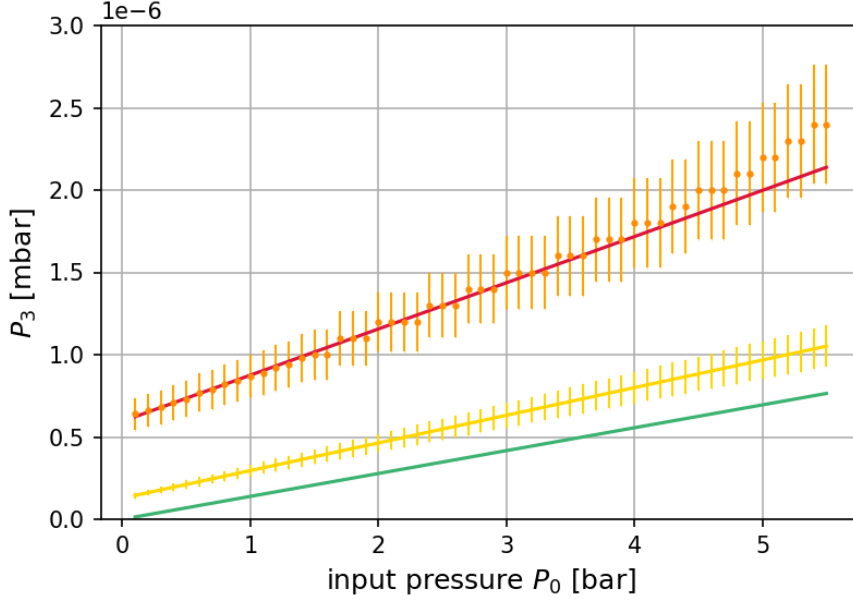


Figure 3.13: Measurement for pressure values P_3 in outer pre-chamber with linear fit (orange: measured values, red: linear fit) and theory based on (aperture, viscous flow) cell hole conductance as well as (tube, viscous flow) pumping stage conductances $C_3 = C_2$ (green); semi-theoretical calculation of $P_3(P_2)$ using fitted measurement values for P_2 from figure 3.12 and theoretical pumping stage conductance C_3 (yellow); for nitrogen gas, target cell with $d = 100 \mu\text{m}$ and pumping stages with $D = 1 \text{ cm}$ and $L = 10 \text{ cm}$

In this pre-chamber, the absolute discrepancy between the measurement values and those of the theoretical calculation is proportionally larger than in the first pre-chamber. Qualitatively, however, the order of magnitude and the general trend are in agreement here as well. Once again, it can be stated that the modelling of the pumping stage as a tube in the molecular flow regime is adequately precise. For a quantitative comparison, the pumping stage conductance C_{PS2} is once again calculated from the slope of the linear fit $x_3 = (2.8 \pm 0.3) \cdot 10^{-7} \text{ mbar}/\text{bar}$. In this case $P_3(P_2(P_1(P_0))) = x_3 \cdot P_0$ is used, whereby the expression for C_{PS2} as a function of x_3 is given as follows:

$$C_{PS2} = \left[\frac{\left(\frac{1}{S_{P2}} + \frac{1}{C_{PS1}}\right)^{-1}}{x_3 \cdot S_{P1} \cdot S_{P2} \cdot S_{P3} \cdot \left(\frac{1}{S_{P1}} + \frac{1}{C_{cell}}\right)} - \frac{1}{S_{P3}} \right]^{-1}. \quad (3.11)$$

The calculation yields $C_{PS2} = (2.1 \pm 0.2) \text{ L/s}$. The theoretically expected value $C_3 = C_2 = 1.22 \text{ L/s}$ (derived from equation 2.31) lies within the $5\text{-}\sigma$ range of this result and deviates from it by 41 %. This is a significant quantitative difference. However, the theoretical model still applies in qualitative terms. Due to the close correspondence with the conductance models for the previous chambers and since the discrepancy for P_3 amounts to less than half an order of magnitude, the theoretical description can be deemed applicable, especially for a qualitative estimation.

3.5 Pressure dependency on target cell hole diameter

For the experiment to succeed, it is of particular importance that the pressure inside the chamber system remains below the critical level at which the main turbo pump (HP-2300) starts to shut down. As discussed above, the conductance of the target cell holes can be described best by the aperture model, in which the conductance depends linearly on the hole's area and thereby quadratically on its radius. To verify this experimentally, a target cell with a hole diameter of $d = 200 \mu\text{m}$ was used to replace the preceding $100 \mu\text{m}$ cell. A series of measurements was again carried out using nitrogen gas (N_2). As anticipated, the test had to be aborted earlier than that with the $100 \mu\text{m}$ cell to protect the pumps from being damaged. The highest pressure applied was 1 bar. Figure 3.14 presents the measurement results for P_1 in the main chamber from chapter 3.4.2 in orange ($100 \mu\text{m}$ cell) and those using the subsequently installed $200 \mu\text{m}$ cell in blue. The green lines illustrate the theoretical computations for P_1 based on the aperture conductance model in the viscous flow regime (for C_1) and show good correspondence with the measured values for the increased cell opening, as well.

Moreover, figure 3.14 displays the result of a linear fit for each measurement series coloured in red. Since the main turbo pump's capacity S_{P1} is the same for both cases and $C_1^{100}, C_1^{200} \ll S_{P1}$ holds for both cell holes' conductances, the following relationship applies to the ratio of the linear fits' slopes x_{100} and x_{200} , derived from equation 3.2:

$$\frac{x_{100}}{x_{200}} = \frac{S_1^{100}}{S_1^{200}} = \frac{\frac{1}{S_{P1}} + \frac{1}{C_1^{200}}}{\frac{1}{S_{P1}} + \frac{1}{C_1^{100}}} \approx \frac{\frac{1}{C_1^{200}}}{\frac{1}{C_1^{100}}} = \frac{C_1^{100}}{C_1^{200}}. \quad (3.12)$$

Furthermore, due to the above-mentioned relationship between the aperture conductance and the radius, $\sqrt{x_{100}/x_{200}} = d_{100}/d_{200}$ applies. The resulting values for the respective slopes are $x_{100} = (1.90 \pm 0.07) \cdot 10^{-3} \text{ mbar/bar}$ and $x_{200} = (7.3 \pm 0.2) \cdot$

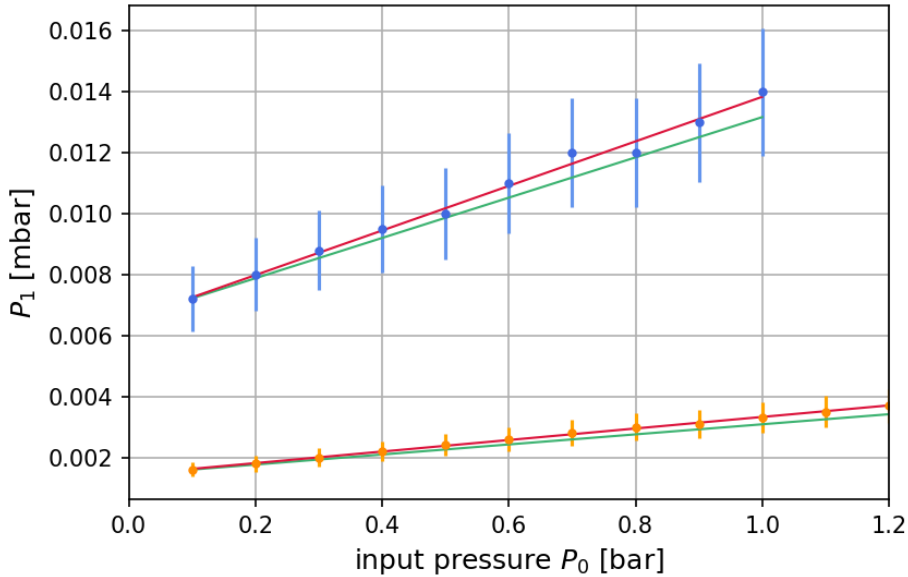


Figure 3.14: Measurement for pressure values P_1 in main chamber for 100 μm (orange) and 200 μm (blue) target cell holes, with linear fits (red) and theory for cell hole conductance (green: aperture and viscous flow); for nitrogen gas

$10^{-3} \text{ mbar}/\text{bar}$. The ratio of the hole diameters (and radii) thus yields:

$$\left(\frac{d_{100}}{d_{200}}\right)_1 = 1.97 \pm 0.04.$$

The expected value of $200 \mu\text{m}/100 \mu\text{m} = 2.0$ lies well within the $1\text{-}\sigma$ range of this result. Since the hole diameters have not been measured independently, the expected values of 100 μm and 200 μm are not verified. In order to examine the real ratio and thus the precision of the drilling, the two cells were positioned in front of a camera lens at the same distance and photographed at maximum optical magnification. Care was taken to ensure that the cell openings were in the optical focus, allowing for a comparison of the pixel numbers. Three digital measurements were carried out for each of the two sharpest images. One such example is given in figure 3.15; the results of all six measurements are to be found in the appendix A.3 (table 5.1). In the process, the diameter of a hole was put in relation to the width of the cell, because it is not guaranteed that both cells were perfectly aligned in the focal lane of the camera. Additionally, the cell length is expected to be manufactured more easily and precisely and was thus used as a reference length.

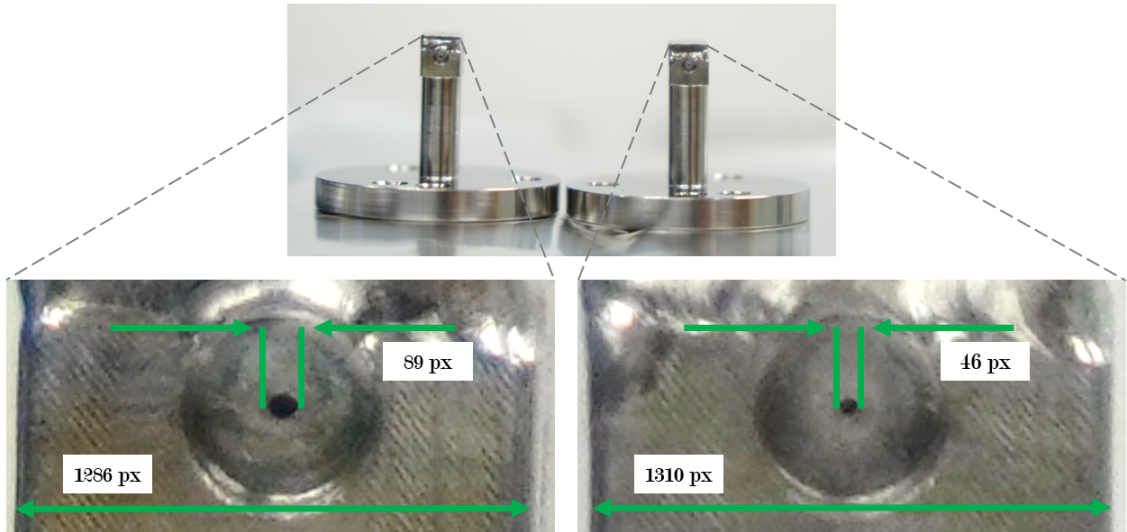


Figure 3.15: Top: example for image of both cells for digital hole measurement
 Bottom: illustration of measured lengths for cell width c and hole diameter h in pixels for 200 μm hole (left) and 100 μm hole (right), results see appendix A.3

Subsequently, the two resulting values for one photo were divided to calculate the ratio of the diameters. Since slight deformations of the holes and cells can be detected, these measurements were carried out at three different angles for each hole. The corresponding error was estimated to amount to 2 pixels for each individual measurement. The six resulting ratios yield the following (weighted) average with minimised total error:

$$\left(\frac{d_{100}}{d_{200}}\right)_2 = 1.98 \pm 0.04.$$

The close $1\text{-}\sigma$ correspondence of the two results suggests that both methods of calculation provide reliable values. The estimates for the errors seem adequately chosen as well. Of particular significance for the upcoming experiment is the conclusion that, in line with theoretical expectations, the pressure inside the main chamber depends quadratically on the radius of the target cell openings. In practical terms, a reduction of the hole size by a factor of 2 allows four times higher input pressures to be applied. While the maximum *Festo* input pressure value of 10 bar could never be reached in the measurements for this thesis project, it would be feasible with an appropriately modified cell with $d = 50\ \mu\text{m}$. This will be discussed further in chapter 3.7.

3.6 Pressure dependency on gas type

In order to deepen the understanding of the introduced theory of the GF as well as to gain a preliminary insight into potential future experiments with the presented setup, the following chapter examines the dependency of the pressure conditions on the type of gas in use. Therefore, the concluding measurements were carried out with the gases argon (Ar) and neon (Ne), especially the latter is of great interest for the upcoming experiment. The target cell with $d = 100 \mu\text{m}$ was also used for the two additional gases. Introductory, it should be mentioned that the *Pfeiffer Vacuum* full range pressure gauges (PBR-260) do not automatically display the real pressure for each gas type [23]. While this is the case for nitrogen, the displayed values for argon and neon have to be multiplied by 0.8 and 4.1, respectively. The results presented below correspond to the values that are already corrected that way.

In figure 3.16, the measurement results for all three chambers are compared to those of the gas-specific theory computations. The corresponding values from tables 2.1 and 3.1 were used to derive the latter. Apart from that, the calculation for neon and argon follows the same approach as described in chapter 3.4.1 for nitrogen. Below, a primarily qualitative description of the results is given; a quantitative analysis can be conducted analogous to that for nitrogen gas in the previous chapters.

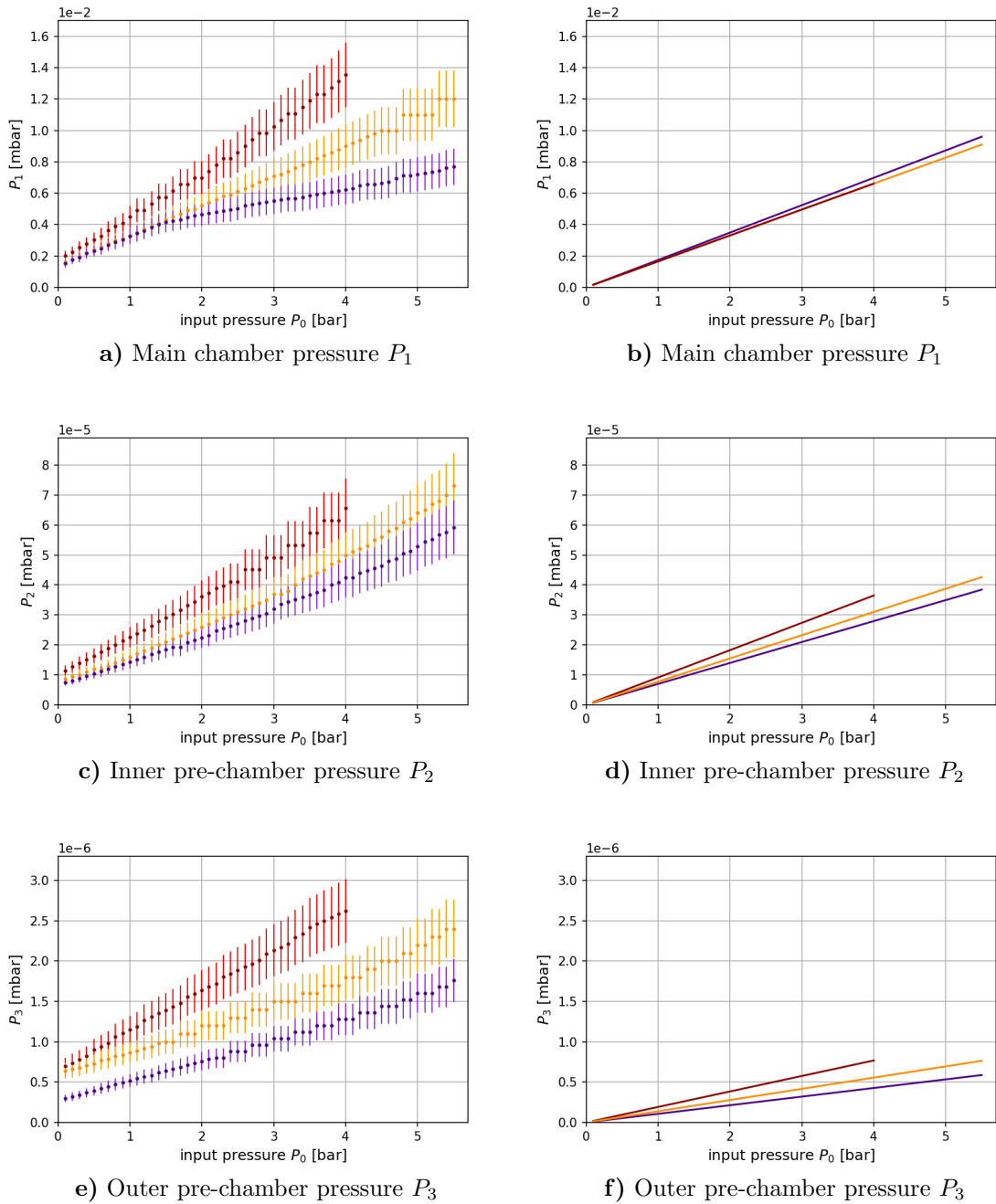


Figure 3.16: **a), c), e)** Measured pressure values in main chamber (P_1), inner (P_2) and outer (P_3) pre-chambers for different types of gas (red: neon, orange: nitrogen, purple: argon); for target cell with $d = 100\ \mu\text{m}$
b), d), f) Corresponding theory values for chamber pressures

To start off, the theoretical predictions for the pressure P_1 in the main chamber, see figure 3.16 b), are to be discussed. Differences in these values are solely the result of the varying pumping capacities. The aperture conductances in the viscous flow regime depend on the measures of the cell openings, not, however, on the gas type. Since the value of S_{P_1} for neon (red) is approximated by that for nitrogen (orange), the curves coincide. When argon gas is used (purple), the capacity is slightly reduced according to the manufacturer's specifications; consequently, the theoretical pressures are higher.

However, the measurement results for P_1 , see figure 3.16 a), suggest that the pumping capacity for neon (red) is below that for nitrogen (orange). Given identical conductance values and $C_1 \ll S_{P_1}$, the ratio of the pumping capacities for nitrogen and neon can be calculated via the pressure values. As a result, the pumping capacity for neon would amount to about 72% of that for nitrogen. Using the value for $S_{P_1}^{N_2}$ from table 3.1, this yields: $S_{P_1}^{Ne} = 0.72 \cdot S_{P_1}^{N_2} \approx 1400 \text{ L/s}$. This relation is useful in case further theoretical calculations are required. However, it should be noted, that this is only valid for the ideal, modelled case of identical conductance values for C_1 , independent of the gas type. The course of the argon curve (purple), which contrary to prediction lies below that for nitrogen, also suggests that the theoretical model for the distinction of the pressure profiles for different gases does not describe the measurement correctly. The negative curvature of the argon graph lacks a theoretical equivalent here as well. In conclusion, it must be stated that the gas-type dependent model for the target cell hole conductances is not applicable to the measurement series. Further investigation would require a significantly more precise theory description, which is not within the scope of this thesis.

In the following, both pressures in the inner and outer pre-chamber are discussed collectively due to the quantitatively similar results. The theory plots are provided in figures 3.16 d) and f), respectively, and exhibit a similar course and identical relative positions. The measurement results for P_2 and P_3 shown in c) and e) indicate the same relative positioning. Neon gas leads to the highest pressure values, followed by nitrogen and subsequently argon. This again points towards the assumption of differing gas specific pumping capacities (increasing in the stated order), in this case for the HP-300 and HP-80 pre-chamber turbo pumps. In addition, a correspondence of the orders of magnitude between the theory and the experiment is observed for all three types of gas.

As a result of the different values for the average velocity \bar{v} of argon, nitrogen and neon (see table 2.1), the conductance values in the tube model for the molecular regime as well as the pressure curves' slopes vary. The flow rate for neon gas marks

the maximum due to its high value for \bar{v} , followed by nitrogen and argon (in that order). The linear theory curves in figures 3.16 d) and f) are arranged correspondingly and exhibit slopes in accordance to the average velocities, starting at the lowest value for argon and, again, followed by nitrogen and neon. This configuration is reflected by the measurement data curves in c) and e). Furthermore, their evident linearity stems from the low pressure values within the pre-chamber system, and serves as further confirmation for the theoretical assumption to describe the pumping stages as tubes in the molecular flow regime. Differences between theory and measurement in quantitative terms are in part attributable to unconsidered effects of GF, special characteristics of the turbo pumps and potential leaks in the chambers and connection joints; these are not discussed in further detail within this thesis. First and foremost, however, the deviations again point to the necessity of a more detailed theoretical modelling for the different types of gas.

3.7 Concluding remarks for upcoming beamtime

Following the detailed description of the setup's characterisation with regard to the pressure conditions in all chambers using different target cells and types of gas, brief concluding remarks for the upcoming beamtime remain to be given. Here, the pivotal aspect is that with the help of the experiment's proposal [3] the necessary neon gas target cell pressure can be calculated, which leads to the same number of particles per area as in the theory calculations by Linda Young. This presumably results in the expected effects of resonant propagation and thus allows for an experimental verification of the applied theory. Said gas particle number per area within the chamber of length L is given by $\rho_A = N/A$. Its maximum value amounts to $\rho_A = 2 \cdot 10^{19} \text{ 1/cm}^2$ and is used in the following, since it was specified for the clear occurrence of propagation effects. Using the ideal gas law

$$P \cdot V = \frac{N}{N_A} \cdot R \cdot T, \quad (3.13)$$

as well as $V = A \cdot L$, the target cell pressure can be expressed as follows:

$$P_c = \frac{\rho_A \cdot R \cdot T}{N_A \cdot L}. \quad (3.14)$$

Here, $R = 8.314 \text{ m}^3 \cdot \text{Pa} / \text{K}^3 \cdot \text{mol}$ denotes the universal gas constant and $N_A = 6.022 \cdot 10^{23} \text{ 1/mol}$ refers to the Avogadro constant [21]. Using the same target cell type as before, the interaction length amounts to $L = 4 \text{ mm}$ while, again, room temperature is assumed. With $\rho_A = 2 \cdot 10^{19} \text{ 1/cm}^2$, this results in a predicted pressure value of:

$$P_C = 2.0 \text{ bar.}$$

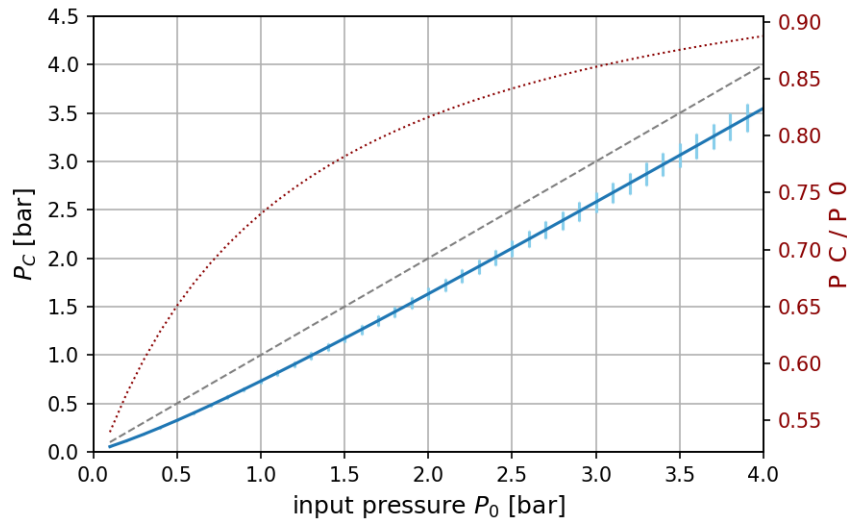


Figure 3.17: Resulting pressure values P_c in target cell (blue) compared to input pressure P_0 (grey); ratio of P_c and P_0 (red) with $P_c/P_0 \rightarrow 1$; for neon gas and target cell with $d = 100 \mu\text{m}$

Further, and in the same manner as for nitrogen in chapter 3.4.3 (see figure 3.10), a plot can be calculated from the neon measurement data that displays the target cell pressure P_c as a function of the *Festo* input pressure P_0 .

Figure 3.17 indicates that the theoretically predicted pressure value $P_c = 2.0 \text{ bar}$ is reached at a neon input pressure $P_0 = 2.4 \text{ bar}$. Reaching higher *Festo* input pressure values, such as the amply estimated maximum of 10 bar, is thus still a reasonable option since the occurrence of said resonant propagation effects is not yet confirmed experimentally. However, it is not necessary in order to achieve the set goal for $\rho_A = 2 \cdot 10^{19} \text{ 1/cm}^2$. All three sets of measured chamber pressure values (P_1 , P_2 and P_3) for neon gas are plotted logarithmically in figure 3.18 with respect to the target cell pressure P_c (see figure 3.17). A vertical line marks said target pressure of 2.0 bar, leading to the desired particle number per area ρ_A . This final illustration summarises the key findings for neon gas and provides an overview on the expected magnitudes of the chamber pressure values for the upcoming experiment.

As a final remark, the long-term measurement using neon gas, described in detail in chapter 3.3, demonstrated that the system, i.e. the *Festo* control valve and the turbo pumps, operates stably for an input pressure of $P_0 = 2.5 \text{ bar}$, when a

target cell with $d = 100 \mu\text{m}$ and $L = 4 \text{ mm}$ is employed. Only for input pressure values $P_0 > 3 \text{ bar}$ did the rotational frequency of the HP-2300 main chamber turbo pump begin to decrease in the corresponding measurement series. This suggests that under currently given conditions, it would presumably be possible to carry out the experiment at the desired particle density $\rho_A = 2 \cdot 10^{19} \text{ 1/cm}^2$ and the corresponding target cell pressure $P_C = 2.0 \text{ bar}$. Nevertheless, to avoid potential risk and to achieve higher pressure values, e.g. if the calculated value for the target cell pressure does not lead to the observation of resonant propagation effects in the experiment, a plan for the construction of a target cell with a reduced hole diameter should be developed. Chapter 3.5 indicates that the input pressure which can be applied quadruples for a cell with a halved aperture size, so for a $d = 50 \mu\text{m}$ hole an input pressure of 10 bar should be in range.

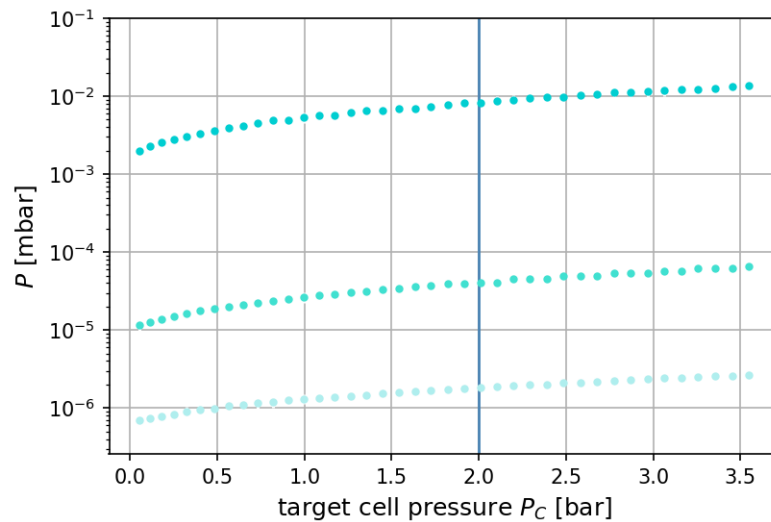


Figure 3.18: Measured pressure values in main chamber (P_1 : dark turquoise), inner (P_2 : medium turquoise) and outer (P_3 : light turquoise) pre-chambers for neon gas, plotted logarithmically in relation to target cell pressure P_C ; for target cell with $d = 100 \mu\text{m}$; vertical (blue) mark at $P_C = 2.0 \text{ bar}$ in accordance with $\rho_A = 2 \cdot 10^{19} \text{ 1/cm}^2$

4 Numerical simulation

Within the previous chapter 3, the target setup was presented and several technical challenges in the preparatory phase of the experiment were discussed as well as mostly solved. However, in addition to resolving practical issues of the setup, it is also of major significance to gain an idea of the physical results that are to be expected. This is the aim of the numerical simulation presented within this chapter. Whereas so far, the target pressure has been highlighted as the first central variable parameter of the experiment, the peak intensity of the laser pulse will be varied and its impact on the investigated $1s \rightarrow 3p$ resonance in neon will be discussed in the following. With the help of the software *LabVIEW*, a code has already been developed for previous experiments, which simulates the effects occurring during the propagation of ultra-short, resonant XUV laser pulses through helium gas (both for a simple two-level and a autoionising resonance; see [5, 16]). This code was adapted for the upcoming *EuXFEL* experiment (see [3]) and now provides numerical results for the interaction of high-intensity X-ray pulses with neon atoms. The mathematical procedure of this simulation is described in detail in [5] and [16] and is presented here in chapter 4.1 on the basis of the previously introduced theoretical background of quantum mechanics (chapter 2.3.1), absorption spectroscopy (chapter 2.4), x-ray lasers (chapter 2.1) and the relevant neon model (chapter 2.2). Subsequently, chapter 4.2 gives an overview of the results obtained with this simulation model for conditions as proposed in [3], which are reachable at the state-of-the art *EuXFEL*. Additionally, chapter 4.3 goes one step further with a transition to peak intensities beyond the proposed and experimentally feasible values. The observed absorption line shape changes form a reference back to the Fano formalism as introduced in chapter 2.4.2 and imply the possibility to deliberately manipulate said asymmetry of the electronic transitions in atoms in the X-ray spectral domain.

4.1 Mathematical basis of simulation method

As stated in chapter 2.3.1 on QM, the key challenge is to formulate the Hamilton operator as a matrix such that solving the SEQ, in turn, yields the solution to the QM problem at hand. It should be noted, that the neon gas is assumed dilute enough in the framework of this model that propagation effects can be neglected and the iteration between SEQ and Maxwell equations as in [4] can be omitted. For the proposed experiment, this simulation can thus be regarded as conducted in the low-pressure limit. The rather complex electronic interactions within the neon atom are, as a first approach, reduced to a simple two-level transition analogue to the one in [16]. The corresponding Hamiltonian is presented in equation 4.1 and

comprises both the ground state energy $E_g = \epsilon_0 = 0$ eV and that of the excited state $E_e = 867.5$ eV on its diagonal. The decay of the latter according to the introduced Auger channel is included simply in the form of the corresponding rate $\Gamma_e = 0.0099$ a.u. ≈ 0.27 eV. This leads to:

$$\mathcal{H} = \begin{pmatrix} E_g & d_{e,g} \cdot E(t) \\ d_{e,g} \cdot E(t) & E_e + i \frac{\Gamma_e}{2} \end{pmatrix}. \quad (4.1)$$

The X-ray laser is simulated as a driving electric field $E(t)$ as explained in chapter 2.1. The field's envelope is of Gaussian shape and entails the pulse duration $t_{FWHM} = 0.5$ fs in chapter 4.2 and $t_{FWHM} = 0.2$ fs in chapter 4.3. Under these respective conditions, the simulated pulse can be seen as one of the several temporal spikes within the longer duration of an FEL pulse, proposed in [3] as 25 fs. Since both values of t_{FWHM} lie well below that of the excited state's lifetime $\tau = \hbar/\Gamma_e \approx 2.4$ fs, the so-called 'impulsive limit' holds. Therefore, the resonance position is not shifted and remains on the initial level after the short interaction duration. Instead, a changed asymmetry of the absorption line is observed in some of the following cases. Further, the simulation only accounts for the ground and excited states of the introduced relevant level system of the neon atom in order to investigate potential strong coupling effects as line shape changes. Further states are thus neglected in this first simulation run and can be added in the future. Accordingly, only the dipole matrix elements $d_{g,e} = 0.0077$ and $d_{e,g} = d_{g,e}$, which describe the coupling of the two states in dipole approximation, enter the Hamiltonian. Its off-diagonal elements are the product of these dipoles and the electric field strength.

The aim of the numerical procedure introduced in the following is to solve the SEQ (see equation 2.9) for the above given Hamiltonian. For this, a discrete time grid with a resolution of $\Delta t = 0.01$ a.u. ≈ 24 as is chosen. The simulation time thereby amounts to 3200 a.u. ≈ 77 fs. For each of these steps, a numerical diagonalisation of \mathcal{H} is carried out. This leads to E_i , the energy eigenvalues of the diagonalised matrix (with $i = 1, 2$). The state vector onto which the Hamiltonian is applied in the SEQ contains the complex-valued coefficients of the two atomic states in the bare atomic Hilbert space before diagonalisation and reads:

$$|\Psi(t)\rangle = \left[c_g(t), c_e(t) \right]^T. \quad (4.2)$$

Here, c_g refers to the ground state, which is exclusively populated in the beginning; therefore $c_g(t=0) = 1$ is set. Hence, $c_e(t=0) = 0$ applies for the excited state. The representation of this vector in the diagonalised Hilbert space enables the

simple mathematical implementation of the state coefficients' propagation in time by multiplication with the phase factor $e^{-iE_i \cdot t/\hbar}$ according to equation 2.11. In total: for each time step, the initial state is transformed from the atomic into the diagonal Hilbert space in order to apply the time propagation. Thereafter, it is again transformed into the initial atomic space and thus provides the starting point for the next time step. Using c_g as well as the complex conjugate (*) of c_e , the complex-valued, time-dependent dipole moment $d(t)$ can be expressed as:

$$d(t) = d_{e,g} \cdot c_g(t) \cdot c_e^*(t). \quad (4.3)$$

The frequency spectrum of the dipole $d(\omega)$ follows as the result of the Fourier transform $\mathcal{F}\{d(t)\}$ and enables the computation of the optical density $OD(\omega)$ according to equation 2.18. Here, $\eta = 10^{-4}$ is set sufficiently low to prevent the occurrence of macroscopic propagation phenomena. The OD accounts for the interference effects occurring between the electric field and the dipole response of the matter. In the strong field regime, these temporal effects are made visible within the changed line shape asymmetry, which is also expected to occur in the here presented model. If so, than dressed states, shifts of the eigenstates' energies and the onset of Rabi oscillation should arise in this simulation during the short interaction time of the electric field with the neon atoms (as explained in chapter 2.3.2). These shifts depend on the detuning and lead to $\Delta\phi$, a phase offset of the dipole response. Subsequently, this relative alteration with respect to the driving field results in a change of the Fano parameter q and is reflected in the OD in the form of a changed transition line shape asymmetry. To find out, whether these well-known energy and phase shifts also occur for the case of X-ray laser pulses interacting with neon atoms, the simulated line shapes are fitted in accordance with Fano's formalism as follows:

$$OD(\omega) = A \cdot \frac{(q + \epsilon(\omega))^2}{1 + \epsilon^2(\omega)} + B. \quad (4.4)$$

A combination of equations 2.15 and 2.19 as well as 2.20 for the reduced photon energy $\epsilon(\omega)$ leads to an expression for the absorption line shape encoded in the OD (left hand side of equation 4.4) and described by a Fano line shape (right hand side). This includes the fitting parameters A and B for the amplitude and offset, respectively. The reduced photon energy is dependent on the centre frequency ω via $E = \hbar \cdot \omega$.

Finally, the Fano parameter q , obtained by this fitting procedure, can be converted into the temporal dipole phase shift $\Delta\phi$ by means of 2.21. As outlined in [18], the absorption profile retains Lorentzian form in the weak field case, while reaching

the intensities of the strong field regime makes it feasible to modify the asymmetry, given the aforementioned impulsive limit. As illustrated in figure 2.5, the separation of the eigenstates' energy levels grows stronger with increasing intensity and is also dependent on the detuning. In order to study the resulting effects for various conditions in detail, the simulation is run for different detuning values and varying peak intensities. The results are presented and analysed in the subsequent two chapters. At this point, it is important to emphasise that the two-level simulation does not account for the effects of Raman scattering and 1s-photoionisation presented in the theory chapter.

4.2 Simulations for state-of-the-art XFEL peak intensities

In figure 4.1 the first simulation (fit) results, i.e. the q parameter and corresponding dipole phase shift of the resonance line shape for different detunings and peak intensities, are presented. Hereby, a pulse with $t_{FWHM} = 0.5$ fs as described above, centred in the energy domain around $E_e = 867.5$ eV in the case of zero detuning, is utilised. This ultra-short duration is chosen to match a single coherent temporal spike within the longer and only partially coherent full SASE pulse. Given the minimum duration-bandwidth product introduced in chapter 2.1, 0.441 for the Fourier-limited Gaussian pulses at hand, this covers an energy range with a spectral bandwidth of 3.6 eV. To ascertain whether the known line shape asymmetry changes known from both FEL experiments and theory calculations for helium (see [16]) can also occur for the given neon model, interacting with X-ray pulses, the simulation was repeatedly carried out for peak intensities below $I_0 = 10^{18}$ W/cm² and different detunings ($\Delta = \pm 2$ eV). The absorption line shape changes were analysed in the same manner as in the previous theoretical works. The peak pulse intensity constitutes the horizontal axis in figure 4.1 and corresponds to the proposed values in [3]. Furthermore, a detuning range of $\Delta/E_e \approx \pm 0.2\%$ was covered which lies within the bandwidth of the pulse and thus the OD for the absorption line can be calculated without numerical problems. The detuning, in turn, marks the vertical axis in figure 4.1. In a), the third dimension, shown here by means of colour coding, illustrates the results of the fitting procedure for the Fano parameter with help of equation 4.4. This can be transformed into the dipole phase shift $\Delta\phi$ using equation 2.21, which is displayed in figure 4.1 b).

First looking at the lowest peak intensities ($I_0 \approx 0.1 \cdot 10^{18}$ W/cm²), q converges to $\pm \infty$ (white and black in figure 4.1 a), respectively); the value of the phase shift is correspondingly around 0, (nearly) independent of the detuning (green in figure 4.1 b)). Thus, resonances with Lorentzian shape can be seen in the OD for lowest peak intensities. For higher values, both plots in figure 4.1 show close resemblance

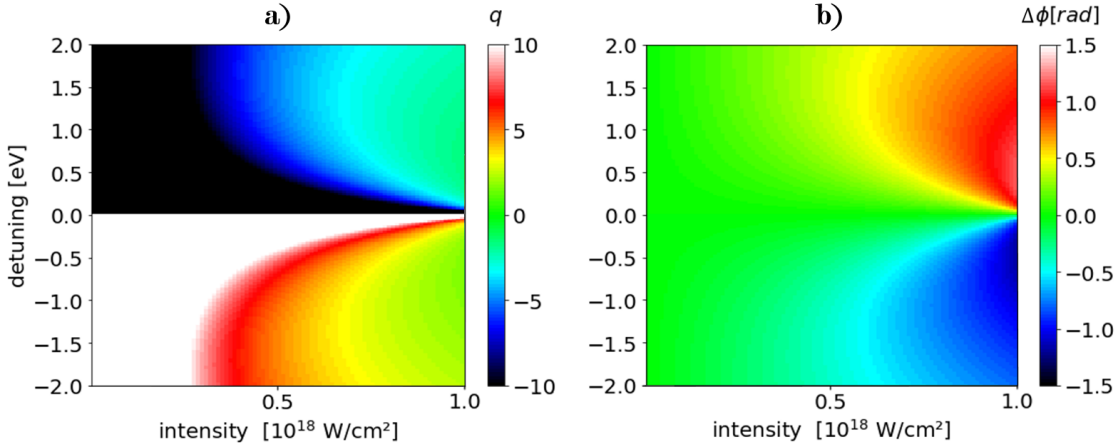


Figure 4.1: Simulation results for two-level neon system for varying detuning ($\Delta/E_c \approx \pm 0.2\%$) and peak intensity values up to 10^{18} W/cm^2 , corresponding to [3]; a) Fano parameter q and b) dipole response phase shift $\Delta\phi$ obtained via fitting of numerically calculated OD using equation 4.4

to the corresponding plots in [16]. This prominently demonstrates that the absorption line shape can be modified, leading to changes in q from $+\infty$ (white in figure 4.1 a)) to ≈ 2 (green with yellow tinge) for $\Delta < 0$ and from $-\infty$ (black) to ≈ -2 (green with blue tinge) for $\Delta > 0$. This corresponds to dipole phase shifts from 0 (green in b)) to ≈ -1 (blue) for $\Delta < 0$ and to ≈ 1 (red) for $\Delta > 0$. Thus, in the case of red detuning, the Fano parameter takes on positive values while the opposite is true for blue detuning. This divergence of q leads to the clear inversion of colours in the mirrored sides above and below $\Delta = 0$ in figure 4.1 a). The increase of the absolute value of q for outer detuning regions and thus the 'arc-like' structure can be explained in terms of averaging effect. Again describing the range of high peak intensities in figure 4.1, now for the case of central detuning, the same observation is made as for the lowest peak intensities. This is also due to said averaging effects. The pulse's spectral components are equally distributed on both sides of the resonance and induce correspondingly spread dressed states. Since the value of $\Delta\phi$ depends on their energy shift, which is equal in magnitude but opposite in sign when switching the sign of Δ , the effects of red and blue detuning cancel out, resulting in a phase shift of 0. For details the reader is referred to [16].

The increased and decreased values of q for higher intensities as well as red and blue detuning, respectively, represent a growing line shape asymmetry. The sym-

metrical structure along the detuning axis of the plots (in figure 4.1 a) and b)) indicates that the absorption line shape is mirrored vertically for detuning values of identical magnitude but changing signs; apart from that, it exhibits the same characteristics. Consequently, the absolute value of the phase shift also grows along with that of the Fano parameter; however, due to the minus sign in equation 2.21 for $q(\Delta\phi)$, with the opposite sign. For later considerations it is important to mention that the value of $\Delta\phi$ in the off-resonant case for fixed blue (red) detuning monotonously increases (decreases) while it exhibits the constant value zero in the resonant case.

As discussed in the paper [16], on which the here presented simulations are based, the underlying simulation method is presented along with an analysis of the results for helium atoms and XUV pulses. In that case, the peak intensity ranges in the order of 10^{15} W/cm². The findings in figure 4.1 are in close correspondence with those shown in [16]. Therefore, similar line shape changes are found within this simulation chapter for the more complex neon atom when irradiated with more intense X-ray lasers given the proposed peak intensities (up to 10^{18} W/cm²) for the upcoming experiment.

4.3 Outlook for high intensities

In this chapter, plots of the simulation results for the OD in the intensity range above 10^{20} W/cm² are presented and evaluated with regard to the occurrence of window resonances. These results are not based on a fit, whereby errors of the fit routine can be ruled out. Since intensities of this order of magnitude are not achievable with the *EuXFEL*, the following is to be understood as a simulation-based outlook for potential future experiments. At the outset, it should be noted here that the aforementioned phenomenon of window resonance occurs if the Fano parameter q becomes zero, i.e. if $\Delta\phi$ is equal to odd multiples of π . Thereby, resonant amplification leads to X-ray gain. While this may appear at increased intensities due to a changed absorption line asymmetry, the effect usually occurs as a result of population inversion. If the excited state is populated by more electrons than the ground state, processes of spontaneous and (due to the resonant laser) stimulated emission lead to an increased intensity of the transmitted spectrum in the range of the resonance energy. Therefore, in the later part of this chapter, the evolution of the populations during the interaction period will be discussed.

In the following, the OD is plotted for fixed values of either the peak intensity or the detuning in order to analyse and understand the accordingly arising effects. For both parameters, three different values are chosen: blue, red and resonant detuning (± 15 eV and 0 eV, respectively) as well as low, intermediate and high

peak intensities ($3.2 \cdot 10^{18} \text{ W/cm}^2$, $3.3 \cdot 10^{20} \text{ W/cm}^2$ and $6.5 \cdot 10^{20} \text{ W/cm}^2$, respectively). Here, the three cases of fixed high peak intensity (figure 4.2), resonant detuning (figure 4.3) and red detuning (figure 4.4) are displayed to discuss the main findings. The complete results are presented in the appendix A.4 for a more detailed view.

Figure 4.2 displays the results for the spectral OD as a function of only the detuning and not the intensity, again by use of a colour code. For this simulation run, a peak intensity of $I_0 = 6.5 \cdot 10^{20} \text{ W/cm}^2$ was fixed to first look only at the detuning dependent effects of the OD. This lies roughly two orders of magnitude above the intensity value considered in the previous chapter. It should be noted that pulses with $t_{FWHM} = 0.2 \text{ fs}$, corresponding to a now broader spectral bandwidth of 9.1 eV , were used. Moreover, a detuning range of $\pm 15 \text{ eV}$ was chosen, which equals $\Delta/E_e = \pm 1.7\%$ of the pulse's resonance energy. This detuning can still be regarded as nearly-resonant, albeit allowing for a broader investigation in direct contrast to figure 4.1.

Analysing figure 4.2, it is striking that no positive OD values are present for the highest peak intensity value ($I_0 = 6.5 \cdot 10^{20} \text{ W/cm}^2$). Especially, no magnitude can be observed for central detuning; it approximately amounts to zero at this level, visualised by means of green colouring. The unit of the OD is of little significance in all of the plots presented. Instead, the focus lies on the description of qualitative observations. Generally speaking, a yellow and red plotted, positive value indicates absorption during the propagation of X-ray laser pulses through neon gas. The transmitted light is attenuated in comparison to the incident light. A negative OD, on the other hand, depicted here in blue and black color coding, indicates an amplification of light. This can occur for Fano lines of asymmetric shape with $q \neq \pm \infty$, that correspondingly exhibit negative values for the absorption cross section. If the region of negative OD coincides centrally with the resonance, i.e. 867.5 eV in the considered application, window resonance is present. Accordingly, the vertically symmetrical blue coloured areas for maximum and minimum detuning are striking in figure 4.2 as they indicate such window resonance. In order to compare different results for the OD for different detuning values and to understand the contrast to the previous findings outlined in chapter 4.2, the minimum and resonant detuning values are fixed in the following figures 4.3 and 4.4, respectively. The OD is thus plotted as a function of the peak intensity, ranging from $3.2 \cdot 10^{18} \text{ W/cm}^2$ up to $6.5 \cdot 10^{20} \text{ W/cm}^2$. Due to the observed symmetry, only the lower range ($\Delta = -15 \text{ eV}$) is regarded in the following. The result for maximum blue detuning ($\Delta = 15 \text{ eV}$) can be found in the appended figure 5.3 f) and features total mirror symmetry with respect to the photon energy axis compared to figure 4.4. It is thus not further discussed here.

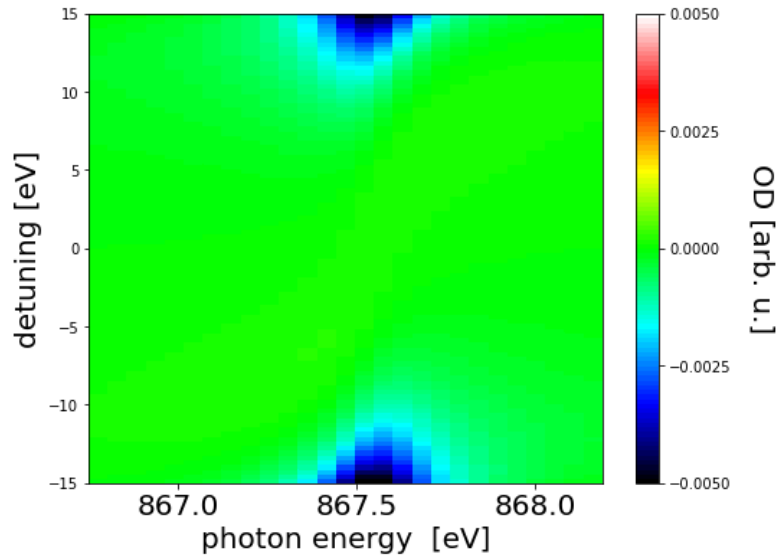


Figure 4.2: Simulation results for OD plotted as function of pulse detuning ($\Delta/E_e = \pm 1.7\%$) and photon energy for fixed highest peak intensity value $I_0 = 6.5 \cdot 10^{20} \text{ W/cm}^2$

Figure 4.3 displays the results for the peak intensity dependent OD, employing resonantly driving pulses. It is apparent that only symmetrical, i.e. Lorentzian, line shapes occur for photon energies around 867.5 eV in the course of increasing peak intensity. For the lowest intensities displayed, strong resonant absorption is apparent (white and red colouring), followed by a short interval of unhindered transmission for peak intensities of around $0.4 \cdot 10^{20} \text{ W/cm}^2$ (green colouring). Next, a (black and blue coloured) region of window resonance for I_0 between $0.5 \cdot 10^{20} \text{ W/cm}^2$ and $1.3 \cdot 10^{20} \text{ W/cm}^2$ is observed, again followed by a green coloured transmission range from $1.3 \cdot 10^{20} \text{ W/cm}^2$ up to $1.7 \cdot 10^{20} \text{ W/cm}^2$. With increasingly larger intensity intervals and likewise decreasing spectral line width, this sequence of absorption, transmission and resonant amplification is repeated a second time for I_0 starting from $1.7 \cdot 10^{20} \text{ W/cm}^2$ and reaching beyond $6.5 \cdot 10^{20} \text{ W/cm}^2$. The increase in the intervals' sizes stem from the method of plotting. Were the vertical axis to represent the electric field strength, rather than its squared value (the intensity), the distances would be equal. The weakening of the structures is attributable on the one hand to the decay of the excited state. On the other hand and more importantly, the influence of the polarisation response in the numerator of the OD (see equation 2.18) decreases for increasing intensities. Its value oscillates within a constant interval, while the squared electric field strength in the denominator continues to grow. For the maximum observed intensity, the OD is again valued zero, which

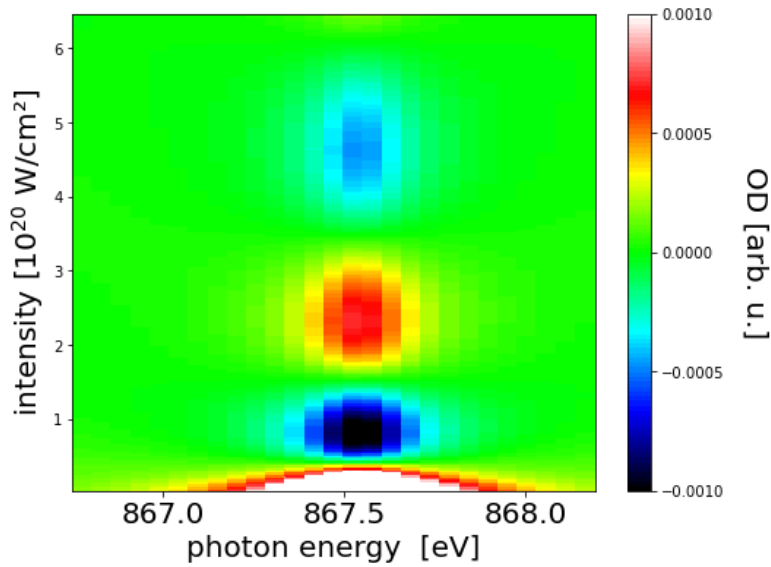


Figure 4.3: Simulation results for OD plotted as function of peak intensity up to $I_0 = 6.5 \cdot 10^{20} \text{ W/cm}^2$ and photon energy for fixed resonant detuning value $\Delta = 0 \text{ eV}$

is in agreement the central detuning region in figure 4.2. At $\Delta = 0 \text{ eV}$ and for $I_0 = 6.5 \cdot 10^{20} \text{ W/cm}^2$, this plot displays the exact same unperturbed transmission (OD valued zero) by green colouring. Overall, this can be interpreted as a gradually attenuated oscillation of the amplitude for increasing intensity. However, since in this case of resonant detuning only symmetrical absorption line shapes occur, a continuous change of the phase shift $\Delta\phi$ and thus of the Fano parameter q is not to be considered the cause of this oscillation. The underlying physics of said findings are addressed below when the state populations are discussed.

Prior to presenting the case of fixed minimum detuning in figure 4.4, an important remark is to be made at this point. For the following analysis, the lower section of figure 4.2 was chosen, since the photon energy for the upper case lies at 882.5 eV and thus well above the K-edge of neon atoms. Therefore, in the actual experiment, $1s$ -photoionisation processes would take place abundantly. The ensuing ions would in turn exhibit new resonances in interaction with the X-ray laser pulses and lead to a pattern of the OD that differs from the simulated one. To model these processes adequately, it would be necessary to add additional energy levels to the *LabVIEW* code. Corresponding results can be found in the paper [4], however, they were not included here with regard to the scope of this thesis. For the now considered case of fixed minimum detuning, a similar restriction is given. With a central photon energy at 852.5 eV , increased stimulation of the Raman scattering

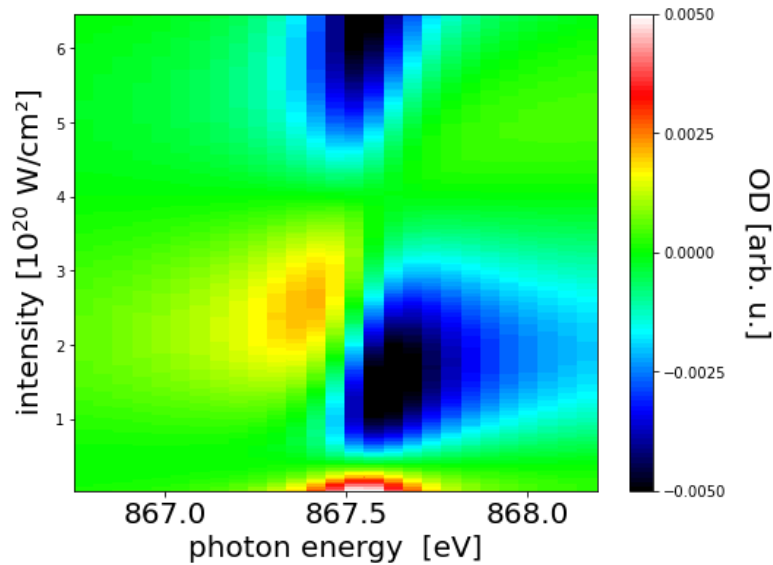


Figure 4.4: Simulation results for OD plotted as function of peak intensity up to $I_0 = 6.5 \cdot 10^{20} \text{ W/cm}^2$ and photon energy for fixed red detuning value $\Delta = -15 \text{ eV}$

process, introduced in chapter 2.3.3, would arise in the experiment. To account for this in the simulation, the inclusion of the valence excited state $|1\rangle$ from figure 2.4, i.e. a three-level system, would be required. Since this is an effect to be investigated in the upcoming experiment, the lower case is selected for description. This is sufficient for the investigation of the phenomenon of resonant amplification. Still, for future analyses of the theoretical expectations, the inclusion of these additional energy levels is advisable.

Next, the case of intensity dependent OD for fixed red detuned driving pulses, shown in figure 4.4, is described in the following. Analogue to the analysis of figure 4.3, the spectral lineouts along the increasing peak intensity axis of the OD are discussed. First, a region of positive resonant absorption is observed for the lowest intensities. This is followed around $I_0 = 0.4 \cdot 10^{20} \text{ W/cm}^2$ by a short (green coloured) peak intensity range with OD values at zero and an asymmetric OD thereafter for I_0 between $0.5 \cdot 10^{20} \text{ W/cm}^2$ and $3.5 \cdot 10^{20} \text{ W/cm}^2$. For instance, at $I_0 = 2.0 \cdot 10^{20} \text{ W/cm}^2$, an amplification of light (in correspondence with negative OD values) occurs for photon energies around and above the resonance energy of 867.5 eV. For lower photon energies, on the other hand, an attenuation of light is apparent due to the emergence of asymmetric absorption line shapes, i.e. Fano line shapes. At even higher peak intensities between $3.5 \cdot 10^{20} \text{ W/cm}^2$ and $4.5 \cdot 10^{20} \text{ W/cm}^2$, yet another section of vanishing OD follows. Eventually, a region

of resonant amplification, the window resonance expected from figure 4.2, is observed around $I_0 = 6.0 \cdot 10^{20} \text{ W/cm}^2$.

In contrast to the case of resonant detuning described above (figure 4.3), the phase shift of the dipole response seems to perform a continuous rotation for minimum red detuning, accompanied by a monotonic variation of the Fano parameter. With increasing peak intensity, the intrinsic, unperturbed Lorentzian absorption line shape is modified into an asymmetric Fano region and ultimately into a symmetric (but negative) window resonance. This corresponds to a progression of q from $\pm \infty$ to positive and finite values up to $q = 0$ for $I_0 = 6.5 \cdot 10^{20} \text{ W/cm}^2$. Further, this can also be associated with the evolution from $\Delta\phi = 0$ to positive values $0 < \Delta\phi < \pi$ and eventually $\Delta\phi = \pi$. In order to further elucidate the difference in the OD between the resonant and the red detuned case, an analysis of the states' population coefficients is conducted and presented in the following.

Figure 4.5 illustrates the difference in the population probabilities $P_g(t) = |c_g|^2$ and $P_e(t) = |c_e|^2$ (see chapter 2.3) between the two bare atomic states (ground and excited) of the simplified two-level neon system. This is presented for resonant and minimum red detuning in the same way as for the two preceding OD plots (figures 4.3 and 4.4). For times $t < -0.5 \text{ fs}$, both plots display the value $|c_e|^2 - |c_g|^2 = 0 - 1 = -1$ according to the aforementioned initial condition that only the ground state is populated before the X-ray pulse interacts with the system. During the interaction period, centred around 0 fs, resonant excitation then ensues for both cases and the population is shifted from the ground to the excited state.

In the case of centre detuning (figure 4.5 a)), not only population inversion is obtained, i.e. the difference of the population probabilities lies above zero, but even a full population shift from the ground to the excited state is reached (indicated by $|c_e|^2 - |c_g|^2 = 1$). The population difference then falls again, back to ≈ -1 , before (almost) the same cycle occurs for a second time (second peak in figure 4.5 a)). This process of shifting the state population back and forth is well-known from the Rabi oscillations introduced in chapter 2.3.2 for the case of monochromatic driving lasers. After the interaction with the laser pulse (for $t > 0.5 \text{ fs}$, the current population configuration is nearly preserved. The weakly populated excited state subsequently exhibits a barely visible decay, noticeable in the decrease of $|c_e|^2 - |c_g|^2$ and corresponding to the Auger process with an lifetime of 2.4 fs, which would be better visible if a longer time window was provided. The repeated emergence of the population inversion helps to explain the amplitude oscillation of the symmetric absorption line shapes as observed in figure 4.3. A detailed de-

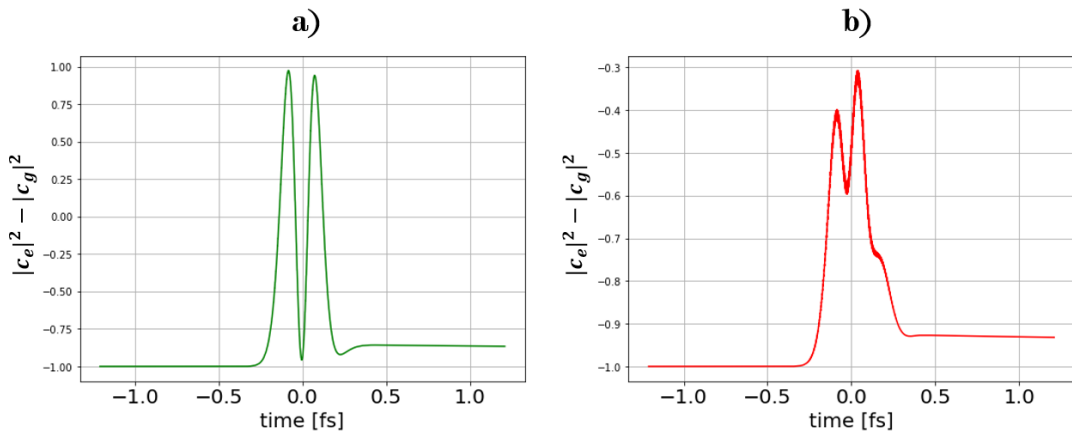


Figure 4.5: Simulation results for difference of population probabilities of excited and ground state for highest peak intensity value $I_0 = 6.5 \cdot 10^{20} \text{ W/cm}^2$ and for **a)** resonant detuning $\Delta = 0 \text{ eV}$ and **b)** minimum red detuning $\Delta = -15 \text{ eV}$

scription of this connection between the Rabi oscillation of the state population and the intensity-dependent variation of the absorption line amplitude is provided in [17].

Compared to the previously described case, the value of the population probability difference plotted in figure 4.5 for the minimum red detuning ($\Delta = -15 \text{ eV}$) lies below zero at all times. Consequently, population inversion never occurs and is thus excluded as a cause for the continuous change of symmetry with increasing peak intensity and especially for the observed negative OD values corresponding to transient X-ray amplification in figure 4.4. As explained earlier, it can therefore be concluded that in the off-resonant case the occurrence of window resonance regions is attributable to an intensity-dependent change in the Fano parameter q alongside a phase shift $\Delta\phi$ of the dipole response, thereby allowing for transient X-ray gain in the resonance photon energy without the need for an otherwise expected population inversion. This is an interesting finding in itself, which requires further and more detailed investigation, which is, however, beyond the scope of this thesis.

In conclusion, it remains to be noted that the deductions made in the previous chapter 4.2 for experimentally realistic intensities are also valid in the range of strongly increased intensities. Exclusively symmetrical absorption lines occur in the resonant case. Here, the population inversion causes an oscillation of the amplitude depending on the peak intensity and thus areas of window resonance arise. The off-resonant case shows a monotonic increase of $\Delta\phi$ with growing values

of I_0 , resulting in alternating asymmetric and symmetric regions in the OD. The latter also leads to the phenomenon of window resonance whenever $q = 0$ applies. As the final consideration of $|c_e|^2 - |c_g|^2$ confirms for the investigated peak intensity range, the resonant X-ray gain is not linked to the effect of population inversion in this case of minimum red detuning. Instead, the approach of transient dipole phase shifts leading to asymmetry changes of the spectral absorption lines shapes, described by the Fano formalism, provides an explanation for the amplification of resonant light.

5 Conclusion

The aim of the conducted project, as the title of this thesis suggests, was to contribute '*towards ultra-fast X-ray transient spectroscopy in high density neon gas*', to develop and test a gas flow model for the experimental setup and to make predictions based on the results of numerical simulations. To achieve this aim, relevant fundamentals of laser theory, the neon atom, light-matter interaction, absorption spectroscopy and gas flow were introduced first. This was followed by a detailed description of the target setup, which was constructed at the *Max Planck Institute for Nuclear Physics* in Heidelberg as a part of the subsequent collaborative experiment in Hamburg.

Chapter 3 on the experimental setup and the conducted measurements concluded by comparing the findings with the particle number density $\rho_A = 2 \cdot 10^{19} \text{ 1/cm}^2$ proposed by Linda Young in [3]. It was thus found that said value is already achievable under given conditions, i.e. an input pressure of $P_0 = 2.4 \text{ bar}$ can be set over a longer period of time. The anticipated propagation effects are expected to occur in the absorption spectrum, given this condition. Nevertheless, the reduction of the target cell hole diameter is particularly desirable in order to achieve even higher input pressure values.

The first measurements carried out lead to the conclusion that the newly employed *Festo* pressure control unit operates reliably, i.e. it allows the input pressure value to be set with satisfactory accuracy and reproducibility and also maintains it over sufficiently long periods of time.

The following series of measurements confirmed that the developed model of the conductances for individual components and thus the pressure conditions in the chamber system provides a satisfactory description of the experimental results. The central finding here was that the target cell holes are best characterised as apertures in the viscous flow regime, while the pumping stages between the chambers approximately comply with the model of tubes in the molecular flow regime. Furthermore, a conductance value for the gas inlet system leading from the *Festo* control valve to the interior of the target cell was obtained in this context. Thus, a valuable prediction of the actual target pressure, available in the area of laser propagation throughout the cell, was made. At the time of completion of this thesis, development of a set-up for the exact determination of the target cell pressure, employing an interferometer, has begun.

Furthermore, a comparative measurement for two target cells with different hole diameters led to the conclusion of a quadratic relationship between the increase of said diameter and of the pressure values within the main chamber. This corresponds to the mathematical description of aperture conductances. Consequently, it is of great interest to reduce the diameter of the cell opening further beyond the

hitherto minimum of 100 μm . One way to achieve this would be to mask a cell with aluminium foil and use needles to pierce appropriate holes. Since this has already proven to be a complicated and unreliable method, the following option is to be preferred. Thanks to its high beam intensity, the *EuXFEL* is capable of burning holes in the thin walls of a sealed cell. This ensures that the size of the resulting openings is perfectly matched and also facilitates the alignment of the cell. Lastly, it should be noted that the conception of a new cell design has also been considered, which would involve the clamping of externally purchased metal plates with prefabricated small holes to close the cell. All of these modifications would enable to obtain even higher pressures within the target cell without reducing the main turbo pump's rotational frequency and thereby eventually breaking high vacuum conditions.

Subsequently, the measurement results for the comparison of the operation using different types of gas were presented. These indicate that the assumed values for the turbo pumps' pumping capacities do not comply with the experimental conditions. Contrary to the manufacturer's specifications, it is thus suggested that argon was pumped most efficiently, followed in that order by nitrogen and neon gas. The measurement data also point towards the theoretically expected direct correlation between the pressure values in the pre-chambers and the average velocity of the gas used. However, with regard to the overall results, it must be noted that the theoretical model for the description of different gases has yet to be improved considerably. This is of particular importance, since, after carrying out the proposed experiment with neon gas, other atoms and molecules can be studied using the same setup. For instance, in [3], a plan is introduced to subsequently investigate xenon and krypton. Another upcoming experiment is presented below.

In chapter 4, the second portion of this thesis' main part, the mathematical foundations of the numerical simulation were outlined. After adapting the *LabVIEW* code for neon gas and X-ray laser pulses in resonance with the $1s \rightarrow 3p$ excitation, realistic experimental conditions (i.e. peak beam intensities below 10^{18} W/cm^2) were simulated first. The results are comparable to those found in previous numerical studies for helium and XUV laser pulses. Both Fano parameter and dipole response phase shift remain unchanged for increasing intensities in the resonant detuning case, the absorption lines thus exhibit (symmetrical) Lorentzian shape. In the off-resonant case (red or blue detuning), the absolute value of q decreases monotonically with growing peak intensity; $\Delta\phi$ changes continuously and, thus, also the absorption line shape asymmetry. However, the case of $q = 0$ is only reached for intensity values increased beyond the realistic limit. For this purpose, OD plots with fixed detuning or intensity values were analysed. In the resonant case, population inversion occurs, the amplitude of the OD oscillates without any changes

in symmetry and areas of window resonance occur. These can also be identified in the case of off-resonant detuning; here, however, within a monotonic change of the Fano parameter. Overall, important insights into the coupling effects of the neon atom's ground and excited states and into the possibility of targeted manipulation of absorption line shape asymmetry were gained in the course of these analyses. In order to make more accurate predictions based on numerical simulations, it is essential to include the $1s$ -ionisation channel as well as the introduced valence excited state, and thus the Raman scattering process, in the underlying model.

A number of perspectives on possible optimisations and investigations beyond the scope of this thesis have already been mentioned. Now a final remark should be made here, concerning another proposed experiment (see [24]). Here it is intended to follow up the first neon gas experiment at hand with an analysis of carbon monoxide (CO), employing the same set-up. Thus, instead of an atomic gas, molecular matter now comes into play. The central idea is to use a two-colour pulse of the *EuXFEL* in order to, first, induce a core excitation in the oxygen atom; this requires a photon energy of 534 eV. The second and far less intense pulse causes stimulated Raman scattering near the K-edge of oxygen, i.e. at a photon energy of about 525 eV. In this case, too, the transmitted spectrum allows conclusions to be drawn about such interaction processes. And once again, it is necessary to compare the theoretical expectations with the experimental findings obtained via resonant absorption spectroscopy. Thereby, the experiment opens up the possibility to investigate light-induced chemical reactions, to advance the methods of absorption spectroscopy and to gain new fundamental insights into the electronic structures and laws of the applied carbon monoxide gas.

Further investigation would be desirable at almost every turn of this thesis, even within the limited scope of a bachelor's project. Experienced researchers (such as the proposers of this experiment) cultivate this strive for new and wider understanding in the methods of science, in the development of **theories** and the conduct of insightful **experiments**. Thereby, basic research means observing the **'becoming'** of things, just as the interaction of X-ray laser **light** with gaseous neon **matter** is to be observed in the presented case. The aim is to infer the **'being'** of things, in this context the electronic structures and laws of the neon atom. Every small contribution and every major breakthrough constitutes the essence of physics, invigorated by basic research, devoid of the need for justification besides human curiosity. Within the limited scope of this thesis, theory models have been developed for two aspects of the experiment at hand: the gas flow and the emerging interaction effects. These were then tested for their validity in comparison with previously established as well as newly measured results.

References

- [1] Anton F. Koch. Milestones in the history of philosophy, 4 2020. Script for a lecture at the faculty of philosophy, Heidelberg University.
- [2] European X-Ray Free-Electron Laser Facility GmbH. Euxfel. https://www.xfel.eu/facility/overview/index_eng.html. Accessed: 2021-07-02.
- [3] Linda Young et al. X-ray transient absorption from the weak- to strong-field regime, 6 2019. Proposal for the experiment at hand.
- [4] Kai Li, Marie Labeye, Phay J. Ho, Mette B. Gaarde, and Linda Young. Resonant propagation of x-rays from the linear to the nonlinear regime. *Physical Review A*, 102, 11 2020.
- [5] Alexander Magunia. Doubly-excited helium strongly driven with short and long wavelength pulses. Master's thesis, Ruperto-Carola-University of Heidelberg, Germany, 12 2018.
- [6] Thomas Ding. *Quantum dynamics in weak and strong fields measured by XUV nonlinear spectroscopy*. PhD thesis, Ruperto-Carola-University of Heidelberg, Germany, 2018.
- [7] Jean-Claude Diels and Wolfgang Rudolph. *Ultrashort Laser Pulse Phenomena, 2nd Edition*. Academic Press, 2 edition, 2006.
- [8] Lukas Röhrich. External coupling and modifications to an ultra-fast laser pulse setup to allow higher infrared peak intensities. Bachelor's thesis, Ruperto-Carola-University of Heidelberg, Germany, 4 2021.
- [9] Matthias Bartelmann et al. *Theoretische Physik*. Springer Spektrum, Berlin/Heidelberg, Germany, 10 edition, 2014.
- [10] David Attwood and Anne Sakdinawat. *X-Rays and Extreme Ultraviolet Radiation*. Cambridge University Press, Cambridge, England, 2 edition, 11 2016.
- [11] Marc A. A. Rebholz. *All-XUV pump-probe transient absorption spectroscopy on the dissociation dynamics of small molecules*. PhD thesis, Ruperto-Carola-University of Heidelberg, Germany, 2020.
- [12] Hermann Sicius. *Handbuch der chemischen Elemente*. Springer Spektrum, Berlin/Heidelberg, Germany, 1 edition, 2021.
- [13] Clemens Weninger and Nina Rohringer. Stimulated resonant x-ray raman scattering with incoherent radiation. *Physical Review A*, 88, 11 2013.

-
- [14] Daniel C. Haynes, Markus Wurzer, Albert Schletter, et al. Clocking auger electrons. *Nature Physics*, 17, 1 2021.
- [15] Wolfgang Demtroeder. *Atoms, Molecules and Photons: An Introduction to Atomic-, Molecular- and Quantum Physics*. Springer Spektrum, Berlin/Heidelberg, Germany, 3 edition, 2 2019.
- [16] Alexander Magunia et al. Bound-state electron dynamics driven by near-resonantly detuned intense and ultrashort pulsed xuv fields. *Applied Sciences*, 10, 9 2020.
- [17] Alexander Magunia. Elektronen-korrelation in helium unter einfluss intensiver xuv-laserpulse. Bachelor's thesis, Ruperto-Carola-University of Heidelberg, Germany, 9 2016.
- [18] Christian Ott, Andreas Kaldun, Philipp Raith, Thomas Pfeifer, et al. Lorentz meets fano in spectral line shapes: A universal phase and its laser control. *Science*, 340, 5 2013.
- [19] John H. Moore, Christopher C. Davis, and Michael A. Coplan. *Building Scientific Apparatus - A Practical Guide to Design and Construction*. Westview Press, Cambridge, Massachusetts, 3 edition, 2002.
- [20] Pfeiffer Vacuum GmbH. *Know-how Book: The Vacuum Technology Book - Volume 2*. Asslar, Germany, 4 2013.
- [21] Wolfgang Demtroeder. *Experimentalphysik 1: Mechanik und Wärme*. Springer Spektrum, Berlin/Heidelberg, Germany, 7 edition, 5 2015.
- [22] Pfeiffer Vacuum GmbH. Turbopumps with hybrid bearing. <https://www.pfeiffer-vacuum.com/en/products/vacuum-generation/turbopumps/hybrid-bearing>. Accessed: 2021-07-12.
- [23] Pfeiffer Vacuum GmbH. Short instructions for compact full range gauge (user manual), 11 2005.
- [24] Alessandra Picchiotti, Nina Rohringer, et al. Stimulated rixs in carbon monoxide, 12 2020. Additional proposal.
- [25] Mette B. Gaarde, Christian Buth, Jennifer L. Tate, and Kenneth J. Schafer. Transient absorption and reshaping of ultrafast xuv light by laser-dressed helium. *Physical Review A*, 83, 1 2011.

Appendix

A.1 Derivation of equation 2.17 for $\sigma_a(\omega)$

Starting with equation 2.16 for the polarisation, the following derivation leads to expression 2.17 for the absorption cross section:

The susceptibility can be written in complex notation as $\chi = \chi'(\omega) + i\chi''(\omega)$. It relates to the material's refractive index n via

$$n(\omega) = \sqrt{1 + \chi(\omega)}. \quad (5.1)$$

As a next step, one needs to consider Lambert-Beer's law

$$I(\omega) = I_0(\omega) \cdot e^{-\rho_N \cdot \sigma_a(\omega) \cdot z}, \quad (5.2)$$

which describes light's reduction in intensity (with respect to the initial value) when propagating through an absorbing medium in z direction. For comparison, the fundamental expression for linear propagation of an electromagnetic wave (with the wave vector $k(\omega) = n(\omega) \cdot \omega/c$) must be appended:

$$E(\omega, z) = E(\omega, 0) \cdot e^{ik(\omega) \cdot z} \quad (5.3)$$

Using the approximation $n(\omega) \approx 1 + \chi'/2 + i\chi''/2$ for a dilute medium leads to:

$$E(\omega, z) = E(\omega, 0) \cdot e^{i\frac{\omega}{c} \cdot \left(1 + \frac{\chi'(\omega)}{2}\right) \cdot z} \cdot e^{-\frac{\omega}{c} \frac{\chi''(\omega)}{2} \cdot z} \quad (5.4)$$

The second term of this equation corresponds to the dispersion, the third term to the absorption of the medium. If now the exponential terms of equations 5.2 and 5.4 are compared, this (by means of equation 2.16) leads to the following final expression for the absorption cross section [25]. It is expressed as a function of the dipole response $d(\omega)$ and the electric field $E(\omega)$:

$$\sigma_a(\omega) = \frac{\omega}{c} \cdot \frac{\chi''(\omega)}{\rho_N} \quad (5.5)$$

$$= \frac{\omega}{c \cdot \varepsilon_0} \operatorname{Im} \left[\frac{d(\omega)}{E(\omega)} \right] \quad (5.6)$$

A.2 Photographs of experimental setup

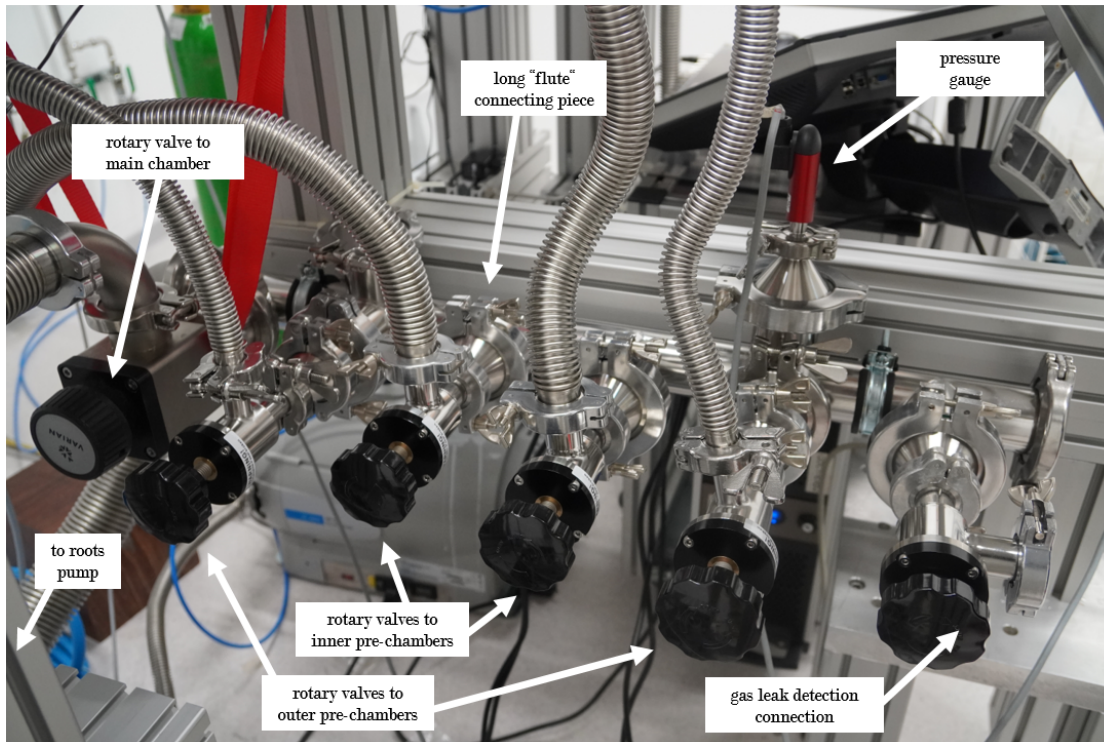


Figure 5.1: Photograph of pre-vacuum system with labelled components

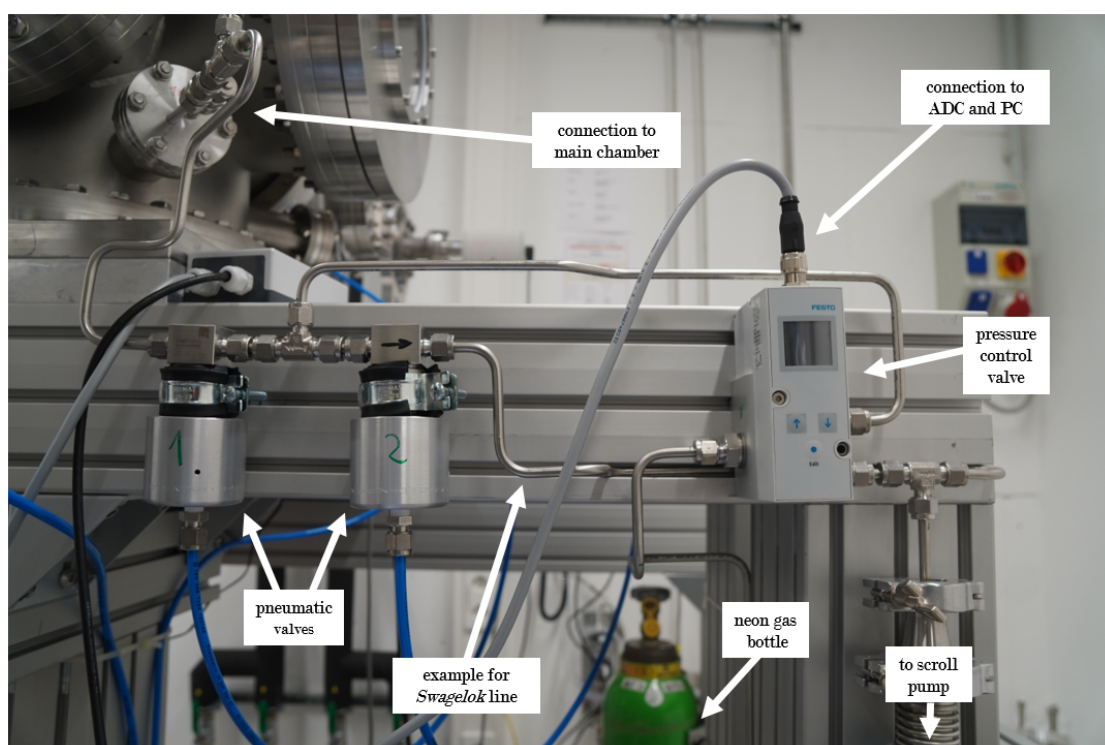


Figure 5.2: Photograph of gas supply system with labelled components

A.3 Digital measurements for hole diameters

Image	Error [px]	h_1 [px]	c_1 [px]	h_2 [px]	c_2 [px]	Ratio
1	2	36	1195	70	1190	1.953 ± 0.122
	2	35	1199	70	1211	1.980 ± 0.127
	2	34	1228	73	1324	1.991 ± 0.129
2	2	46	1310	89	1286	1.971 ± 0.097
	2	49	1393	95	1372	1.968 ± 0.090
	2	47	1359	92	1332	1.997 ± 0.096

Table 5.1: Supplement to chapter 3.5: measured pixel values for cell width c_i and hole diameter h_i , resulting ratios of hole diameter

A.4 Complete set of simulation results for chapter 4.3

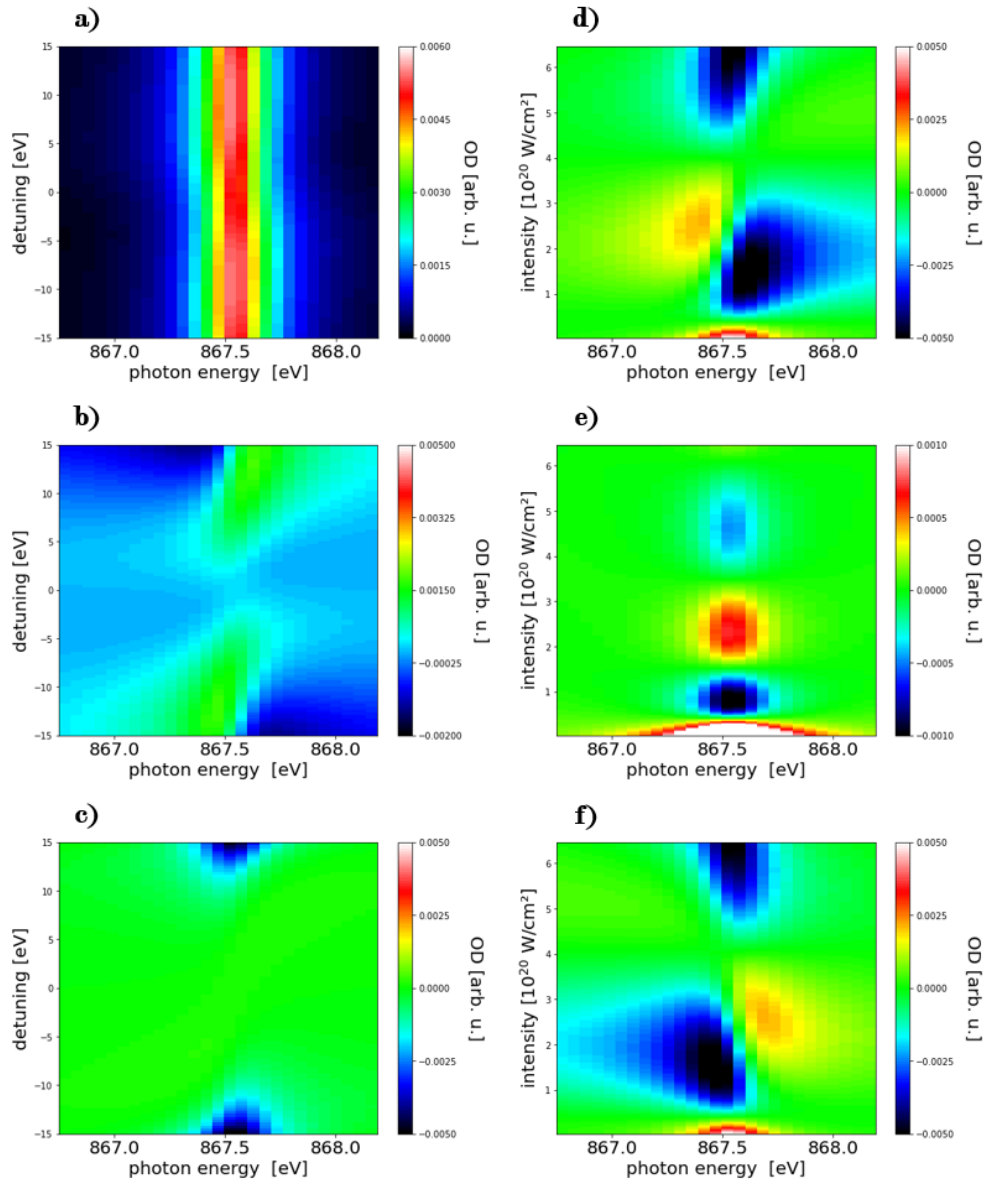


Figure 5.3: Simulation results for OD plotted against photon energy ROI and...
 ...detuning for fixed peak intensity values:
 a) $I_0 = 3.2 \cdot 10^{18}$ W/cm 2 , b) $I_0 = 3.3 \cdot 10^{20}$ W/cm 2 , c) $I_0 = 6.5 \cdot 10^{20}$ W/cm 2
 ...intensity for fixed detuning values:
 d) $\Delta = -15$ eV, e) $\Delta = 0$ eV, f) $\Delta = 15$ eV

Glossary

AS	Absorption Spectroscopy
CF	Copper Flange
<i>EuXFEL</i>	<i>European X-Ray Free-Electron Laser</i>
FWHM	Full Width Half Maximum
GF	Gas Flow
KF	Klein Flansch (Small Flange)
OD	Optical Density
QM	Quantum Mechanics
RS	Raman Scattering
SASE	Self-Amplified Spontaneous Emission
SEQ	Schrödinger Equation
SQS	Small Quantum Systems
XFEL	X-Ray Free-Electron Laser
XUV	Extreme Ultra Violet

Acknowledgment

Zu Beginn des vierten Semesters nahm mein Bachelorstudium eine abrupte Wende. Gerade noch in Mitten des Studienlebens und täglich an der Universität, katapultierte uns die Pandemie mit einem Mal in ein Fernstudium. Für mich war das, wie für viele Studierende, ein jäher und kaum willkommenener Einschnitt. Bei der Planung meines sechsten Semesters und der Suche nach einem Bacheloranden-Platz war es mir daher ein besonderes Anliegen, wieder vor Ort studieren, arbeiten und leben zu können. Vor diesem Hintergrund bin ich einigen Akteurinnen und Akteuren am *MPIK* Heidelberg zu besonderem Dank verpflichtet:

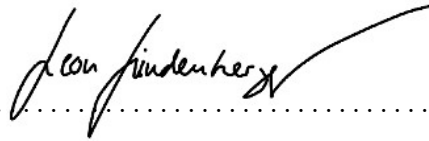
Thomas Pfeifer, für den ersten Kontakt, das passionierte Seminar, die erste Einladung und seitdem für viele ermutigende, hilfreiche und positive Gespräche. Vor allem danke ich natürlich für die offizielle Betreuung meines Projekts und die Erstkorrektur dieser Arbeit. **Christian Ott**, für die erste Laborführung, den entscheidenden Austausch im Vorfeld, viele physikalische, organisatorische und moralische Hilfestellungen, erste Korrekturen und solche bis zum Schluss sowie die Gesamtbetreuung meiner Arbeit. **Alexander Dorn**, für die spontane Übernahme der Zweitkorrektur dieser Arbeit, trotz der Abgabe im Hochsommer, und den positiven Austausch im Vorfeld. **Alexandra Heid**, für die Vorbereitung meines Projektpraktikums und den herzlichen Empfang am Institut, die ständige Unterstützung in allen organisatorischen Belangen und gute Gespräche. **Patrick Rupprecht**, **Lukas Röhrich** und **Felix Henrich**, für ausführliche Erfahrungsberichte, hilfreiche Tipps und das kollegiale Gefühl sowie anregende Gespräche im Büro und außerhalb, trotz der beschränkenden Umstände. **Alexander von der Dellen**, für viele lehrreiche, spannende und humorvolle Stunden der Arbeit und Gespräche im Labor, die konsequente Unterstützung des Projekts sowie seine offene und besonders herzliche Art.

Trotz der pandemiebedingten Umstände habe ich die Zeit am Institut als besonders sozial und inspirierend empfunden. Sicher bleiben hier viele ungenannt, die für dieses angenehme und konstruktive Arbeitsklima mitverantwortlich sind. Ihnen und Euch allen verdanke ich eine wunderbare Zeit, viele bereichernde Erkenntnisse und Lehren und die Rückkehr aus dem Fernstudium an ein Institut, das kaum einladender sein können. Zu guter Letzt und allen voran gilt mein Dank jedoch **Alexander Magunia**, der in all der Zeit und gegen Ende des Projekts noch einmal verstärkt mein zentraler Ansprechpartner war, mich in Experiment und Theorie eingeführt und bei jedem Schritt begleitet hat. Eine konstruktivere, humor- und verständnisvollere sowie freundschaftlichere Betreuung hätte ich mir nicht wünschen können. Ich hoffe und bin zuversichtlich, dass die Abgabe dieser Arbeit nicht das Ende des Austauschs mit ihm und über das Projekt bedeutet.

Erklärung

Ich versichere, dass ich diese Arbeit selbstständig verfasst habe und keine anderen als die angegebenen Quellen und Hilfsmittel benutzt habe.

Heidelberg, den 06. August 2021



.....

Leon Niklas Lindenberger